Technische Universität München
Fakultät für Elektrotechnik und Informationstechnik

Optimal Power Flow in Hybrid AC/DC Power Systems

Modeling, Methods, and Design Implications

Matthias Hotz

Vollständiger Abdruck der von der Fakultät für Elektrotechnik und Informationstechnik der Technischen Universität München zur Erlangung des akademischen Grades eines

Doktor-Ingenieurs (Dr.-Ing.)

genehmigten Dissertation.

Vorsitzender:

Prof. Dr.-Ing. Ulf Schlichtmann

Prüfende der Dissertation:

1. Prof. Dr.-Ing. Wolfgang Utschick
2. Prof. Mario Paolone, Ph.D.

Die Dissertation wurde am 01.07.2020 bei der Technischen Universität München eingereicht und durch die Fakultät für Elektrotechnik und Informationstechnik am 25.01.2021 angenommen.

to Verena and Oskar

Abstract

High-voltage direct current (HVDC) systems are increasingly incorporated into today's alternating current (AC) power grids, leading to large-scale *hybrid AC/DC power systems*. The *optimal power flow* (OPF) is the cost-optimal scheduling of the generation resources of a power system under consideration of its transmission capabilities and is of fundamental importance with a wide range of applications.

This work presents a mathematical and software framework for the study of the OPF in hybrid AC/DC power systems. A system model is introduced that enables conclusive system studies as well as substantiated mathematical explorations. Therewith, an OPF formulation is devised that features a *unified* representation of AC and DC subgrids. This simplifies the study of hybrid systems considerably and enables the direct generalization of results on AC grids to DC grids. The latter is utilized to present two *convex relaxations* that can improve the tractability of the OPF problem. Moreover, the relation of *locational marginal prices* to the OPF problem is elucidated and it is shown that the convex relaxations can also enable the efficient computation of optimal nodal prices for electricity markets. The theory is cast into an open-source software to readily enable the computational study of hybrid power systems.

The framework is then utilized to deduce *design implications* for hybrid AC/DC power systems. It is shown that the conversion of certain existing AC lines to DC operation can enable a major increase in transmission capacity and support the applicability of convex relaxations. This systematic integration of power electronics flexibilizes the power flow and induces a novel *capacity expansion strategy* that relies on *existing* transmission corridors. In several case studies, it is shown that this transition of an AC power system into a *structured* hybrid AC/DC power system can increase the transmission capacity and improve the utilization of the grid infrastructure. The results demonstrate that the strategic application of HVDC technology can induce a flexibilization on a *system level* and mitigate the impact of congestion.

Zusammenfassung

Hochspannungs-Gleichstrom-Übertragung (HGÜ) wird zunehmend in Drehstrom-Energieversorgungsnetzen integriert, wodurch großskalige *hybride Stromnetze* entstehen. Der *optimale Lastfluss* beschreibt die kostenoptimale Einsatzplanung von Energieerzeugungsanlagen unter Berücksichtigung der Energieübertragungsfähigkeiten des Netzes und ist von grundlegender Wichtigkeit mit umfassender Anwendung.

In der vorliegenden Arbeit wird ein mathematisches Rahmenwerk sowie eine Softwarelösung für die Untersuchung des optimalen Lastflusses in hybriden Stromnetzen präsentiert. Es wird ein Systemmodell vorgestellt, welches fundierte Lastflussstudien sowie rigorose mathematische Analysen ermöglicht. Darauf aufbauend wird eine Formulierung des optimalen Lastflusses eingeführt, welche Dreh- und Gleichstromnetze einheitlich abbildet. Dadurch wird die Betrachtung hybrider Stromnetze signifikant vereinfacht und die Verallgemeinerung von Ergebnissen von Dreh- zu Gleichstromnetzen ermöglicht. Anhand dessen werden zwei *konvexe Relaxationen* des optimalen Lastflusses präsentiert, welche die global-optimale Lösbarkeit verbessern können. Desweiteren werden die Grenzkosten an Netzknoten mit dem optimalen Lastfluss in Zusammenhang gebracht und gezeigt, dass die konvexen Relaxationen auch der effizienten Berechnung der *optimalen Knotenpreise* in Strommärkten dienen können. Diese Resultate sind in einem quelloffenen Softwarepaket umgesetzt, welches die simulationsbasierte Untersuchung von hybriden Stromnetzen ermöglicht.

Mittels dieses Rahmenwerks werden anschließend Implikationen für die Konzipierung von hybriden Stromnetzen abgeleitet. Insbesondere wird gezeigt, dass die Umstellung von ausgewählten Drehstrom-Übertragungsleitungen zu HGÜ-Verbindungen sowohl die Übertragungskapazität erhöhen als auch die Anwendbarkeit der konvexen Relaxationen unterstützen kann. Diese systematische Einbettung von Leistungselektronik flexibilisiert den Energiefluss und impliziert eine neuartige *Netzausbaustrategie*, welche auf *bestehenden* Stromtrassen beruht. Mehrere Fallstudien zeigen, dass ein Übergang von einem Drehstromnetz zu einem *strukturierten* hybriden Stromnetz die Gesamtübertragungskapazität erhöhen und die Nutzung der Netzinfrastruktur verbessern kann. Die strategische Einbettung von HGÜ-Technik kann folglich eine Flexibilisierung auf *Systemebene* bewirken und Netzüberlastungen verringern.

Acknowledgements

I would like to express my deepest gratitude to my doctoral adviser Prof. Wolfgang Utschick, whose continued support on all levels – professionally, personally, emotionally, and in funding – enabled this research endeavor. This thrilling ride into unknown territory with its ups and downs crafted into an absorbing arc of suspense was only possible due to you and I am forever thankful for that. I am also very grateful to Prof. Mario Paolone for examining this dissertation, to Prof. Ulf Schlichtmann for chairing the defense, and to Prof. Thomas Hamacher for serving as a mentor.

My sincere thanks go to my co-authors Dominic Hewes, Irina Boiarchuk, and Prof. Rolf Witzmann, whose expertise and sharing of data was instrumental to this work. Dominic, I'll miss our immersions in the appreciation of a delicate espresso seasoned with diverting chats about power systems, the universe, and everything. Special thanks also to Mohasha Sampath and Prof. Hoay Beng Gooi for the fruitful collaboration and for hosting me several times at the Nanyang Technological University in Singapore. These visits were an amazing experience – professionally, culinary, and beyond. I had great pleasure working with my students and I'm particularly thankful to Julia Sistermanns, Michael Mitterer, Vincent Bode, Christian Wahl, and Yangyang He for supporting my research. I would like to extend my thanks to Matthias Huber, Andrej Jokić, Maximilian Riemensberger, Lorenz Weiland, and Niklas Winter for the valuable discussions that reflect in this work. Furthermore, I'm very grateful to Niklas Vespermann, Ferdinand Flechtner, and Prof. Gunther Friedl for the opportunity to share our enthusiasm and results with an audience beyond the usual suspects. Finally, a heartfelt thanks to all the people at our chair – to Michael Newinger for being an awesome office mate, to Ulrike Heer, Michael Joham, and Ali Yilmazcan for their support, and to all my colleagues – for the conversations, extraordinary humor, and legendary tastings. It was an exceptional time with you!

I'm deeply grateful to my family, for the roots to grow and to be grounded, for the affection, faith, and interest. And, in the end, this dissertation could have never become a reality without the continuous support and love of my wife Verena and the gigawatts of power radiated by our little sunshine Oskar. There is no expression of thanking that can live up to this, so I've only left to say, I love you!

Contents

List of Figures **xv**

List of Tables **xvii**

Acronyms **xix**

Notation **xxi**

1 Introduction **1**
- 1.1 Motivation and Research Question 4
- 1.2 Scientific Contributions 5
- 1.3 Outline 8

2 Modeling of Hybrid AC/DC Grids **11**
- 2.1 Network Topology 13
- 2.2 Electrical Model 15
  - 2.2.1 Branch Model 15
  - 2.2.2 Bus Model 17
  - 2.2.3 Converter Model 18
  - 2.2.4 Generators, Prosumers, and Loads 20
  - 2.2.5 Power Balance 21
  - 2.2.6 Electrical Losses 22
- 2.3 System Constraints 23
  - 2.3.1 Voltage 23
  - 2.3.2 Ampacity 24
  - 2.3.3 Voltage Drop 24
  - 2.3.4 Angle Difference 25
- 2.4 Mathematical Structure 25
  - 2.4.1 Sparsity Pattern of the Coefficient Matrices 26

3 Optimal Power Flow **29**
3.1 Unified Optimal Power Flow Formulation for Hybrid AC/DC Grids . 30
3.2 Convex Relaxation 34
3.2.1 Semidefinite Relaxation 35
3.2.2 Second-Order Cone Relaxation 36

4 Locational Marginal Pricing **39**
4.1 Relation of the OPF Problem and Locational Marginal Prices 40
4.2 Convex Relaxation 43
4.2.1 Semidefinite Relaxation 43
4.2.2 Second-Order Cone Relaxation 46

5 The Hybrid Architecture **51**
5.1 Exactness of the Relaxations under the Hybrid Architecture 54
5.1.1 Physical Properties and Assumptions 55
5.1.2 Preliminaries 56
5.1.2.1 Cones and Half-Spaces in the Complex Plane 56
5.1.2.2 Properties of the Coefficient Matrices 57
5.1.3 A Characterization of Exactness 62
5.2 Engineering Interpretation and Design Implications 69
5.2.1 Focusing the Hybrid Architecture with Network Reduction . 71
5.2.2 Focusing the Hybrid Architecture with Measure Selection . . 73

6 The Software Framework "*hynet*" **75**
6.1 Fundamental Software Design 76
6.2 Complementary Mathematical Details 78
6.2.1 Injector Model 78
6.2.2 Converter Model 78
6.2.3 Bus Voltage Recovery 79
6.3 Additional Problem Formulations 80
6.3.1 Maximum Loadability 80

7 Case Studies on Grid Flexibilization **83**
7.1 The PJM Test System 84
7.1.1 Transition to the Hybrid Architecture 84
7.1.2 Results and Discussion 85
7.2 The Polish Transmission Grid 89
7.2.1 Capacity Expansion via Grid Flexibilization 89

7.2.1.1 The Hybrid Architecture 90
7.2.1.2 Focusing with Network Reduction 91
7.2.1.3 Focusing with Measure Selection 92
7.2.1.4 Congestion-Based Grid Flexibilization 94
7.2.2 Evaluation of the Optimal Power Flow 94
7.3 The German Transmission Grid 102
7.3.1 Topology-Preserving Capacity Expansion 103
7.3.2 Evaluation and Discussion 105

8 Conclusion **113**
8.1 Directions for Future Research 114

Bibliography **115**

List of Figures

2.1 Electrical models 14
2.2 P/Q-capability of a VSC and an inner polyhedral approximation 18
2.3 P/Q-capability of a generator and an inner polyhedral approximation 20

4.1 Relation of the OPF problem, the SDR, and their Lagrangian dual . . . 45
4.2 Relation of the OPF problem, the SOCR, and their Lagrangian duals . 48

5.1 Qualitative illustration of pathological price profiles 67
5.2 Annulment of KVL around a branch loop by the *hybrid architecture* . 70
5.3 Topology-preserving capacity expansion with the *hybrid architecture* 71
5.4 Focusing the *hybrid architecture* with network reduction 72
5.5 Focusing the *hybrid architecture* with measure selection 73

6.1 Illustration of *hynet*'s fundamental design and data flow 77

7.1 Single line diagram of the adapted PJM system 85
7.2 Single line diagram of an exemplary hybrid PJM system 86
7.3 Feature- and structure-preserving reduction of the Polish system . . . 91
7.4 Max. loadability & converter capacity w.r.t. corridor conversions . . . 93
7.5 Relative total injection cost w.r.t. the *hybrid architecture* 97
7.6 Reconstruction error of the SDR for different load levels 98
7.7 Optimality gap w.r.t. the SDR for different load levels 99
7.8 Reconstruction error of the SOCR for different load levels 100
7.9 Optimality gap w.r.t. the SOCR for different load levels 101
7.10 Injection cost & converter capacity w.r.t. corridor conversions 104
7.11 Illustration of the NEP and the hybrid grid 107
7.12 Injection cost and RES util. in the week with year's maximum load . 108
7.13 Branch util. and losses in the week with year's maximum load 109
7.14 Injection cost and RES util. in the week with year's minimum load . . 110
7.15 Branch util. and losses in the week with year's minimum load 111

List of Tables

2.1 Elements of the coefficient matrices of the constraints on branch k . . 27

7.1 Comparison of the original & hybrid PJM systems for 100% gen. cap. 87
7.2 Comparison of the original & hybrid PJM systems for 125% gen. cap. 88

Acronyms

AC	alternating current
B2B	back-to-back
BNetzA	Bundesnetzagentur
CSC	current source converter
DC	direct current
EVD	eigenvalue decomposition
HVDC	high-voltage direct current
IGBT	insulated-gate bipolar transistor
KCL	Kirchhoff's current law
KVL	Kirchhoff's voltage law
LCC	line-commutated converter
LMP	locational marginal price
MST	minimum spanning tree
MT-HVDC	multi-terminal HVDC
NEP	Netzentwicklungsplan Strom
OPF	optimal power flow

P/Q	active and reactive power
P2P-HVDC	point-to-point HVDC
psd	positive semidefinite
PV	photovoltaics
PWL	piecewise linear
QCQP	quadratically-constrained quadratic problem
RES	renewable energy sources
SDP	semidefinite program
SDR	semidefinite relaxation
SOCP	second-order cone program
SOCR	second-order cone relaxation
SQL	structured query language
TSO	transmission system operator
TUM	Technische Universität München
VSC	voltage source converter

Notation

$\mathbb{N}$	Set of natural numbers
$\mathbb{Z}$	Set of integers
$\mathbb{R}$	Set of real numbers
$\mathbb{R}_+$	Set of nonnegative real numbers
$\mathbb{R}_{++}$	Set of positive real numbers
$\mathbb{C}$	Set of complex numbers
$\mathbb{S}^N$	Set of Hermitian matrices in $\mathbb{C}^{N \times N}$
$\mathbb{S}^N_+$	Set of positive semidefinite matrices in $\mathbb{C}^{N \times N}$
$\mathbf{i}$	Imaginary unit $\mathbf{i} = \sqrt{-1}$
$\boldsymbol{e}_n$	nth standard basis vector of appropriate dimension
$\lvert\mathcal{C}\rvert$	Cardinality of the countable set $\mathcal{C}$
$\operatorname{int}(\mathcal{S})$	Interior of the set $\mathcal{S} \subseteq \mathbb{R}^N$
$\operatorname{relint}(\mathcal{S})$	Relative interior of the set $\mathcal{S} \subseteq \mathbb{R}^N$
	(Interior relative to the affine hull of the set)
$\dim(\mathcal{W})$	Dimension of the vector space $\mathcal{W}$
$\operatorname{Re}(x)$	Real part of $x \in \mathbb{C}$
$\operatorname{Im}(x)$	Imaginary part of $x \in \mathbb{C}$
$\lvert x\rvert$	Absolute value of $x \in \mathbb{C}$
$\arg(x)$	Principal value of the argument of $x \in \mathbb{C}$
x^*	Complex conjugate of $x \in \mathbb{C}$
$\boldsymbol{A}^{\mathrm{T}}$	Transpose of the matrix $\boldsymbol{A}$
$\boldsymbol{A}^{\mathrm{H}}$	Conjugate (Hermitian) transpose of the matrix $\boldsymbol{A}$
$\operatorname{tr}(\boldsymbol{A})$	Trace of the matrix $\boldsymbol{A}$
$\operatorname{rank}(\boldsymbol{A})$	Rank of the matrix $\boldsymbol{A}$

$\operatorname{range}(\boldsymbol{A})$	Range (column space) of the matrix $\boldsymbol{A}$
$\operatorname{null}(\boldsymbol{A})$	Nullspace (kernel) of the matrix $\boldsymbol{A}$
$\|\boldsymbol{A}\|_{\mathrm{F}}$	Frobenius norm of the matrix $\boldsymbol{A}$
$[\boldsymbol{A}]_{i,j}$	Element in row i and column j of the matrix $\boldsymbol{A}$
$\operatorname{Re}(\boldsymbol{A})$	Real part of the matrix $\boldsymbol{A} \in \mathbb{C}^{M \times N}$
$\operatorname{Im}(\boldsymbol{A})$	Imaginary part of the matrix $\boldsymbol{A} \in \mathbb{C}^{M \times N}$
$a \wedge b$	Logical conjunction of the logical values a and b
$a \vee b$	Logical disjunction of the logical values a and b
$\boldsymbol{a} \leq \boldsymbol{b}$	Component-wise inequality for vectors $\boldsymbol{a}, \boldsymbol{b} \in \mathbb{R}^N$
$\boldsymbol{A} \succeq \boldsymbol{B}$	Positive semidefiniteness of $\boldsymbol{A} - \boldsymbol{B}$ for $\boldsymbol{A}, \boldsymbol{B} \in \mathbb{S}^N$
$\boldsymbol{A} \succ \boldsymbol{B}$	Positive definiteness of $\boldsymbol{A} - \boldsymbol{B}$ for $\boldsymbol{A}, \boldsymbol{B} \in \mathbb{S}^N$
$\boldsymbol{A} \preceq \boldsymbol{B}$	Negative semidefiniteness of $\boldsymbol{A} - \boldsymbol{B}$ for $\boldsymbol{A}, \boldsymbol{B} \in \mathbb{S}^N$
$\boldsymbol{A} \prec \boldsymbol{B}$	Negative definiteness of $\boldsymbol{A} - \boldsymbol{B}$ for $\boldsymbol{A}, \boldsymbol{B} \in \mathbb{S}^N$
$\boldsymbol{A} \otimes \boldsymbol{B}$	Kronecker product of the matrices $\boldsymbol{A}$ and $\boldsymbol{B}$
$\mathcal{A} + \mathcal{B}$	Minkowski sum of the sets $\mathcal{A}$ and $\mathcal{B}$
$\mathcal{A} - \mathcal{B}$	Minkowski difference of the sets $\mathcal{A}$ and $\mathcal{B}$
$\partial f(\boldsymbol{x})$	Subdifferential of the convex function $f : \mathcal{S} \to \mathbb{R}$ at $\boldsymbol{x} \in \mathcal{S}$
$\partial_{\boldsymbol{x}} f(\boldsymbol{x}, \boldsymbol{y})$	Subdifferential with respect to $\boldsymbol{x}$ of the function $f : \mathcal{S} \times \mathcal{Y} \to \mathbb{R}$ at $(\boldsymbol{x}, \boldsymbol{y}) \in \mathcal{S} \times \mathcal{Y}$ with $f(\boldsymbol{x}, \boldsymbol{y})$ convex in $\boldsymbol{x}$ for a given $\boldsymbol{y} \in \mathcal{Y}$
$\nabla f(\boldsymbol{x})$	Gradient of the function $f : \mathcal{S} \to \mathbb{R}$ at $\boldsymbol{x} \in \mathcal{S}$
$\boldsymbol{x}_{\mathcal{N}}$	$\lvert\mathcal{N}\rvert$-tuple $\boldsymbol{x}_{\mathcal{N}} = (\boldsymbol{x}_n)_{n \in \mathcal{N}}$ for the set $\mathcal{N} \subset \mathbb{N}$ and the vectors or matrices $\boldsymbol{x}_n$
$\mathcal{S}_{\mathcal{N}}$	$\lvert\mathcal{N}\rvert$-fold Cartesian product $\mathcal{S}_{\mathcal{N}} = \prod_{n \in \mathcal{N}} \mathcal{S}$ or $\mathcal{S}_{\mathcal{N}} = \prod_{n \in \mathcal{N}} \mathcal{S}_n$ for the set $\mathcal{N} \subset \mathbb{N}$ and the set $\mathcal{S}$ or the sets $(\mathcal{S}_n)_{n \in \mathcal{N}}$, respectively
% BCL	Percent of the base case load

1 Introduction

In modern societies, the need for electricity is ubiquitous with applications in industry, transportation, communication, healthcare, and all the way down to our everyday life – probably including the device on which you are just reading this line. Broadly speaking, the infrastructure that enables and manages the transfer of electric power from producers to consumers is the *electric power system*. Historically, in the so-called *war of the currents* between Thomas Edison's and George Westinghouse's company at the end of the 19th century, *alternating current* (AC) power systems were victorious against *direct current* (DC) power systems, as transformers were an efficient means to change the voltage level in AC systems and, therewith, enable an efficient transmission of electric power over long distances. Originating from this root in electric lighting systems, for many years most electric power systems relied almost exclusively on AC transmission. Yet, in 1954, DC returned to the electric power systems in the form of the first commercial *high-voltage direct current* (HVDC) transmission system, then based on mercury-arc valves, due to the advantages of DC in submarine and cable transmission [10]. With the technological advances in power electronics, some years later HVDC systems using thyristor-based *line-commutated converters* (LCCs) were introduced, with further applications in long-distance transmission and the interconnection of asynchronous grids [10, 11]. Moreover, at the end of the 20th century, HVDC systems with *voltage source converters* (VSCs) were introduced, where the converters are based on *insulated-gate bipolar transistors* (IGBTs) and since then have seen a rapid development to lower the conversion losses and support higher voltage and power levels [11]. A particular advantage of VSCs is their ability to rapidly and independently control active and reactive power, which additionally enables the provision of ancillary services to the system, and their inherent suitability for *multi-terminal HVDC* (MT-HVDC) systems [12], supporting the connection of more than two nodes (buses) with a single HVDC system. Nowadays, already more than 170 *point-to-point HVDC* (P2P-HVDC) systems and several MT-HVDC systems are installed and many are planned [10, 13, 14]. This trend is destined

to continue [13, 15], leading to large-scale *hybrid AC/DC power systems*.

A fundamentally important problem in power systems, with applications ranging from operational and grid expansion planning to techno-economic studies, is the so-called *optimal power flow* (OPF) problem. The notion of an OPF problem was coined by Carpentier in 1962 [16, 17] and it has since seen an enormous amount of research leading to a myriad of different formulations and solution approaches, see e.g. [18–24] and the references therein. This vast amount of literature on OPF is explained by both its fundamental importance to power systems and the notorious difficulty of solving this NP-hard problem for large-scale systems. In its standard form, OPF denotes the optimization problem of identifying the cost-optimal allocation of generation resources and the corresponding system state to serve a given load, while satisfying all boundary conditions of the grid. Compared to the *economic dispatch* [22, 23], which is (only) a cost-optimal balancing of generation and load, the OPF problem additionally considers the impact of the transmission system by including its physics via the so-called *power flow equations* as well as essential system limits that ensure the viability of the resulting operating point. For a large-scale system, the OPF problem constitutes an optimization problem with thousands of optimization variables and constraints and, due to the power flow equations, it is inherently *nonconvex*. Furthermore, due to the typically high sensitivity of the power flow to changes in the bus voltages, the difficulties arising from the nonconvex nature are often accompanied by numerical challenges in the solution process. Besides the standard form and its variants, many important extensions of the OPF problem exist. For example, to postulated contingencies for resilience to outages, to the stochastic domain to account for the variability of energy sources like wind and photovoltaics, and to the time domain to consider ramping limits, unit commitment decisions, and energy storage and load scheduling, see e.g. [4, 25, 26] and the references therein.

By reason of the comprehensive predominance of AC power systems, the vast majority of works on OPF problems focuses on AC grids, cf. e.g. [18–24] and the references therein. While OPF formulations for hybrid AC/DC power systems date back to the 1980s [27], they received a growing interest in recent years due to the increasing incorporation of HVDC systems into AC transmission grids, with a particular consideration of VSC HVDC systems [28–36]. In the essence, these formulations extend the classical steady-state AC model with DC buses, DC lines and cables, as well as converters. Analogous to AC grids, which are modeled as impedance networks, DC point-to-point connections and grids are modeled as resistance networks, while the AC/DC conversion is modeled as a lossy transfer of active power between the AC and DC side with, in case of VSCs, the provision of reactive power on the AC

side, see e.g. [31, 37, 38]. Furthermore, the respective operating limits are considered, including an appropriate characterization of admissible operating points of the converters. As a consequence, the mathematical formulation and parameterization of the OPF problem for hybrid AC/DC power systems is considerably more intricate and extensive compared to AC systems, which renders the computation of the OPF for such systems even more challenging.

Due to the difficulties arising from the inclusion of the power flow equations, many OPF formulations and related problems (like nodal pricing [39]) resort to simplified system models, most notably the so-called "DC power flow" [22, 23, 40] for AC systems.[1] The "DC power flow" constitutes a *linearization* of the AC power flow equations that considers only active power and assumes lossless lines, a flat voltage profile (in the per-unit system), and small bus voltage angle differences [22, 23, 40]. While this offers an approximation of the active power flows based on linear equations, the extensive simplification generally induces a significant model mismatch, even if an approximation of the losses is included [41]. Recently, an alternative technique to improve the computational and mathematical tractability of the OPF problem was considered that avoids the necessity of model simplifications, namely *convex relaxation*. Instead of simplifying the system model, convex relaxation simplifies the structure of the *feasible set* by augmenting it with additional (non-physical) states to a convex set. Thus, the OPF problem is reformulated as a convex optimization problem and, therewith, gains access to the powerful theory of convex analysis as well as solution algorithms with polynomial-time convergence to a globally optimal solution [42–48]. In the context of (optimal) power flow, the first second-order cone and semidefinite relaxation is attributed to Jabr [49] and Bai *et al.* [50], respectively, and was followed by a vast number of works, see e.g. [21, 51–58] and the references therein. Again, owing to the predominance of AC power systems, the vast majority of works on convex relaxation of the OPF problem focuses on AC grids, while only some works consider hybrid AC/DC power systems [32–35, 59]. In convex relaxation, the extension of the feasible set introduces the advantages in computational and mathematical tractability, but at the same time limits its applicability: Only if the solution of the relaxed problem can be mapped to an equivalent point in the original feasible set, the relaxation can successfully provide a solution to the OPF problem. If this is indeed possible, the relaxation is called *exact*.

Mathematical analyses of various OPF formulations that aim to guarantee exactness have been presented for AC grids [51, 52, 60–64] and DC grids [61, 65, 66], while

[1] To denote the power flow equations, their solution and solution process, as well as their approximation, "power flow" and "load flow" is often used synonymously.

hybrid AC/DC grids did not receive much attention. For radial AC grids [52,60–62,64] and meshed AC grids with cycles limited to three branches [63], exactness has been proven under certain technical conditions. However, for systems that do not satisfy these preconditions, most notably (large-scale) power systems with a meshed AC transmission grid, exactness is not guaranteed.

1.1 Motivation and Research Question

In some cases, convex relaxation can shift the *optimal power flow* – this fundamentally important and generally NP-hard problem – into the *convex domain*, in which it can benefit from a powerful mathematical theory and efficient solution algorithms. However, in case of the most relevant and challenging setting for OPF problems, i.e., the typically widely meshed *transmission grid* of a power system, the successful utilization of convex relaxation is not ensured – and often not possible.

On the other hand, many transmission grids are currently facing substantial challenges that necessitate extensive reinforcement and expansion measures. Due to the climate change, many countries consider a decarbonization of the energy sector, especially via a transition of electricity generation based on fossil fuels toward *renewable energy sources* (RES) [13, 67]. This transition introduces an increasingly distributed and fluctuating energy production, which generally necessitates additional transmission capacity as well as stronger interconnections of regional and national grids to balance and smooth the variability of RES-based generation [13, 15].

Against this backdrop, we posed the following research question:

Can we identify grid upgrade measures that increase the transmission capacity and support the exactness of convex relaxations?

By such means, the demand for transmission capacity could be utilized to induce a *transition* in the system's design: The capacity expansion may additionally enable superior methods for an improved utilization of the grid infrastructure. Clearly, for reasons of resilience and reliability the network topology must remain *meshed*, which disqualifies the immediate utilization of the aforementioned results on exactness to answer this question. Furthermore, it is favorable that the grid upgrade measures can be implemented in *existing* transmission corridors, as new corridors often raise several issues. On one hand, the implementation of new corridors is often difficult and time consuming, most notably due to the obtainment of right of way [68, 69]. On the other hand, it can cause substantial public opposition, e.g., due to its impact on the landscape and the value of adjacent real estate [70, 71]. Thus, the considered

grid upgrade measures should be *topology-preserving*, i.e., they are implementable within the existing transmission corridors of the system.

In fact, this research question led us to the study of the *optimal power flow* in *hybrid AC/DC power systems*. As discussed above, this class of power systems has not yet experienced a thorough coverage in the literature. For this reason, the research conducted to answer the above question involved the coverage of several aspects of hybrid AC/DC power systems along the way, which evolved into this manuscript on the *modeling*, *methods*, and *design implications* for such systems.

1.2 Scientific Contributions

In the course of this dissertation, the following scientific contributions were made.

Modeling of Hybrid AC/DC Power Systems: This work presents a steady-state system model for the (optimal) power flow analysis of hybrid AC/DC power systems. The hybrid system may consist of an arbitrary interconnection of AC grids, P2P-HVDC links, and MT-HVDC systems. A particular feature of this model formulation is that it is highly expressive in its modeling capabilities and very accessible in its mathematical structure. As a result, it qualifies for both conclusive system studies as well as substantiated and focused mathematical explorations. The model evolved over time, where its final form as presented here was published in

> M. Hotz and W. Utschick, "*hynet*: An Optimal Power Flow Framework for Hybrid AC/DC Power Systems," *IEEE Transactions on Power Systems*, vol. 35, no. 2, pp. 1036–1047, Mar. 2020.

Unified OPF Formulation and Convex Relaxations: Based on the aforementioned system model, we present an OPF formulation for hybrid AC/DC power systems that supports cost minimization, loss minimization, and a combination of both. A particular feature of this OPF formulation is its *unified* representation of AC and DC subgrids in terms of both the *model formulation* and the *system state*. This complete analogy of AC and DC subgrids in the primal and Lagrangian dual domain of the OPF problem simplifies further efforts substantially: Both types of subgrids can be considered *jointly*, in implementations as well as mathematical studies. Moreover, it enables the *direct* generalization of results on AC grids to DC grids. This is shown for the *semidefinite* and *second-order cone relaxation*, which can be generalized directly without explic-

itly considering the hybrid nature of the system. This unified OPF formulation and convex relaxations, as also covered here, were published in

> M. Hotz and W. Utschick, "*hynet*: An Optimal Power Flow Framework for Hybrid AC/DC Power Systems," *IEEE Transactions on Power Systems*, vol. 35, no. 2, pp. 1036–1047, Mar. 2020.

Locational Marginal Prices and Convex Relaxations: The analogue to the OPF problem in electricity markets (with perfect competition) is nodal pricing with the *locational marginal prices* (LMPs). In this work, we show in what manner and under which conditions the LMPs of a hybrid AC/DC power system are related to the OPF problem and its Lagrangian dual. Furthermore, we prove that the semidefinite and, in particular, the second-order cone relaxation of the OPF problem facilitate an efficient computation of the LMPs under exactness. These results were first presented for hybrid systems with P2P-HVDC links in

> M. Hotz and W. Utschick, "The Hybrid Transmission Grid Architecture: Benefits in Nodal Pricing," *IEEE Transactions on Power Systems*, vol. 33, no. 2, pp. 1431–1442, Mar. 2018.

and are generalized here to the aforesaid system model and OPF formulation.

Software Framework for OPF Computations: To complement the theory and support the study of large-scale hybrid AC/DC power systems, we developed *hynet*, an open-source OPF framework for hybrid AC/DC grids with P2P-HVDC and radial MT-HVDC systems. In *hynet*, the mathematical foundation developed in this work is embedded in a flexible and object-oriented software design, which emphasizes ease of use and extensibility to facilitate an effortless adoption in research and education. Moreover, the framework is written in the popular high-level open-source programming language Python [72] that is freely available for all major platforms. This software framework, which is also discussed and utilized in this work, was published (scientifically) in

> M. Hotz and W. Utschick, "*hynet*: An Optimal Power Flow Framework for Hybrid AC/DC Power Systems," *IEEE Transactions on Power Systems*, vol. 35, no. 2, pp. 1036–1047, Mar. 2020.

The Hybrid Architecture: Finally, the research question posed in the previous section is addressed by the proposal of the so-called *hybrid architecture*, i.e., a novel *topology-preserving capacity expansion strategy*. In short, the *hybrid*

architecture utilizes the conversion of certain existing AC lines to DC operation, which can enable a major increase in transmission capacity, for a systematic incorporation of *power electronics* that induces a strong tendency toward exactness of the convex relaxations. This concept was originally proposed on the basis of hybrid AC/DC power systems with P2P-HVDC links in

> M. Hotz and W. Utschick, "A Hybrid Transmission Grid Architecture Enabling Efficient Optimal Power Flow," *IEEE Transactions on Power Systems*, vol. 31, no. 6, pp. 4504–4516, Nov. 2016.

and, subsequently, its mathematical exploration was continued in

> M. Hotz and W. Utschick, "The Hybrid Transmission Grid Architecture: Benefits in Nodal Pricing," *IEEE Transactions on Power Systems*, vol. 33, no. 2, pp. 1431–1442, Mar. 2018.

Here, this work is extended in several respects. Firstly, the concept and proof of the strong tendency toward exactness under the *hybrid architecture* is generalized to hybrid AC/DC grids with P2P-HVDC and radial MT-HVDC systems. Secondly, this mathematically inspired concept is complemented by an interpretation from an engineering viewpoint, which illustrates that the *design implications* of the *hybrid architecture* constitute a systematic approach to *grid flexibilization*. Thirdly, the thus implied *topology-preserving capacity expansion strategy* is investigated in several case studies, which range from an illustration of its principles in a small-scale example to the demonstration of its potential in resolving an issue that currently challenges the German transmission grid.

Concluding, the scientific publications related to this doctoral research work are listed below. As documented above, the publications [1–3] emanated from the main research work for this dissertation. The work in [5] may be regarded as an early preliminary result for the case study in Section 7.3, while [7] originated from the specific network reduction requirements in Section 5.2.1. Finally, the works [4, 6] arose from a collaboration with the Nanyang Technological University, Singapore, in which the *hybrid architecture* was studied in the context of unit commitment.

Journal Publications:

[1] **M. Hotz** and W. Utschick, "A Hybrid Transmission Grid Architecture Enabling Efficient Optimal Power Flow," *IEEE Transactions on Power Systems*, vol. 31, no. 6, pp. 4504–4516, Nov. 2016.

[2] **M. Hotz** and W. Utschick, "The Hybrid Transmission Grid Architecture: Benefits in Nodal Pricing," *IEEE Transactions on Power Systems*, vol. 33, no. 2, pp. 1431–1442, Mar. 2018.

[3] **M. Hotz** and W. Utschick, "*hynet*: An Optimal Power Flow Framework for Hybrid AC/DC Power Systems," *IEEE Transactions on Power Systems*, vol. 35, no. 2, pp. 1036–1047, Mar. 2020.

[4] L. P. M. I. Sampath, **M. Hotz**, H. B. Gooi, and W. Utschick, "Network-Constrained Thermal Unit Commitment for Hybrid AC/DC Transmission Grids under Wind Power Uncertainty," *Applied Energy*, vol. 258, Jan. 2020.

Conference Publications:

[5] **M. Hotz**, I. Boiarchuk, D. Hewes, R. Witzmann, and W. Utschick, "Reducing the Need for New Lines in Germany's Energy Transition: The Hybrid Transmission Grid Architecture," *International ETG Congress 2017*, Nov. 2017.

[6] L. P. M. I. Sampath, **M. Hotz**, H. B. Gooi, and W. Utschick, "Unit Commitment with AC Power Flow Constraints for a Hybrid Transmission Grid," *20th Power Systems Computation Conference (PSCC)*, Jun. 2018.

[7] J. Sistermanns, **M. Hotz**, W. Utschick, D. Hewes, and R. Witzmann, "Feature- and Structure-Preserving Network Reduction for Large-Scale Transmission Grids," *13th IEEE PowerTech*, Milan, Italy, Jun. 2019.

1.3 Outline

The organization of the manuscript essentially follows the synopsis of the scientific contributions in the previous section with a partitioning of the discussion of the *hybrid architecture* into a theoretical and practical part. Chapter 2 presents the *system model* for hybrid AC/DC power systems as well as a characterization of the *physical* and *operational limits*, which is then complemented by a discussion of important aspects of the *mathematical structure*. Chapter 3 discusses the *OPF problem*, for which a relaxation of the state space of DC subgrids is introduced and studied to obtain a *unified* OPF formulation. On this basis, two convex relaxations of the OPF problem are presented, i.e., a *semidefinite* and *second-order cone relaxation*. Chapter 4 turns the attention to a market context and discusses the LMPs, which are the *optimal nodal prices* under perfect competition. The relation of LMPs to the *Lagrangian dual* of the OPF problem is analyzed and the utilization of the convex relaxations for the

efficient computation of LMPs is explored. Chapter 5 motivates and introduces the *hybrid architecture*, for which the strong tendency toward exactness of the convex relaxations is shown by entangling a sufficient condition for exactness and the nature of LMPs into an interpretable *characterization of exactness*. Subsequently, this result is discussed from an engineering perspective to reveal the *design implications* of the *hybrid architecture*. Chapter 6 introduces the OPF software framework *hynet*, whose software documentation is complemented by relating the modeling and theory in this work to the software design. Furthermore, the *maximum loadability problem* is presented as an exemplary extension of this framework. Chapter 7 presents several case studies to demonstrate the implications of the *hybrid architecture* for *grid flexibilization* and *topology-preserving capacity expansion* as well as to show their efficacy for increasing the effective transmission capacity and improving the utilization of the grid infrastructure. Finally, Chapter 8 concludes this work and highlights some potential directions for future research.

2 Modeling of Hybrid AC/DC Grids

This chapter presents the model of hybrid AC/DC power systems for power flow analysis that was developed in the series of work in [1–3]. It supports the modeling of an arbitrary interconnection of AC and DC grids, where the latter may be P2P-HVDC systems or MT-HVDC systems with a radial or meshed topology. In the development of this model, particular care was taken that it is both highly expressive in its modeling capabilities and very accessible in its mathematical structure. Many works on mathematical and computational aspects of OPF problems use rather simple system models to focus the mathematical exposition (cf. e.g. [21, 52, 61, 63, 65, 66, 73, 74]), which may leave the reader questioning if or under which conditions the results generalize to practical models. On the other hand, works that focus on the expressiveness of the model can result in bulky formulae (cf. e.g. [35]), which complicates a further exposition and may obfuscate or hamper insights into the mathematical structure. The model presented in this chapter attempts to overcome this issue by carefully applying abstraction. To this end, specific aspects of the mathematical structure of the model are kept explicit, while certain details are made implicit with the appropriate definition or use of higher-level symbols or concepts. This includes, for example, the unified representation of AC and DC subgrids, the concept of injectors that unifies the representation of generators, prosumers, and loads, as well as the formulation of system constraints in a unified mathematical form. Therewith, an elaborate model with an accessible mathematical structure is obtained, which is applicable to both conclusive system studies as well as substantiated and focused mathematical explorations.

The presented model is developed for power flow analysis and considers the system in steady state. To this end, AC grids are considered as balanced three-phase systems, for which the power flow analysis can be based on a single-phase model comprising equivalent π-models with lumped parameters that is analyzed in the phasor domain [75, 76]. DC grids, as per the steady state condition, are considered as resistive networks [37, 38, 77]. The currently prevalent converter technologies are

line-commutated *current source converters* (CSCs), also known as *line-commutated converters* (LCCs), and self-commutated *voltage source converters* (VSCs) [10, 12]. A converter station comprises, besides the converters themselves, also transformers and filters as well as, in case of a VSC, a phase reactor and, in case of an LCC, a capacitor bank [10, 12]. These parts of the converter station can be considered via equivalent π-models, while the converter itself is modeled as a lossy transfer of active power between the AC and DC side of the converter with, in case of VSCs, the provision of reactive power on the AC side, see also [31, 37, 38]. For the modeling of converter losses, most recent works consider a quadratic function in the converter current [28–30, 33, 35, 37, 78], with the most advanced formulation in [31] using an individual parameterization for the rectifier and inverter mode. This loss model can be traced back to the Master's thesis [79] of Daelemans in 2008 and, notably, also its parameterization in most case studies.[2] The parameters therein are based on the Södra Länken HVDC Light® link (600 MW/$\pm$300 kV) [79, Sec. 5.3]. However, as stated in [79], the losses are specific to each HVDC application and, furthermore, the losses are steadily decreasing with the continued development of HVDC technology [11], which may invalidate the adequacy of the parameters in [79] for case studies with current converter technologies. Thus, although this converter loss model is suitable, the unavailability of proper parameters can complicate an appropriate loss modeling on this basis. For this reason, the model presented here considers a combination of mode-dependent proportional losses as well as static (no-load) losses to offer an adequate representation of converter losses based on a straightforward parameterization. In terms of operating limits, the most elaborate characterizations for VSCs include a converter current limit as well as constraints that restrict the provision of reactive power based on the coupling of the AC- and DC-side voltage, cf. [30, 31, 37]. Several works that elaborately characterize the P/Q-capability of converters, at the same time, only employ rudimentary box constraints to approximate the P/Q-capability of generators, cf. e.g. [30, 31, 33, 34]. To address this issue, the model hereafter describes the range of safe operating points with polyhedral sets, which enables a consistent and flexible characterization of P/Q-capabilities.

The presentation of the system model is divided into a description of the *network topology* and the *electrical model*. This is complemented by the formulation of physical and operational limits as *system constraints* and a concluding discussion of

[2] All documented choices of the coefficients for the converter loss model in [28–30, 33, 35, 37, 78] trace back to [79]: The work [28] refers to [80], where the latter refers to [81] that is based on [79]. In [37], the authors state that the loss data is a scaled version of [79]. The works [35, 78] refer to [81] and [31] refers to [37], which are both traced back to [79] above. The work [30] directly refers to [79]. In [29], which is also referred to by [33], the origin of the loss data is not documented.

the mathematical structure of the model. Below, AC lines, cables, transformers, and phase shifters are referred to as *AC branches*, DC lines and cables as *DC branches*, inverters, rectifiers, VSCs, and *back-to-back* (B2B) converters as *converters*, and points of interconnection, generation injection, and load connection are called *buses*.

2.1 Network Topology

The network topology of the hybrid AC/DC power system is described by the directed multigraph $\mathcal{G} = \{\mathcal{V}, \mathcal{E}, \mathcal{C}, \hat{\epsilon}, \check{\epsilon}, \hat{\gamma}, \check{\gamma}\}$, where

$$\begin{aligned}
\mathcal{V} &= \{1, \ldots, |\mathcal{V}|\} \text{ is the set of buses,} \\
\mathcal{E} &= \{1, \ldots, |\mathcal{E}|\} \text{ is the set of branches,} \\
\mathcal{C} &= \{1, \ldots, |\mathcal{C}|\} \text{ is the set of converters,}
\end{aligned}$$

and

$$\begin{aligned}
\hat{\epsilon} &: \mathcal{E} \to \mathcal{V} \text{ maps a branch to its source bus,} \\
\check{\epsilon} &: \mathcal{E} \to \mathcal{V} \text{ maps a branch to its destination bus,} \\
\hat{\gamma} &: \mathcal{C} \to \mathcal{V} \text{ maps a converter to its source bus, and} \\
\check{\gamma} &: \mathcal{C} \to \mathcal{V} \text{ maps a converter to its destination bus.}
\end{aligned}$$

Without loss of generality, the set elements are considered as consecutive numbers to facilitate the description of the electrical model in matrix notation. For the same reason, the branches are numbered instead of the commonly employed representation as unordered pairs of buses. The directionality of branches and converters is *not* related to the direction of power flow and can be chosen arbitrarily. The buses $\mathcal{V}$ are partitioned into a set $\tilde{\mathcal{V}}$ of *AC buses* and a set $\bar{\mathcal{V}}$ of *DC buses*, i.e.,

$$\mathcal{V} = \tilde{\mathcal{V}} \cup \bar{\mathcal{V}} \qquad \text{and} \qquad \tilde{\mathcal{V}} \cap \bar{\mathcal{V}} = \emptyset\,. \tag{2.1}$$

AC and DC buses must not be connected by a branch, i.e., the branches $\mathcal{E}$ are partitioned into the set $\tilde{\mathcal{E}}$ of *AC branches* and the set $\bar{\mathcal{E}}$ of *DC branches*. Specifically,

$$\mathcal{E} = \tilde{\mathcal{E}} \cup \bar{\mathcal{E}} \qquad \text{and} \qquad \tilde{\mathcal{E}} \cap \bar{\mathcal{E}} = \emptyset \tag{2.2}$$

where

$$\tilde{\mathcal{E}} = \{k \in \mathcal{E} : \hat{\epsilon}(k), \check{\epsilon}(k) \in \tilde{\mathcal{V}}\} \tag{2.3}$$

$$\bar{\mathcal{E}} = \{k \in \mathcal{E} : \hat{\epsilon}(k), \check{\epsilon}(k) \in \bar{\mathcal{V}}\}\,. \tag{2.4}$$

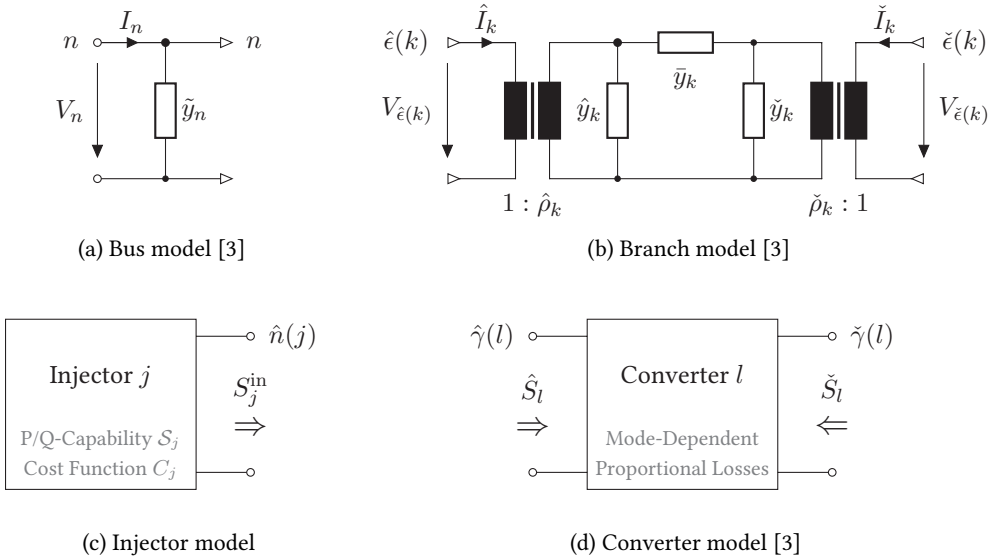

(a) Bus model [3]

(b) Branch model [3]

(c) Injector model

(d) Converter model [3]

Figure 2.1: Electrical models.

The terminal buses of converters are *not* restricted, i.e., the model supports AC/DC and DC/AC as well as AC and DC B2B converters. Concluding, to support the mathematical exposition, some terms and expressions are defined and a generally valid property of the network topology is established.

Definition 1. Consider the directed subgraph $\mathcal{G}' = \{\mathcal{V}, \mathcal{E}, \hat{\epsilon}, \check{\epsilon}\}$ with all buses and branches. A *connected component* [82] in the *underlying* [82] undirected graph of $\mathcal{G}'$ is called *subgrid*. A subgrid comprising buses in $\tilde{\mathcal{V}}$ is called *AC subgrid*. A subgrid comprising buses in $\bar{\mathcal{V}}$ is called *DC subgrid*.

Definition 2. The set $\hat{\mathcal{B}}_{\mathcal{E}}(n) \subseteq \mathcal{E}$ and $\check{\mathcal{B}}_{\mathcal{E}}(n) \subseteq \mathcal{E}$ of branches outgoing and incoming at bus $n \in \mathcal{V}$, respectively, is

$$\hat{\mathcal{B}}_{\mathcal{E}}(n) = \{k \in \mathcal{E} : \hat{\epsilon}(k) = n\} \tag{2.5}$$

$$\check{\mathcal{B}}_{\mathcal{E}}(n) = \{k \in \mathcal{E} : \check{\epsilon}(k) = n\}\,. \tag{2.6}$$

Definition 3. The set $\hat{\mathcal{B}}_{\mathcal{C}}(n) \subseteq \mathcal{C}$ and $\check{\mathcal{B}}_{\mathcal{C}}(n) \subseteq \mathcal{C}$ of converters outgoing and incoming at bus $n \in \mathcal{V}$, respectively, is

$$\hat{\mathcal{B}}_{\mathcal{C}}(n) = \{l \in \mathcal{C} : \hat{\gamma}(l) = n\} \tag{2.7}$$

$$\check{\mathcal{B}}_{\mathcal{C}}(n) = \{l \in \mathcal{C} : \check{\gamma}(l) = n\}\,. \tag{2.8}$$

Definition 4 (Self-Loop Free Network Graph)**.** The multigraph $\mathcal{G}$ does not comprise any self-loops, i.e.,

$$\nexists\, k \in \mathcal{E}: \;\; \hat{\epsilon}(k) = \check{\epsilon}(k) \quad \text{and} \quad \nexists\, l \in \mathcal{C}: \;\; \hat{\gamma}(l) = \check{\gamma}(l)\,. \tag{2.9}$$

2.2 Electrical Model

In the following, the network topology is combined with models for branches, buses, and converters as well as generators, prosumers, and loads to arrive at a mathematical description of the power flow in the hybrid AC/DC power system in terms of its state variables. Complementary, the total electrical losses are derived as a function of the state variables.

2.2.1 Branch Model

AC and DC branches are represented via the common branch model in Figure 2.1b. For branch $k \in \mathcal{E}$, which connects the source bus $\hat{\epsilon}(k)$ to the destination bus $\check{\epsilon}(k)$, it comprises two shunt admittances $\hat{y}_k, \check{y}_k \in \mathbb{C}$, a series admittance $\bar{y}_k \in \mathbb{C} \setminus \{0\}$, and two complex voltage ratios $\hat{\rho}_k, \check{\rho}_k \in \mathbb{C} \setminus \{0\}$. In the latter, $|\hat{\rho}_k|$ and $|\check{\rho}_k|$ is the tap ratio and $\arg(\hat{\rho}_k)$ and $\arg(\check{\rho}_k)$ the phase shift of the respective transformer, while

$$\rho_k = \hat{\rho}_k^* \check{\rho}_k \tag{2.10}$$

denotes the *total voltage ratio*. With the voltage relation and power conservation at the transformers, *Kirchhoff's current law* (KCL), *Kirchhoff's voltage law* (KVL), and Ohm's law, the branch currents $\hat{I}_k$ and $\check{I}_k$ can be expressed in terms of the adjacent bus voltages $V_{\hat{\epsilon}(k)}$ and $V_{\check{\epsilon}(k)}$ as

$$\hat{I}_k = \hat{\rho}_k^* \big[\bar{y}_k(\hat{\rho}_k V_{\hat{\epsilon}(k)} - \check{\rho}_k V_{\check{\epsilon}(k)}) + \hat{y}_k \hat{\rho}_k V_{\hat{\epsilon}(k)}\big] \tag{2.11a}$$

$$\check{I}_k = \check{\rho}_k^* \big[\bar{y}_k(\check{\rho}_k V_{\check{\epsilon}(k)} - \hat{\rho}_k V_{\hat{\epsilon}(k)}) + \check{y}_k \check{\rho}_k V_{\check{\epsilon}(k)}\big]\,. \tag{2.11b}$$

To describe the branch currents in matrix notation, let the *bus voltage vector* $\boldsymbol{v}$, *source current vector* $\hat{\boldsymbol{i}}$, and *destination current vector* $\check{\boldsymbol{i}}$ be defined as

$$\boldsymbol{v} = [V_1, \ldots, V_{|\mathcal{V}|}]^{\mathrm{T}} \in \mathbb{C}^{|\mathcal{V}|} \tag{2.12}$$

$$\hat{\boldsymbol{i}} = [\hat{I}_1, \ldots, \hat{I}_{|\mathcal{E}|}]^{\mathrm{T}} \in \mathbb{C}^{|\mathcal{E}|} \tag{2.13}$$

$$\check{\boldsymbol{i}} = [\check{I}_1, \ldots, \check{I}_{|\mathcal{E}|}]^{\mathrm{T}} \in \mathbb{C}^{|\mathcal{E}|}\,. \tag{2.14}$$

Furthermore, let the *source admittance matrix* $\hat{\boldsymbol{Y}} \in \mathbb{C}^{|\mathcal{E}|\times|\mathcal{V}|}$ be defined as

$$\hat{\boldsymbol{Y}} = \sum_{k\in\mathcal{E}} \boldsymbol{e}_k(\hat{\alpha}_k \boldsymbol{e}_{\hat{\epsilon}(k)}^{\mathrm{T}} + \hat{\beta}_k \boldsymbol{e}_{\check{\epsilon}(k)}^{\mathrm{T}}) \tag{2.15}$$

and the *destination admittance matrix* $\check{\boldsymbol{Y}} \in \mathbb{C}^{|\mathcal{E}|\times|\mathcal{V}|}$ be defined as

$$\check{\boldsymbol{Y}} = \sum_{k\in\mathcal{E}} \boldsymbol{e}_k(\check{\alpha}_k \boldsymbol{e}_{\check{\epsilon}(k)}^{\mathrm{T}} + \check{\beta}_k \boldsymbol{e}_{\hat{\epsilon}(k)}^{\mathrm{T}}) \tag{2.16}$$

in which

$$\hat{\alpha}_k = |\hat{\rho}_k|^2(\bar{y}_k + \hat{y}_k) \qquad \hat{\beta}_k = -\rho_k \bar{y}_k \tag{2.17a}$$

$$\check{\alpha}_k = |\check{\rho}_k|^2(\bar{y}_k + \check{y}_k) \qquad \check{\beta}_k = -\rho_k^* \bar{y}_k\,. \tag{2.17b}$$

Therewith, the source and destination branch currents in (2.11) are collectively described for all $k \in \mathcal{E}$ by

$$\hat{\boldsymbol{i}} = \hat{\boldsymbol{Y}}\boldsymbol{v} \qquad \text{and} \qquad \check{\boldsymbol{i}} = \check{\boldsymbol{Y}}\boldsymbol{v}\,. \tag{2.18}$$

In this work, the bus voltages are used as *state variables*. While AC subgrids exhibit complex-valued effective (rms) voltage phasors, DC subgrids exhibit real-valued voltages. This is considered by restricting $\boldsymbol{v}$ to $\mathcal{U}$, where

$$\mathcal{U} = \{\boldsymbol{v} \in \mathbb{C}^{|\mathcal{V}|} : V_n \in \mathbb{R}_+,\ n \in \bar{\mathcal{V}}\}\,. \tag{2.19}$$

DC lines and cables are modeled via their series resistance and assumed to be lossy. (Otherwise, their adjacent buses can be considered as an amalgamated bus.)

Definition 5. DC branches equal a series conductance, i.e.,

$$\forall k \in \bar{\mathcal{E}}: \quad \hat{\rho}_k = \check{\rho}_k = 1, \quad \hat{y}_k = \check{y}_k = 0, \quad \mathrm{Im}(\bar{y}_k) = 0\,. \tag{2.20}$$

Definition 6 (Lossy DC Branches)**.** The series conductance of all DC branches is positive, i.e.,

$$\forall k \in \bar{\mathcal{E}}: \quad \mathrm{Re}(\bar{y}_k) > 0\,. \tag{2.21}$$

In this context, it should be pointed out that HVDC systems are currently available in three different configurations, i.e., asymmetrical monopolar, symmetrical monopolar, and bipolar [10, 11, 77]. For the purpose of power flow analysis, the asymmetrical monopolar configuration may be modeled with a single DC branch, while

the symmetrical monopolar and (balanced) bipolar configuration may be modeled using two parallel DC branches (with the negative pole considered in negated form), see also [37, Sec. II-C].

2.2.2 Bus Model

Buses are modeled as depicted in Figure 2.1a. For bus $n \in \mathcal{V}$, it comprises a shunt admittance $\tilde{y}_n \in \mathbb{C}$, connections to the outgoing branches $k \in \hat{\mathcal{B}}_\mathcal{E}(n)$ as well as to the incoming branches $k \in \check{\mathcal{B}}_\mathcal{E}(n)$, and an injection port. Using KCL and Ohm's law, the injection current I_n is quantified as

$$I_n = \tilde{y}_n V_n \; + \sum_{k \in \hat{\mathcal{B}}_\mathcal{E}(n)} \hat{I}_k \; + \sum_{k \in \check{\mathcal{B}}_\mathcal{E}(n)} \check{I}_k \,. \tag{2.22}$$

With (2.11) and (2.17), I_n can be expressed in terms of bus voltages,

$$I_n = \alpha_n V_n \; + \sum_{k \in \hat{\mathcal{B}}_\mathcal{E}(n)} \hat{\beta}_k V_{\check{\epsilon}(k)} \; + \sum_{k \in \check{\mathcal{B}}_\mathcal{E}(n)} \check{\beta}_k V_{\hat{\epsilon}(k)} \tag{2.23}$$

where

$$\alpha_n = \tilde{y}_n \; + \sum_{k \in \hat{\mathcal{B}}_\mathcal{E}(n)} \hat{\alpha}_k \; + \sum_{k \in \check{\mathcal{B}}_\mathcal{E}(n)} \check{\alpha}_k \,. \tag{2.24}$$

For a description in matrix notation, let the *injection current vector* $\boldsymbol{i}$ be defined as

$$\boldsymbol{i} = [I_1, \dots, I_{|\mathcal{V}|}]^\mathrm{T} \in \mathbb{C}^{|\mathcal{V}|} \tag{2.25}$$

and the *bus admittance matrix* $\boldsymbol{Y} \in \mathbb{C}^{|\mathcal{V}| \times |\mathcal{V}|}$ be defined as

$$\boldsymbol{Y} = \sum_{n \in \mathcal{V}} \boldsymbol{e}_n \Big[\alpha_n \boldsymbol{e}_n^\mathrm{T} \; + \sum_{k \in \hat{\mathcal{B}}_\mathcal{E}(n)} \hat{\beta}_k \boldsymbol{e}_{\check{\epsilon}(k)}^\mathrm{T} \; + \sum_{k \in \check{\mathcal{B}}_\mathcal{E}(n)} \check{\beta}_k \boldsymbol{e}_{\hat{\epsilon}(k)}^\mathrm{T} \Big] \,. \tag{2.26}$$

Therewith, the injection current in (2.23) is collectively described for all $n \in \mathcal{V}$ by

$$\boldsymbol{i} = \boldsymbol{Y} \boldsymbol{v} \,. \tag{2.27}$$

Finally, note that the shunt $\tilde{y}_n$ usually models reactive power compensation and is irrelevant in DC subgrids.

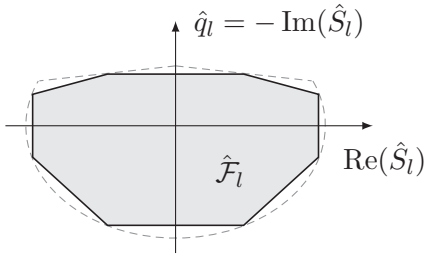

Figure 2.2: P/Q-capability of a VSC (dashed) and a polyhedral approx. (solid) [3].

Definition 7. DC buses exhibit a zero shunt admittance, i.e.,

$$\forall n \in \bar{\mathcal{V}}: \quad \tilde{y}_n = 0\,. \tag{2.28}$$

2.2.3 Converter Model

Converters are modeled as illustrated in Figure 2.1d. Other parts of a converter station besides the converter itself, like transformers and filters, can be modeled as AC branches using their equivalent π-models, see also [31, 38]. For converter $l \in \mathcal{C}$, which connects the source bus $\hat{\gamma}(l)$ to the destination bus $\check{\gamma}(l)$, the model considers the source and destination apparent power flow $\hat{S}_l, \check{S}_l \in \mathbb{C}$, respectively, where active power is converted with a forward and backward conversion loss factor $\hat{\eta}_l, \check{\eta}_l \in [0, 1)$, respectively, while reactive power may be provided. Specifically,

$$\hat{S}_l = \hat{p}_l - (1 - \check{\eta}_l)\check{p}_l - \mathbf{i}\hat{q}_l \tag{2.29a}$$
$$\check{S}_l = \check{p}_l - (1 - \hat{\eta}_l)\hat{p}_l - \mathbf{i}\check{q}_l \tag{2.29b}$$

where $\hat{p}_l \in \mathbb{R}_+$ and $\check{p}_l \in \mathbb{R}_+$ is the nonnegative active power flow from bus $\hat{\gamma}(l)$ to $\check{\gamma}(l)$ and vice versa, respectively, while $\hat{q}_l, \check{q}_l \in \mathbb{C}$ is the reactive power support and $\hat{\eta}_l, \check{\eta}_l$ enable a mode-dependent loss parameterization. Static (no-load) losses are modeled as as fixed loads, cf. Section 2.2.4. The P/Q-capability of the converter at the source and destination bus is approximated by the nonempty and bounded polyhedral set $\hat{\mathcal{F}}_l$ and $\check{\mathcal{F}}_l$, respectively. Figure 2.2 shows a qualitative example of the P/Q-capability of a typical VSC [83, Sec. 2.1], [38, Sec. 2.7.1] and an exemplary inner polyhedral approximation. This restriction to a safe operating region is captured by

$$\boldsymbol{f}_l = [\hat{p}_l, \check{p}_l, \hat{q}_l, \check{q}_l]^{\mathrm{T}} \in \mathcal{F}_l \subset \mathbb{R}_+^2 \times \mathbb{R}^2 \tag{2.30}$$

where the nonempty and bounded polyhedral set $\mathcal{F}_l$ is a reformulation of $\hat{\mathcal{F}}_l$ and $\check{\mathcal{F}}_l$ in terms of the *converter state vector* $\boldsymbol{f}_l$ using (2.29). For a description in matrix notation, the state vectors of all converters are stacked, i.e.,

$$\boldsymbol{f} = [\boldsymbol{f}_1^{\mathrm{T}}, \dots, \boldsymbol{f}_{|\mathcal{C}|}^{\mathrm{T}}]^{\mathrm{T}} \in \mathcal{F} = \prod_{l \in \mathcal{C}} \mathcal{F}_l \tag{2.31}$$

where the polyhedral set $\mathcal{F}$ is expressed as

$$\mathcal{F} = \{\boldsymbol{f} \in \mathbb{R}^{4|\mathcal{C}|} : \boldsymbol{H}\boldsymbol{f} \leq \boldsymbol{h}\}\,. \tag{2.32}$$

In the latter, $\boldsymbol{H} \in \mathbb{R}^{F \times 4|\mathcal{C}|}$ and $\boldsymbol{h} \in \mathbb{R}^F$ capture the $F \in \mathbb{N}$ inequality constraints that describe the capability regions of all converters. Finally, the absence of reactive power on the DC-side of a converter is established.

Definition 8. The DC-side of all converters exclusively injects active power, i.e.,

$$\forall l \in \bigcup_{n \in \bar{\mathcal{V}}} \hat{\mathcal{B}}_{\mathcal{C}}(n): \quad \mathcal{F}_l \subset \mathbb{R}_+^2 \times \{0\} \times \mathbb{R} \tag{2.33a}$$

$$\forall l \in \bigcup_{n \in \bar{\mathcal{V}}} \check{\mathcal{B}}_{\mathcal{C}}(n): \quad \mathcal{F}_l \subset \mathbb{R}_+^2 \times \mathbb{R} \times \{0\}\,. \tag{2.33b}$$

If the converter is lossless or if its mode is fixed, this model is linear in the converter state vector, rendering it easily tractable. Otherwise, in general the nonlinear mode complementarity constraint

$$\hat{p}_l \check{p}_l = 0 \tag{2.34}$$

is required, as a violation of mode complementarity can then induce a nonnegative and bounded loss error

$$\vartheta_l = \hat{\eta}_l\big(\hat{p}_l - [\mathrm{Re}(\hat{S}_l)]_+\big) + \check{\eta}_l\big(\check{p}_l - [\mathrm{Re}(\check{S}_l)]_+\big) \tag{2.35}$$

in converter $l \in \mathcal{C}$, where $[x]_+ = \max(x, 0)$. However, (2.34) can still be excluded in certain problem formulations. For example, OPF problems in general do not incentivize an increase of load and, as the loss error (load increase) is minimal (zero) at mode complementarity, the mode complementarity is implicitly imposed and the exclusion of (2.34) typically remains without effect.

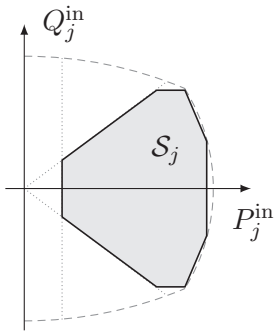

Figure 2.3: P/Q-capability of a generator (dashed) and a polyhedral approx. (solid) [3].

2.2.4 Generators, Prosumers, and Loads

For the modeling of power producers, prosumers (and flexible distribution systems), as well as flexible and fixed loads, it is observed that they are conceptually equivalent in the context of optimal power flow.[3] They comprise a set of valid operating points in the P/Q-plane and quantify their preferences via a real-valued function over the P/Q-plane. This is utilized for an abstraction of these entities to injectors. An *injector* can inject a certain amount of (positive or negative) active and reactive power, which is associated with a certain cost. The set of injectors is denoted by $\mathcal{I} = \{1, \dots, |\mathcal{I}|\}$. Injector $j \in \mathcal{I}$ injects the active power P_j^{in} and the reactive power Q_j^{in}, which are collected in the *injection vector* $\boldsymbol{s}_j = [P_j^{\mathrm{in}}, Q_j^{\mathrm{in}}]^{\mathrm{T}} \in \mathbb{R}^2$. Its valid operating points are specified by the *capability region* $\mathcal{S}_j \subset \mathbb{R}^2$, which is a nonempty and bounded polyhedral set. The Lipschitz-continuous convex *cost function* $C_j : \mathcal{S}_j \to \mathbb{R}$ specifies the cost associated with an operating point. The injector's terminal bus is specified by $\hat{n} : \mathcal{I} \to \mathcal{V}$. This is illustrated in Figure 2.1c, where injector $j \in \mathcal{I}$ is connected to the injection port of bus $\hat{n}(j)$ and injects the apparent power $S_j^{\mathrm{in}} = P_j^{\mathrm{in}} + \mathbf{i}Q_j^{\mathrm{in}}$. The model is complemented by the following definitions.

Definition 9. The set $\hat{\mathcal{B}}_{\mathcal{I}}(n) \subseteq \mathcal{I}$ of injectors connected to bus $n \in \mathcal{V}$ is

$$\hat{\mathcal{B}}_{\mathcal{I}}(n) = \{j \in \mathcal{I} : \hat{n}(j) = n\}\,. \tag{2.36}$$

Definition 10. Injectors connected to DC buses exclusively inject active power, i.e.,

$$\forall j \in \bigcup_{n \in \bar{\mathcal{V}}} \hat{\mathcal{B}}_{\mathcal{I}}(n) : \quad \mathcal{S}_j \subset \mathbb{R} \times \{0\}\,. \tag{2.37}$$

[3] In power flow studies, loads are generally considered as a constant apparent power demand [75,76]. This neglects any voltage dependency of the load, which, e.g., is approximated by the ZIP model [76].

To elucidate the concept of injectors, consider the following examples. For a generator, C_j reflects the generation cost and $\mathcal{S}_j$ is a convex approximation of its P/Q-capability. The latter is illustrated in Figure 2.3, which shows a qualitative example of the P/Q-capability of a typical generator [76, Ch. 5.4] and an exemplary inner polyhedral approximation that considers the physical limits and, additionally, a power factor and minimum output limit. For a fixed load, C_j maps to a constant value and $\mathcal{S}_j$ is singleton. For a flexible load, C_j reflects the cost for load dispatching and $\mathcal{S}_j$ characterizes the implementable load shift.

2.2.5 Power Balance

The flow conservation arising from KCL balances the nodal injections with the flow into branches and converters. At bus $n \in \mathcal{V}$, the balance of the apparent power flow is given by

$$\sum_{j \in \hat{\mathcal{B}}_{\mathcal{I}}(n)} \boldsymbol{w}^{\mathrm{T}} \boldsymbol{s}_j = I_n^* V_n + \sum_{l \in \hat{\mathcal{B}}_{\mathcal{C}}(n)} \hat{S}_l + \sum_{l \in \check{\mathcal{B}}_{\mathcal{C}}(n)} \check{S}_l \tag{2.38}$$

where $\boldsymbol{w} = [\,1,\ \mathbf{i}\,]^{\mathrm{T}} \in \mathbb{C}^2$. Therein, the left-hand side accumulates the nodal apparent power injection, while the right-hand side describes the flow of apparent power into the branches and converters. To describe (2.38) in matrix notation, it is observed that

$$I_n^* V_n = (\boldsymbol{e}_n^{\mathrm{T}} \boldsymbol{i})^{\mathrm{H}} (\boldsymbol{e}_n^{\mathrm{T}} \boldsymbol{v}) = (\boldsymbol{e}_n^{\mathrm{T}} \boldsymbol{Y} \boldsymbol{v})^{\mathrm{H}} (\boldsymbol{e}_n^{\mathrm{T}} \boldsymbol{v}) = \boldsymbol{v}^{\mathrm{H}} \left[\boldsymbol{Y}^{\mathrm{H}} \boldsymbol{e}_n \boldsymbol{e}_n^{\mathrm{T}} \right] \boldsymbol{v} \tag{2.39}$$

and, for some matrix $\boldsymbol{A} \in \mathbb{C}^{|\mathcal{V}| \times |\mathcal{V}|}$, that

$$\mathrm{Re}(\boldsymbol{v}^{\mathrm{H}} \boldsymbol{A} \boldsymbol{v}) = \frac{1}{2} \left[\boldsymbol{v}^{\mathrm{H}} \boldsymbol{A} \boldsymbol{v} + (\boldsymbol{v}^{\mathrm{H}} \boldsymbol{A} \boldsymbol{v})^* \right] = \boldsymbol{v}^{\mathrm{H}} \left[(\boldsymbol{A} + \boldsymbol{A}^{\mathrm{H}})/2 \right] \boldsymbol{v} \tag{2.40}$$

$$\mathrm{Im}(\boldsymbol{v}^{\mathrm{H}} \boldsymbol{A} \boldsymbol{v}) = \frac{1}{2\mathbf{i}} \left[\boldsymbol{v}^{\mathrm{H}} \boldsymbol{A} \boldsymbol{v} - (\boldsymbol{v}^{\mathrm{H}} \boldsymbol{A} \boldsymbol{v})^* \right] = \boldsymbol{v}^{\mathrm{H}} \left[(\boldsymbol{A} - \boldsymbol{A}^{\mathrm{H}})/(2\mathbf{i}) \right] \boldsymbol{v}\,. \tag{2.41}$$

Jointly with (2.29), (2.30), and (2.31), the nodal apparent power balance (2.38) can then be stated for all $n \in \mathcal{V}$ in terms of its real and imaginary part as

$$\boldsymbol{v}^{\mathrm{H}} \boldsymbol{P}_n \boldsymbol{v} + \boldsymbol{p}_n^{\mathrm{T}} \boldsymbol{f} = \boldsymbol{e}_1^{\mathrm{T}} \sum_{j \in \hat{\mathcal{B}}_{\mathcal{I}}(n)} \boldsymbol{s}_j\,, \qquad \forall n \in \mathcal{V} \tag{2.42a}$$

$$\boldsymbol{v}^{\mathrm{H}} \boldsymbol{Q}_n \boldsymbol{v} + \boldsymbol{q}_n^{\mathrm{T}} \boldsymbol{f} = \boldsymbol{e}_2^{\mathrm{T}} \sum_{j \in \hat{\mathcal{B}}_{\mathcal{I}}(n)} \boldsymbol{s}_j\,, \qquad \forall n \in \mathcal{V} \tag{2.42b}$$

which are called the *power balance* equations. Therein, (2.42a) describes the active power balance and (2.42b) the reactive power balance. The matrices $\boldsymbol{P}_n, \boldsymbol{Q}_n \in \mathbb{S}^{|\mathcal{V}|}$ are given by

$$\boldsymbol{P}_n = [\boldsymbol{Y}^{\mathrm{H}} \boldsymbol{e}_n \boldsymbol{e}_n^{\mathrm{T}} + \boldsymbol{e}_n \boldsymbol{e}_n^{\mathrm{T}} \boldsymbol{Y}]/2 \tag{2.43a}$$

$$\boldsymbol{Q}_n = [\boldsymbol{Y}^{\mathrm{H}} \boldsymbol{e}_n \boldsymbol{e}_n^{\mathrm{T}} - \boldsymbol{e}_n \boldsymbol{e}_n^{\mathrm{T}} \boldsymbol{Y}]/(2\mathbf{i}) \tag{2.43b}$$

and the vectors $\boldsymbol{p}_n, \boldsymbol{q}_n \in \mathbb{R}^{4|\mathcal{C}|}$ read

$$\boldsymbol{p}_n = \sum_{l \in \hat{\mathcal{B}}_{\mathcal{C}}(n)} (\boldsymbol{e}_{4l-3} - (1-\check{\eta}_l)\boldsymbol{e}_{4l-2}) \; + \sum_{l \in \check{\mathcal{B}}_{\mathcal{C}}(n)} (\boldsymbol{e}_{4l-2} - (1-\hat{\eta}_l)\boldsymbol{e}_{4l-3}) \tag{2.44a}$$

$$\boldsymbol{q}_n = -\sum_{l \in \hat{\mathcal{B}}_{\mathcal{C}}(n)} \boldsymbol{e}_{4l-1} \; - \sum_{l \in \check{\mathcal{B}}_{\mathcal{C}}(n)} \boldsymbol{e}_{4l} \, . \tag{2.44b}$$

2.2.6 Electrical Losses

In some cases, like the OPF formulation in Chapter 3, a description of the electrical losses as a function of the state variables is desired. The total electrical losses amount to the difference of total active power generation and load or, in terms of this model, the sum of the active power injections into the grid. Using the active power balance in (2.42a), this can be expressed as

$$\sum_{j \in \mathcal{I}} \boldsymbol{e}_1^{\mathrm{T}} \boldsymbol{s}_j = \sum_{n \in \mathcal{V}} \boldsymbol{e}_1^{\mathrm{T}} \sum_{j \in \hat{\mathcal{B}}_{\mathcal{I}}(n)} \boldsymbol{s}_j = \sum_{n \in \mathcal{V}} (\boldsymbol{v}^{\mathrm{H}} \boldsymbol{P}_n \boldsymbol{v} + \boldsymbol{p}_n^{\mathrm{T}} \boldsymbol{f}) = \boldsymbol{v}^{\mathrm{H}} \left[\sum_{n \in \mathcal{V}} \boldsymbol{P}_n \right] \boldsymbol{v} + \sum_{n \in \mathcal{V}} \boldsymbol{p}_n^{\mathrm{T}} \boldsymbol{f} \, . \tag{2.45}$$

Let $\boldsymbol{L} \in \mathbb{S}^{|\mathcal{V}|}$ and $\boldsymbol{l} \in \mathbb{R}^{4|\mathcal{C}|}$ be defined as

$$\boldsymbol{L} = \sum_{n \in \mathcal{V}} \boldsymbol{P}_n = \sum_{n \in \mathcal{V}} \frac{1}{2} (\boldsymbol{Y}^{\mathrm{H}} \boldsymbol{e}_n \boldsymbol{e}_n^{\mathrm{T}} + \boldsymbol{e}_n \boldsymbol{e}_n^{\mathrm{T}} \boldsymbol{Y}) = \frac{1}{2} (\boldsymbol{Y} + \boldsymbol{Y}^{\mathrm{H}}) \tag{2.46}$$

and

$$\boldsymbol{l} = \sum_{n \in \mathcal{V}} \boldsymbol{p}_n = \sum_{l \in \mathcal{C}} [\hat{\eta}_l \boldsymbol{e}_{4l-3} + \check{\eta}_l \boldsymbol{e}_{4l-2}] \tag{2.47}$$

where the reformulation utilizes (2.43a) and (2.44a). Furthermore, note that for some matrix $\boldsymbol{A} \in \mathbb{C}^{|\mathcal{V}| \times |\mathcal{V}|}$, the quadratic form can be put as

$$\boldsymbol{v}^{\mathrm{H}} \boldsymbol{A} \boldsymbol{v} = \mathrm{tr}(\boldsymbol{v}^{\mathrm{H}} \boldsymbol{A} \boldsymbol{v}) = \mathrm{tr}(\boldsymbol{A} \boldsymbol{v} \boldsymbol{v}^{\mathrm{H}}) \tag{2.48}$$

by using the cyclic property of the trace. Therewith, the *total electrical losses* can be quantified as $L(\boldsymbol{v}\boldsymbol{v}^{\mathrm{H}}, \boldsymbol{f})$, where $L : \mathbb{S}^{|\mathcal{V}|} \times \mathbb{R}^{4|\mathcal{C}|} \to \mathbb{R}$ is

$$L(\boldsymbol{V}, \boldsymbol{f}) = \operatorname{tr}(\boldsymbol{L}\boldsymbol{V}) + \boldsymbol{l}^{\mathrm{T}}\boldsymbol{f}\,. \tag{2.49}$$

At this point, the definition of L in terms of the outer product of the bus voltage vector may appear needlessly complicated, but it will turn out to be beneficial for the exposition in Chapter 3 later on.

2.3 System Constraints

In the context of (optimal) power flow, the grid's typically considered physical and operational limits concern the bus voltage and the branch flow, cf. e.g. [22, 84]. Due to the physical relation between voltage, current, and power, these system constraints can be expressed in various ways. In the following formulation, the constraints are implemented in a quadratic form in the bus voltages to unify their mathematical representation. A particular aspect therein is the departure from the constraint on the apparent power flow, which is common to describe the capacity of AC transmission lines. The limit on the apparent power flow is actually threefold. For short transmission lines it represents a physical constraint of thermal nature that is proportional to the current, for medium-length transmission lines it casts a stability constraint related to the voltage drop along the line, and for long transmission lines it represents a stability constraint related to the voltage angle difference of the adjacent buses [76, Ch. 6.1.12], [75, Ch. 4.9]. Here, these three constraints are implemented directly, which does not only increase the expressiveness and accuracy of the constraint [68] but also enables their formulation in a unified mathematical form.

2.3.1 Voltage

Due to physical and operational requirements, the voltage at bus $n \in \mathcal{V}$ must satisfy $|V_n| \in [\underline{V}_n, \bar{V}_n] \subset \mathbb{R}_+$, where $\bar{V}_n > \underline{V}_n > 0$. Considering that

$$|V_n|^2 = V_n^* V_n = (\boldsymbol{e}_n^{\mathrm{T}}\boldsymbol{v})^{\mathrm{H}}(\boldsymbol{e}_n^{\mathrm{T}}\boldsymbol{v}) = \boldsymbol{v}^{\mathrm{H}}\boldsymbol{M}_n\boldsymbol{v} \tag{2.50}$$

where $\boldsymbol{M}_n \in \mathbb{S}^{|\mathcal{V}|}$ is

$$\boldsymbol{M}_n = \boldsymbol{e}_n\boldsymbol{e}_n^{\mathrm{T}} \tag{2.51}$$

it follows that this constraint can be cast as

$$\underline{V}_n^2 \leq \boldsymbol{v}^{\mathrm{H}} \boldsymbol{M}_n \boldsymbol{v} \leq \bar{V}_n^2 \,, \qquad \forall n \in \mathcal{V} \,. \tag{2.52}$$

2.3.2 Ampacity

The thermal flow limit on branch $k \in \mathcal{E}$ can be expressed as ampacity constraints, i.e., $|\hat{I}_k| \leq \bar{\hat{I}}_k$ and $|\check{I}_k| \leq \bar{\check{I}}_k$ with $\bar{\hat{I}}_k, \bar{\check{I}}_k \in \mathbb{R}_{++}$. Considering that

$$|\hat{I}_k|^2 = \hat{I}_k^* \hat{I}_k = (\boldsymbol{e}_k^{\mathrm{T}} \hat{\boldsymbol{i}})^{\mathrm{H}} (\boldsymbol{e}_k^{\mathrm{T}} \hat{\boldsymbol{i}}) = \boldsymbol{v}^{\mathrm{H}} \hat{\boldsymbol{I}}_k \boldsymbol{v} \tag{2.53a}$$

$$|\check{I}_k|^2 = \check{I}_k^* \check{I}_k = (\boldsymbol{e}_k^{\mathrm{T}} \check{\boldsymbol{i}})^{\mathrm{H}} (\boldsymbol{e}_k^{\mathrm{T}} \check{\boldsymbol{i}}) = \boldsymbol{v}^{\mathrm{H}} \check{\boldsymbol{I}}_k \boldsymbol{v} \tag{2.53b}$$

in which $\hat{\boldsymbol{I}}_k, \check{\boldsymbol{I}}_k \in \mathbb{S}^{|\mathcal{V}|}$ are given by

$$\hat{\boldsymbol{I}}_k = \hat{\boldsymbol{Y}}^{\mathrm{H}} \boldsymbol{e}_k \boldsymbol{e}_k^{\mathrm{T}} \hat{\boldsymbol{Y}} \qquad \text{and} \qquad \check{\boldsymbol{I}}_k = \check{\boldsymbol{Y}}^{\mathrm{H}} \boldsymbol{e}_k \boldsymbol{e}_k^{\mathrm{T}} \check{\boldsymbol{Y}} \tag{2.54}$$

these ampacity constraints can be implemented as

$$\boldsymbol{v}^{\mathrm{H}} \hat{\boldsymbol{I}}_k \boldsymbol{v} \leq \bar{\hat{I}}_k^2 \,, \qquad \boldsymbol{v}^{\mathrm{H}} \check{\boldsymbol{I}}_k \boldsymbol{v} \leq \bar{\check{I}}_k^2 \,, \qquad \forall k \in \mathcal{E} \,. \tag{2.55}$$

2.3.3 Voltage Drop

The stability-related limit on the voltage drop $\nu_k \in \mathbb{R}$ along AC branch $k \in \tilde{\mathcal{E}}$, i.e.,

$$\nu_k = \frac{|V_{\check{\epsilon}(k)}|}{|V_{\hat{\epsilon}(k)}|} - 1 \tag{2.56}$$

reads $\nu_k \in [\underline{\nu}_k, \bar{\nu}_k] \subset [-1, \infty)$, with $\underline{\nu}_k < \bar{\nu}_k$. Considering that, with (2.50),

$$\nu_k \geq \underline{\nu}_k \quad \Longleftrightarrow \quad (1 + \underline{\nu}_k)^2 |V_{\hat{\epsilon}(k)}|^2 - |V_{\check{\epsilon}(k)}|^2 = \boldsymbol{v}^{\mathrm{H}} \underline{\boldsymbol{M}}_k \boldsymbol{v} \leq 0 \tag{2.57}$$

$$\nu_k \leq \bar{\nu}_k \quad \Longleftrightarrow \quad |V_{\check{\epsilon}(k)}|^2 - (1 + \bar{\nu}_k)^2 |V_{\hat{\epsilon}(k)}|^2 = \boldsymbol{v}^{\mathrm{H}} \bar{\boldsymbol{M}}_k \boldsymbol{v} \leq 0 \tag{2.58}$$

where $\underline{\boldsymbol{M}}_k, \bar{\boldsymbol{M}}_k \in \mathbb{S}^{|\mathcal{V}|}$ are

$$\underline{\boldsymbol{M}}_k = (1 + \underline{\nu}_k)^2 \boldsymbol{M}_{\hat{\epsilon}(k)} - \boldsymbol{M}_{\check{\epsilon}(k)} \tag{2.59a}$$

$$\bar{\boldsymbol{M}}_k = \boldsymbol{M}_{\check{\epsilon}(k)} - (1 + \bar{\nu}_k)^2 \boldsymbol{M}_{\hat{\epsilon}(k)} \tag{2.59b}$$

it follows that this constraint can be written as

$$\boldsymbol{v}^{\mathrm{H}} \underline{\boldsymbol{M}}_k \boldsymbol{v} \leq 0 \,, \qquad \boldsymbol{v}^{\mathrm{H}} \bar{\boldsymbol{M}}_k \boldsymbol{v} \leq 0 \,, \qquad \forall k \in \tilde{\mathcal{E}} \,. \tag{2.60}$$

2.3.4 Angle Difference

The stability-related limit on the voltage angle difference $\delta_k \in \mathbb{R}$ along AC branch $k \in \tilde{\mathcal{E}}$, i.e.,

$$\delta_k = \arg(V^*_{\hat{\epsilon}(k)} V_{\check{\epsilon}(k)}) \tag{2.61}$$

reads $\delta_k \in [\underline{\delta}_k, \bar{\delta}_k] \subset (-\pi/2, \pi/2)$, with $\underline{\delta}_k < \bar{\delta}_k$. Equivalently, it can be expressed as

$$\mathrm{Re}(V^*_{\hat{\epsilon}(k)} V_{\check{\epsilon}(k)}) \geq 0 \tag{2.62}$$

$$\tan(\underline{\delta}_k) \leq \mathrm{Im}(V^*_{\hat{\epsilon}(k)} V_{\check{\epsilon}(k)}) \,/\, \mathrm{Re}(V^*_{\hat{\epsilon}(k)} V_{\check{\epsilon}(k)}) \leq \tan(\bar{\delta}_k)\,. \tag{2.63}$$

Considering that

$$\mathrm{Re}(V^*_{\hat{\epsilon}(k)} V_{\check{\epsilon}(k)}) = \frac{1}{2}\left[V^*_{\hat{\epsilon}(k)} V_{\check{\epsilon}(k)} + V_{\hat{\epsilon}(k)} V^*_{\check{\epsilon}(k)}\right] = \frac{1}{2}\,\boldsymbol{v}^{\mathrm{H}}\left[\hat{\boldsymbol{M}}_k + \hat{\boldsymbol{M}}_k^{\mathrm{H}}\right]\boldsymbol{v} \tag{2.64}$$

$$\mathrm{Im}(V^*_{\hat{\epsilon}(k)} V_{\check{\epsilon}(k)}) = \frac{1}{2\mathbf{i}}\left[V^*_{\hat{\epsilon}(k)} V_{\check{\epsilon}(k)} - V_{\hat{\epsilon}(k)} V^*_{\check{\epsilon}(k)}\right] = -\frac{\mathbf{i}}{2}\,\boldsymbol{v}^{\mathrm{H}}\left[\hat{\boldsymbol{M}}_k - \hat{\boldsymbol{M}}_k^{\mathrm{H}}\right]\boldsymbol{v} \tag{2.65}$$

where $\hat{\boldsymbol{M}}_k \in \mathbb{R}^{|\mathcal{V}|\times|\mathcal{V}|}$ is

$$\hat{\boldsymbol{M}}_k = \boldsymbol{e}_{\hat{\epsilon}(k)} \boldsymbol{e}^{\mathrm{T}}_{\check{\epsilon}(k)} \tag{2.66}$$

it follows that (2.62) and (2.63) and, thus, the voltage angle difference constraint can be implemented as

$$\boldsymbol{v}^{\mathrm{H}} \boldsymbol{A}_k \boldsymbol{v} \leq 0\,, \quad \boldsymbol{v}^{\mathrm{H}} \underline{\boldsymbol{A}}_k \boldsymbol{v} \leq 0\,, \quad \boldsymbol{v}^{\mathrm{H}} \bar{\boldsymbol{A}}_k \boldsymbol{v} \leq 0\,, \quad \forall k \in \tilde{\mathcal{E}} \tag{2.67}$$

with $\boldsymbol{A}_k, \underline{\boldsymbol{A}}_k, \bar{\boldsymbol{A}}_k \in \mathbb{S}^{|\mathcal{V}|}$ given by

$$\boldsymbol{A}_k = -\hat{\boldsymbol{M}}_k - \hat{\boldsymbol{M}}_k^{\mathrm{H}} \tag{2.68a}$$

$$\underline{\boldsymbol{A}}_k = (\tan(\underline{\delta}_k) + \mathbf{i})\hat{\boldsymbol{M}}_k + (\tan(\underline{\delta}_k) - \mathbf{i})\hat{\boldsymbol{M}}_k^{\mathrm{H}} \tag{2.68b}$$

$$\bar{\boldsymbol{A}}_k = -(\tan(\bar{\delta}_k) + \mathbf{i})\hat{\boldsymbol{M}}_k - (\tan(\bar{\delta}_k) - \mathbf{i})\hat{\boldsymbol{M}}_k^{\mathrm{H}}\,. \tag{2.68c}$$

2.4 Mathematical Structure

In the presented model, it can be observed that the bus voltages, which are used as state variables for subgrids, appear exclusively in *quadratic form* in the power balance equations (2.42), the total electrical loss function (2.49), as well as the system constraints (2.52), (2.55), (2.60) and (2.67). In addition to this unified mathematical

form, the following exposition further shows that the coefficient matrices in these quadratic forms exhibit a rich structure. Particularly, they feature a *sparsity pattern* that is related to the network topology and their *off-diagonal elements* share an interesting relation. While the relation of the off-diagonal elements will be uncovered in Chapter 5, this section analyzes the sparsity pattern of the coefficient matrices.

2.4.1 Sparsity Pattern of the Coefficient Matrices

By the construction of the bus admittance matrix $\boldsymbol{Y}$ in (2.26), it follows that it may only contain a nonzero off-diagonal element in row i and column $j \neq i$ if and only if there exists a branch between bus i and bus j. Clearly, this transfers to the coefficient matrix $\boldsymbol{L}$ in (2.46) of the total electrical loss function, as it constitutes a weighted sum of $\boldsymbol{Y}$ and its Hermitian transpose. The coefficient matrices $\boldsymbol{P}_n$ and $\boldsymbol{Q}_n$ in (2.43) of the power balance equations may only be nonzero in the nth row and nth column, where they inherit the sparsity pattern of the nth row of the bus admittance matrix $\boldsymbol{Y}$:

$$[\boldsymbol{P}_n]_{i,j} = \boldsymbol{e}_i^{\mathrm{T}} \boldsymbol{P}_n \boldsymbol{e}_j = \frac{1}{2} \boldsymbol{e}_i^{\mathrm{T}} (\boldsymbol{Y}^{\mathrm{H}} \boldsymbol{e}_n \boldsymbol{e}_n^{\mathrm{T}} + \boldsymbol{e}_n \boldsymbol{e}_n^{\mathrm{T}} \boldsymbol{Y}) \boldsymbol{e}_j = \begin{cases} \mathrm{Re}([\boldsymbol{Y}]_{i,j}) & \text{if } i = j = n \\ [\boldsymbol{Y}]_{i,j}/2 & \text{if } i = n \neq j \\ [\boldsymbol{Y}]_{j,i}^*/2 & \text{if } j = n \neq i \\ 0 & \text{otherwise} \end{cases} \tag{2.69}$$

$$[\boldsymbol{Q}_n]_{i,j} = \boldsymbol{e}_i^{\mathrm{T}} \boldsymbol{Q}_n \boldsymbol{e}_j = \frac{1}{2\mathbf{i}} \boldsymbol{e}_i^{\mathrm{T}} (\boldsymbol{Y}^{\mathrm{H}} \boldsymbol{e}_n \boldsymbol{e}_n^{\mathrm{T}} - \boldsymbol{e}_n \boldsymbol{e}_n^{\mathrm{T}} \boldsymbol{Y}) \boldsymbol{e}_j = \begin{cases} \mathrm{Im}([\boldsymbol{Y}]_{i,j}) & \text{if } i = j = n \\ -[\boldsymbol{Y}]_{i,j}/(2\mathbf{i}) & \text{if } i = n \neq j \\ [\boldsymbol{Y}]_{j,i}^*/(2\mathbf{i}) & \text{if } j = n \neq i \\ 0 & \text{otherwise} \end{cases} \tag{2.70}$$

With the source and destination admittance matrix in (2.15) and (2.16), the elements of the coefficient matrices $\hat{\boldsymbol{I}}_k$ and $\check{\boldsymbol{I}}_k$ in (2.54) of the ampacity constraint can be put as

$$[\hat{\boldsymbol{I}}_k]_{i,j} = \boldsymbol{e}_i^{\mathrm{T}} \hat{\boldsymbol{Y}}^{\mathrm{H}} \boldsymbol{e}_k \boldsymbol{e}_k^{\mathrm{T}} \hat{\boldsymbol{Y}} \boldsymbol{e}_j = \boldsymbol{e}_i^{\mathrm{T}} (\hat{\alpha}_k^* \boldsymbol{e}_{\hat{\varepsilon}(k)} + \hat{\beta}_k^* \boldsymbol{e}_{\check{\varepsilon}(k)}) (\hat{\alpha}_k \boldsymbol{e}_{\hat{\varepsilon}(k)}^{\mathrm{T}} + \hat{\beta}_k \boldsymbol{e}_{\check{\varepsilon}(k)}^{\mathrm{T}}) \boldsymbol{e}_j \tag{2.71}$$

$$[\check{\boldsymbol{I}}_k]_{i,j} = \boldsymbol{e}_i^{\mathrm{T}} \check{\boldsymbol{Y}}^{\mathrm{H}} \boldsymbol{e}_k \boldsymbol{e}_k^{\mathrm{T}} \check{\boldsymbol{Y}} \boldsymbol{e}_j = \boldsymbol{e}_i^{\mathrm{T}} (\check{\alpha}_k^* \boldsymbol{e}_{\check{\varepsilon}(k)} + \check{\beta}_k^* \boldsymbol{e}_{\hat{\varepsilon}(k)}) (\check{\alpha}_k \boldsymbol{e}_{\check{\varepsilon}(k)}^{\mathrm{T}} + \check{\beta}_k \boldsymbol{e}_{\hat{\varepsilon}(k)}^{\mathrm{T}}) \boldsymbol{e}_j \,. \tag{2.72}$$

Therewith, as well as (2.59) and (2.68), the elements of the coefficient matrices of the constraints on branch $k \in \mathcal{E}$, i.e., the ampacity, voltage drop, and angle difference

i	j	$[\hat{\boldsymbol{I}}_k]_{i,j}$	$[\check{\boldsymbol{I}}_k]_{i,j}$	$[\underline{\boldsymbol{M}}_k]_{i,j}$	$[\bar{\boldsymbol{M}}_k]_{i,j}$	$[\boldsymbol{A}_k]_{i,j}$	$[\underline{\boldsymbol{A}}_k]_{i,j}$	$[\bar{\boldsymbol{A}}_k]_{i,j}$
$\hat{\epsilon}(k)$	$\hat{\epsilon}(k)$	$\lvert\hat{\alpha}_k\rvert^2$	$\lvert\check{\beta}_k\rvert^2$	$(1+\underline{\nu}_k)^2$	$-(1+\bar{\nu}_k)^2$	0	0	0
$\hat{\epsilon}(k)$	$\check{\epsilon}(k)$	$\hat{\alpha}_k^*\hat{\beta}_k$	$\check{\alpha}_k\check{\beta}_k^*$	0	0	-1	$\tan(\underline{\delta}_k)+\mathbf{i}$	$-\tan(\bar{\delta}_k)-\mathbf{i}$
$\check{\epsilon}(k)$	$\hat{\epsilon}(k)$	$\hat{\alpha}_k\hat{\beta}_k^*$	$\check{\alpha}_k^*\check{\beta}_k$	0	0	-1	$\tan(\underline{\delta}_k)-\mathbf{i}$	$-\tan(\bar{\delta}_k)+\mathbf{i}$
$\check{\epsilon}(k)$	$\check{\epsilon}(k)$	$\lvert\hat{\beta}_k\rvert^2$	$\lvert\check{\alpha}_k\rvert^2$	-1	1	0	0	0
otherwise		0	0	0	0	0	0	0

Table 2.1: Elements of the coefficient matrices of the constraints on branch $k \in \mathcal{E}$.

constraint, can be identified by inspection as documented in Table 2.1. Considering further that the coefficient matrix $\boldsymbol{M}_n$ in (2.51) of the voltage constraint is diagonal, the sparsity pattern of these matrices can be summarized as in Corollary 1 below. In words, it states that all these coefficient matrices adhere to a sparsity pattern that is induced by the network topology of the system's subgrids.

Definition 11. The set $\mathcal{K} \subset \mathbb{S}^{|\mathcal{V}|}$ of coefficient matrices is

$$\mathcal{K} = \left\{ \boldsymbol{P}_n, \boldsymbol{Q}_n, \boldsymbol{M}_n, -\boldsymbol{M}_n, \hat{\boldsymbol{I}}_k, \check{\boldsymbol{I}}_k, \underline{\boldsymbol{M}}_k, \bar{\boldsymbol{M}}_k, \boldsymbol{A}_k, \underline{\boldsymbol{A}}_k, \bar{\boldsymbol{A}}_k \right\}_{n\in\mathcal{V},\, k\in\mathcal{E}} . \tag{2.73}$$

Corollary 1. *Let the projection $\mathscr{P} : \mathbb{S}^{|\mathcal{V}|} \to \mathbb{S}^{|\mathcal{V}|}$ onto the sparsity pattern*

$$\mathcal{J} = \left\{ (i,j) \in \mathcal{V}\times\mathcal{V} : i = j \ \vee \ i,j \in \{\hat{\epsilon}(k), \check{\epsilon}(k)\}, k \in \mathcal{E} \right\} \tag{2.74}$$

be given by

$$\mathscr{P}(\boldsymbol{X}) = \sum_{(i,j)\in\mathcal{J}} [\boldsymbol{X}]_{i,j} \boldsymbol{e}_i \boldsymbol{e}_j^{\mathrm{T}} . \tag{2.75}$$

Then, for all matrices $\boldsymbol{X} \in \mathcal{K} \cup \{\boldsymbol{L}\}$,

$$\mathscr{P}(\boldsymbol{X}) = \boldsymbol{X} . \tag{2.76}$$

3 Optimal Power Flow

The *optimal power flow* (OPF) problem identifies the optimal utilization of the grid infrastructure and generation resources to satisfy the load, where optimality is typically considered with respect to minimum injection costs or minimum electrical losses, see also Chapter 1. With the system model for hybrid AC/DC grids presented in Chapter 2, the OPF problem can be stated as the following optimization problem:

$$\underset{\substack{\boldsymbol{s}_j \in \mathcal{S}_j,\, \boldsymbol{v} \in \mathcal{U} \\ \boldsymbol{f} \in \mathcal{F}}}{\text{minimize}} \quad \sum_{j \in \mathcal{I}} C_j(\boldsymbol{s}_j) + \tau L(\boldsymbol{v}\boldsymbol{v}^{\mathrm{H}}, \boldsymbol{f}) \tag{3.1a}$$

$$\text{subject to} \quad (2.42), (2.52), (2.55), (2.60), (2.67)\,. \tag{3.1b}$$

The optimization variables in this problem are the state (operating point) $\boldsymbol{s}_{\mathcal{I}}$ of the injectors and the state of the grid, where the latter consists of the bus voltages $\boldsymbol{v}$ and converter states $\boldsymbol{f}$. While the injector and converter states are restricted to the respective P/Q-capability region and the bus voltages to the respective state domain of AC and DC grids, the problem is further constrained by the power flow equations (2.42), which describe the physical behavior of the system, as well as the system's operating limits on bus voltages, branch currents, voltage drops, and angle differences in (2.52), (2.55), (2.60), and (2.67), respectively. The problem's objective consists of the total injection costs and a penalty term comprising the total electrical losses weighted by an (artificial) *loss price* $\tau \in \mathbb{R}_+$. This enables injection cost minimization, electrical loss minimization, and a combination of both. As shown by the following proposition, this objective can also be expressed with cost functions only. The penalty term is considered explicitly to study its impact mathematically and to offer a convenient parameterization in a practical implementation.

Proposition 1. *Consider the OPF problem* (3.1)*. Including a loss penalty with* $\tau > 0$ *is equivalent to increasing the marginal cost of active power by* τ *for all injectors* $j \in \mathcal{I}$*.*

Proof. Considering the definition of the electrical loss function L in (2.49) and its

derivation in (2.45), it follows that

$$\sum_{j\in\mathcal{I}} C_j(\boldsymbol{s}_j) + \tau L(\boldsymbol{v}\boldsymbol{v}^{\mathrm{H}}, \boldsymbol{f}) = \sum_{j\in\mathcal{I}} C_j(\boldsymbol{s}_j) + \tau \sum_{n\in\mathcal{V}} \boldsymbol{e}_1^{\mathrm{T}} \sum_{j\in\hat{\mathcal{B}}_{\mathcal{I}}(n)} \boldsymbol{s}_j$$
$$= \sum_{j\in\mathcal{I}} \left[C_j(\boldsymbol{s}_j) + \tau \boldsymbol{e}_1^{\mathrm{T}} \boldsymbol{s}_j \right] . \qquad \square$$

The cost functions C_j are typically either quadratic polynomials or *piecewise linear* (PWL) functions[4] and, if the PWL functions are included in *epigraph form* [42, Ch. 4.1.3], the OPF problem in (3.1) is a *quadratically-constrained quadratic problem* (QCQP). Moreover, as the power flow equations are quadratic in the bus voltages, the OPF problem is inherently a *nonconvex* QCQP. The *globally* optimal solution of a nonconvex QCQP is in general *NP-hard*[5] and, thus, practically intractable for large-scale problems. Still, this nonconvex OPF problem can be "solved" in practice rather efficiently using interior-point methods, which in general converge to a *local* optimum (see e.g. [87]). The locally optimal solution is typically regarded or, to emphasize the pragmatism, *taken* as sufficient. While local optima do exist in OPF problems [88], recent computational studies for large-scale systems considering convex relaxations show that the locally optimal solutions obtained with interior-point methods are often reasonably close to some lower bound on the optimal objective value, see e.g. [3, 58, 89]. Later in this chapter, convex relaxations and their induced lower bounds are discussed, but prior to that a *unified* OPF problem is presented, which considerably simplifies the mathematical exposition (and software implementation) later on.

3.1 Unified Optimal Power Flow Formulation for Hybrid AC/DC Grids

By virtue of the particular model formulation in Chapter 2, AC and DC subgrids are considered in a unified manner in the objective and constraints of the OPF problem (3.1), while their different physical nature is only explicit in the restriction of their state domain as captured by $\boldsymbol{v} \in \mathcal{U}$. With respect to convex relaxations and the Lagrangian dual domain, this restriction complicates further mathematical studies as it necessitates a differentiation of AC and DC subgrids. In the following, it

[4] These functions are known as piecewise *linear* even though the pieces are in general *affine*.

[5] An *NP-hard* problem is a problem to which an *NP-complete* problem can be transformed [85, Ch. 5]. Zero-one integer programming is known to be NP-complete [85, A6] and, as the zero-one restriction $x \in \{0, 1\}$ can be reformulated as the quadratic constraint $x(x-1) = 0$ with $x \in \mathbb{R}$ (see e.g. [86]), zero-one integer programming can be transformed to a nonconvex QCQP.

is shown that the state domain of AC and DC subgrids can be unified in (3.1) under some mild conditions and, therewith, the necessity to differentiate between AC and DC subgrids can be avoided.

To this end, it is observed that all currently installed and almost all planned HVDC systems are P2P-HVDC or *radial* MT-HVDC systems [14]. This observation is utilized for the unification and, for that purpose, formalized in Definition 12. Furthermore, let (2.62) also be imposed on DC subgrids, which is put with $\boldsymbol{A}_k$ in (2.68a) as

$$\boldsymbol{v}^{\mathrm{H}} \boldsymbol{A}_k \boldsymbol{v} \leq 0\,, \qquad \forall k \in \bar{\mathcal{E}}\,. \tag{3.2}$$

Definition 12 (Radial DC Subgrids)**.** The underlying undirected graph of the directed subgraph $\bar{\mathcal{G}} = \{\bar{\mathcal{V}}, \bar{\mathcal{E}}, \hat{\epsilon}, \check{\epsilon}\}$ is *acyclic* [82], i.e., its connected components are *trees* [82].

Jointly, Definition 12 and (3.2) enable the following results.

Lemma 1. *Consider any $\boldsymbol{f} \in \mathcal{F}$ and $\boldsymbol{s}_j \in \mathcal{S}_j$, for $j \in \mathcal{I}$. Let $\boldsymbol{v} \in \mathbb{C}^{|\mathcal{V}|}$ satisfy* (2.42) *for the given $\boldsymbol{f}$ and $\boldsymbol{s}_{\mathcal{I}}$. Then,* $\operatorname{Im}(V^*_{\hat{\epsilon}(k)} V_{\check{\epsilon}(k)}) = 0, \forall k \in \bar{\mathcal{E}}$.

Proof. For DC bus $n \in \bar{\mathcal{V}}$, it follows from the reactive power balance equation (2.42b) and the absence of reactive power at converters and injectors by Definition 8 and Definition 10 that $\boldsymbol{v}^{\mathrm{H}} \boldsymbol{Q}_n \boldsymbol{v} = 0$. With Definition 5 and Definition 7, this implies[6] that

$$\sum_{k \in \hat{\mathcal{B}}_{\mathcal{E}}(n)} \bar{y}_k \operatorname{Im}(V^*_{\check{\epsilon}(k)} V_n) \; + \sum_{k \in \check{\mathcal{B}}_{\mathcal{E}}(n)} \bar{y}_k \operatorname{Im}(V^*_{\hat{\epsilon}(k)} V_n) = 0\,. \tag{3.3}$$

Thus, if $\boldsymbol{v}$ is *not* restricted to $\mathcal{U}$, there may emerge a circulation of "artificial reactive power" in DC subgrids. Now, consider an individual DC subgrid, which is radial by Definition 12. Without loss of generality, assume that it comprises no parallel branches (consider their single branch equivalent), consider one of its buses as the reference bus, and let all its branches point toward this reference bus. At all leaf nodes n of this directed tree graph, (3.3) reduces to

$$\bar{y}_k \operatorname{Im}(V^*_{\check{\epsilon}(k)} V_n) = 0 \tag{3.4}$$

[6] Alternatively, (3.3) can be derived with the electrical model. For $n \in \bar{\mathcal{V}}$, using (2.11) in (2.22) considering the conductance-only branches and the absence of shunts by Definition 5 and 7 yields

$$I_n = \sum_{k \in \hat{\mathcal{B}}_{\mathcal{E}}(n)} \bar{y}_k (V_n - V_{\check{\epsilon}(k)}) \; + \sum_{k \in \check{\mathcal{B}}_{\mathcal{E}}(n)} \bar{y}_k (V_n - V_{\hat{\epsilon}(k)})\,.$$

With Definition 5 ($\bar{y}_k \in \mathbb{R}, \forall k \in \bar{\mathcal{E}}$), (3.3) follows directly from $\boldsymbol{v}^{\mathrm{H}} \boldsymbol{Q}_n \boldsymbol{v} = \operatorname{Im}(V_n I_n^*) = 0$.

where k is the *only* DC branch connected to DC bus $n = \hat{\epsilon}(k)$ due to Definition 12, Definition 4 (no self-loops), and the absence of parallel branches. It follows from Definition 6 (lossy DC branches) that $\bar{y}_k \neq 0$, thus (3.4) implies

$$\mathrm{Im}(V^*_{\check{\epsilon}(k)} V_{\hat{\epsilon}(k)}) = 0 \quad \Longrightarrow \quad \mathrm{Im}(V^*_{\hat{\epsilon}(k)} V_{\check{\epsilon}(k)}) = 0$$

i.e., the inflow of artificial reactive power arising from DC branch k at its destination bus $\check{\epsilon}(k)$ is zero. Therefore, all DC branches that are connected to leaf nodes do not contribute to the circulation of artificial reactive power and, thus, can be excluded for this analysis. Considering the resulting reduced directed tree graph, the above argument can be repeated until the reduced directed tree graph equals the reference node. This proves by induction that $\mathrm{Im}(V^*_{\hat{\epsilon}(k)} V_{\check{\epsilon}(k)}) = 0$ for all DC branches k of the considered DC subgrid. The repetition of this inductive argument for all DC subgrids implies that $\mathrm{Im}(V^*_{\hat{\epsilon}(k)} V_{\check{\epsilon}(k)}) = 0, \forall k \in \bar{\mathcal{E}}$. Note that the proof can be adapted to an arbitrary directionality of DC branches. □

Theorem 1. *Consider any $\boldsymbol{f} \in \mathcal{F}$ and $\boldsymbol{s}_j \in \mathcal{S}_j$, for $j \in \mathcal{I}$. Let $\boldsymbol{v} \in \mathbb{C}^{|\mathcal{V}|}$ satisfy the constraints in* (3.1b) *and* (3.2) *for the given $\boldsymbol{f}$ and $\boldsymbol{s}_{\mathcal{I}}$. Then, $\underline{\boldsymbol{v}} \in \mathcal{U}$ given by*

$$[\underline{\boldsymbol{v}}]_n = \begin{cases} [\boldsymbol{v}]_n & \text{if } n \in \tilde{\mathcal{V}} \\ |[\boldsymbol{v}]_n| & \text{if } n \in \bar{\mathcal{V}} \end{cases} \tag{3.5}$$

satisfies (3.1b) *and* (3.2) *for the given $\boldsymbol{f}$ and $\boldsymbol{s}_{\mathcal{I}}$ with equivalent constraint function values and $L(\underline{\boldsymbol{v}}\underline{\boldsymbol{v}}^{\mathrm{H}}, \boldsymbol{f}) = L(\boldsymbol{v}\boldsymbol{v}^{\mathrm{H}}, \boldsymbol{f})$.*

Proof. It follows from Lemma 1 that, for all $k \in \bar{\mathcal{E}}$,

$$\arg(V_{\check{\epsilon}(k)}) - \arg(V_{\hat{\epsilon}(k)}) = r\pi\,, \quad \text{for some } r \in \mathbb{Z}\,. \tag{3.6}$$

Furthermore, it follows from (3.2), which implements (2.62), that

$$-\frac{\pi}{2} \leq \arg(V_{\check{\epsilon}(k)}) - \arg(V_{\hat{\epsilon}(k)}) \leq \frac{\pi}{2}\,. \tag{3.7}$$

Jointly, (3.6) and (3.7) imply

$$\arg(V_{\hat{\epsilon}(k)}) = \arg(V_{\check{\epsilon}(k)})\,, \quad \forall k \in \bar{\mathcal{E}}\,. \tag{3.8}$$

Therefore, the phase of all elements in $\boldsymbol{v}$ associated with a certain DC subgrid is

equal. As the constraints in (3.1b) and (3.2) are quadratic[7] in $\boldsymbol{v}$ and the individual constraints only involve elements of $\boldsymbol{v}$ that are associated with the same subgrid,[8] it follows that these constraints are invariant with respect to a common phase shift of all elements in $\boldsymbol{v}$ for a certain subgrid. Thus, if $\boldsymbol{v}$ satisfies (3.1b) and (3.2), then $\underline{\boldsymbol{v}}$ in (3.5) satisfies (3.1b) and (3.2) with equivalent constraint function values, as its construction only involves a common phase shift in the individual DC subgrids. Furthermore, this implies that $L(\underline{\boldsymbol{v}}\underline{\boldsymbol{v}}^{\mathrm{H}}, \boldsymbol{f}) = L(\boldsymbol{v}\boldsymbol{v}^{\mathrm{H}}, \boldsymbol{f})$, as L equals the summation of the left-hand side of (2.42a). □

In words, Theorem 1 states that, under Definition 12 and the complementary constraints (3.2), the state domain of DC subgrids in the OPF problem (3.1) can be relaxed from the real numbers to the complex numbers, i.e., $\boldsymbol{v} \in \mathcal{U} \subset \mathbb{C}^{|\mathcal{V}|}$ can be relaxed to $\boldsymbol{v} \in \mathbb{C}^{|\mathcal{V}|}$. Thus, the state domain of AC and DC subgrids can be *unified*, while (3.5) provides the reconstruction of the associated (real-valued) DC voltages. By applying this result to (3.1), the following *unified OPF formulation* is obtained:

$$p^\star = \underset{\substack{\boldsymbol{s}_j \in \mathcal{S}_j,\, \boldsymbol{v} \in \mathbb{C}^{|\mathcal{V}|} \\ \boldsymbol{f} \in \mathcal{F}}}{\text{minimize}} \quad \sum_{j \in \mathcal{I}} C_j(\boldsymbol{s}_j) + \tau L(\boldsymbol{v}\boldsymbol{v}^{\mathrm{H}}, \boldsymbol{f}) \tag{3.9a}$$

$$\text{subject to} \quad (2.42), (2.52), (2.55), (2.60), (2.67), (3.2)\,. \tag{3.9b}$$

Concluding, for a more focused exposition later on, a set representation of the constraints in (3.9b) that also includes the restriction of $\boldsymbol{f}$ to $\mathcal{F}$ shall be introduced. To this end, let the polyhedral set $\mathcal{X}$ be defined as

$$\mathcal{X} = \Big\{ (\boldsymbol{V}, \boldsymbol{f}, \boldsymbol{s}_{\mathcal{I}}) \in \mathbb{S}^{|\mathcal{V}|} \times \mathbb{R}^{4|\mathcal{C}|} \times \mathbb{R}^2_{\mathcal{I}} : \tag{3.10a}$$

$$\operatorname{tr}(\boldsymbol{P}_n \boldsymbol{V}) + \boldsymbol{p}_n^{\mathrm{T}} \boldsymbol{f} = \boldsymbol{e}_1^{\mathrm{T}} \sum_{j \in \hat{\mathcal{B}}_{\mathcal{I}}(n)} \boldsymbol{s}_j\,, \qquad \forall n \in \mathcal{V} \tag{3.10b}$$

$$\operatorname{tr}(\boldsymbol{Q}_n \boldsymbol{V}) + \boldsymbol{q}_n^{\mathrm{T}} \boldsymbol{f} = \boldsymbol{e}_2^{\mathrm{T}} \sum_{j \in \hat{\mathcal{B}}_{\mathcal{I}}(n)} \boldsymbol{s}_j\,, \qquad \forall n \in \mathcal{V} \tag{3.10c}$$

$$\operatorname{tr}(\boldsymbol{C}_m \boldsymbol{V}) + \boldsymbol{c}_m^{\mathrm{T}} \boldsymbol{f} \leq b_m\,, \qquad \forall m \in \mathcal{M} \Big\} \tag{3.10d}$$

in which (3.10d) captures the inequality constraints (2.32), (2.52), (2.55), (2.60), (2.67),

[7] For $\boldsymbol{x}$ and $\underline{\boldsymbol{x}} = \boldsymbol{x}e^{\mathrm{i}\varphi}$ with $\varphi \in \mathbb{R}$, it follows that $\underline{\boldsymbol{x}}^{\mathrm{H}} \boldsymbol{A} \underline{\boldsymbol{x}} = e^{-\mathrm{i}\varphi} \boldsymbol{x}^{\mathrm{H}} \boldsymbol{A} \boldsymbol{x} e^{\mathrm{i}\varphi} = \boldsymbol{x}^{\mathrm{H}} \boldsymbol{A} \boldsymbol{x}$.

[8] Note that converters "decouple" the voltages of different subgrids. W.l.o.g., the buses can be numbered such that the coefficient matrices are block-diagonal (cf. Corollary 1), where each block relates to a subgrid. Footnote 7 applies per block, i.e., a blockwise phase shift does not affect the constraints.

and (3.2) using the cyclic property of the trace in (2.48). $\boldsymbol{C}_m$, $\boldsymbol{c}_m$, and b_m, with $m \in \mathcal{M} = \{1, \dots, |\mathcal{M}|\}$, are parameterized to reproduce these

$$|\mathcal{M}| = F + 2|\mathcal{V}| + 3|\mathcal{E}| + 4|\tilde{\mathcal{E}}| \tag{3.11}$$

inequality constraints. With $\mathcal{X}$ in (3.10), the unified OPF formulation in (3.9) can be expressed equivalently as

$$p^\star = \underset{\substack{\boldsymbol{s}_j \in \mathcal{S}_j,\, \boldsymbol{v} \in \mathbb{C}^{|\mathcal{V}|} \\ \boldsymbol{f} \in \mathbb{R}^{4|\mathcal{C}|}}}{\text{minimize}} \quad \sum_{j \in \mathcal{I}} C_j(\boldsymbol{s}_j) + \tau L(\boldsymbol{v}\boldsymbol{v}^{\mathrm{H}}, \boldsymbol{f}) \tag{3.12a}$$

$$\text{subject to} \quad (\boldsymbol{v}\boldsymbol{v}^{\mathrm{H}}, \boldsymbol{f}, \boldsymbol{s}_{\mathcal{I}}) \in \mathcal{X}\,. \tag{3.12b}$$

3.2 Convex Relaxation

In the past decades, optimization has made a lot of progress and for a special class of nonlinear problems, i.e., *convex* optimization problems, efficient polynomial-time algorithms for finite precision solutions exist, most notably interior-point methods [42]. A very strong property of convex optimization problems is that a *locally* optimal solution is also *globally* optimal (see e.g. [43, Theorem 3.4.2]), which is key to their efficient solvability to global optimality. Furthermore, under mild conditions that are collectively known as *constraint qualifications*, convex optimization problems share a strong relation with their *Lagrangian dual problem* (see also Chapter 5), which offers rich interpretations as well as powerful opportunities for solution methods, including problem decompositions that enable parallel and distributed computation [42, 43, 90, 91]. While these are only prominent advantages among others [42–46], they highlight the strong motivation to transform or approximate a nonconvex problem as a convex one.

A recent approach to shift the OPF problem into the convex domain without compromising model accuracy is *convex relaxation*, see the related discussion in Chapter 1. In the following, the two most prominent relaxation techniques in the context of OPF, i.e., the semidefinite and second-order cone relaxation, are applied to the OPF problem (3.12). In contrast to other works on such relaxations of the OPF problem for hybrid AC/DC grids [32, 33, 35], a distinctive feature of the presented relaxations is that they can be applied *without* explicitly considering the hybrid nature of the grid. This is enabled by the *unified* OPF formulation, which facilitates the direct generalization of relaxations for AC grids to hybrid AC/DC grids and promotes a particularly simple and concise derivation and result.

3.2.1 Semidefinite Relaxation

By definition, the objective in (3.12) and $\mathcal{S}_j$ are convex, while $\mathcal{X}$ is a polyhedral set and, thus, also convex. Hence, the nonconvexity of the OPF problem (3.12) arises from the quadratic dependence on the bus voltage vector $\boldsymbol{v}$. The outer product $\boldsymbol{v}\boldsymbol{v}^{\mathrm{H}}$ may be expressed equivalently by a Hermitian matrix $\boldsymbol{V} \in \mathbb{S}^{|\mathcal{V}|}$, which is *positive semidefinite* (psd)[9] and of rank 1. This observation enables the following equivalent formulation of the OPF problem (3.12), where an optimizer $(\boldsymbol{V}^\star, \boldsymbol{f}^\star, \boldsymbol{s}_{\mathcal{I}}^\star)$ always facilitates the factorization $\boldsymbol{V}^\star = \boldsymbol{v}^\star(\boldsymbol{v}^\star)^{\mathrm{H}}$ such that $(\boldsymbol{v}^\star, \boldsymbol{f}^\star, \boldsymbol{s}_{\mathcal{I}}^\star)$ is optimal in (3.12).

$$
\begin{aligned}
p^\star = \underset{\substack{\boldsymbol{s}_j \in \mathcal{S}_j,\, \boldsymbol{V} \in \mathbb{S}^{|\mathcal{V}|} \\ \boldsymbol{f} \in \mathbb{R}^{4|\mathcal{C}|}}}{\text{minimize}} \quad & \sum_{j \in \mathcal{I}} C_j(\boldsymbol{s}_j) + \tau L(\boldsymbol{V}, \boldsymbol{f}) && \text{(3.13a)} \\
\text{subject to} \quad & (\boldsymbol{V}, \boldsymbol{f}, \boldsymbol{s}_{\mathcal{I}}) \in \mathcal{X} && \text{(3.13b)} \\
& \boldsymbol{V} \succeq \boldsymbol{0} && \text{(3.13c)} \\
& \operatorname{rank}(\boldsymbol{V}) = 1\,. && \text{(3.13d)}
\end{aligned}
$$

As the set of psd matrices is a convex cone [42, Ch. 2.2.5], this reformulation lumps the nonconvexity to the rank constraint (3.13d). In *semidefinite relaxation* (SDR) [93], the rank constraint is omitted to obtain a convex optimization problem. Accordingly, the SDR of the OPF problem (3.12) reads

$$
\begin{aligned}
\hat{p}^\star = \underset{\substack{\boldsymbol{s}_j \in \mathcal{S}_j,\, \boldsymbol{V} \in \mathbb{S}^{|\mathcal{V}|} \\ \boldsymbol{f} \in \mathbb{R}^{4|\mathcal{C}|}}}{\text{minimize}} \quad & \sum_{j \in \mathcal{I}} C_j(\boldsymbol{s}_j) + \tau L(\boldsymbol{V}, \boldsymbol{f}) && \text{(3.14a)} \\
\text{subject to} \quad & (\boldsymbol{V}, \boldsymbol{f}, \boldsymbol{s}_{\mathcal{I}}) \in \mathcal{X} && \text{(3.14b)} \\
& \boldsymbol{V} \succeq \boldsymbol{0}\,. && \text{(3.14c)}
\end{aligned}
$$

Therewith, the OPF problem gains access to the powerful theory of convex analysis as well as solution algorithms with polynomial-time convergence to a globally optimal solution. By construction of the SDR, an optimizer $(\boldsymbol{V}^\star, \boldsymbol{f}^\star, \boldsymbol{s}_{\mathcal{I}}^\star)$ of (3.14) provides a solution to the OPF problem (3.12) if $\boldsymbol{V}^\star$ has rank 1, in which case the relaxation is called *exact*.[10] Furthermore, a direct consequence of the relaxation of the feasible set is the following relation of the optimal objective values.

[9] By definition, a matrix $\boldsymbol{A} \in \mathbb{S}^{|\mathcal{V}|}$ is psd if $\boldsymbol{A} \succeq \boldsymbol{0} \Leftrightarrow \boldsymbol{x}^{\mathrm{H}}\boldsymbol{A}\boldsymbol{x} \geq 0, \forall \boldsymbol{x} \in \mathbb{C}^{|\mathcal{V}|}$ [92]. Consequently, $\boldsymbol{v}\boldsymbol{v}^{\mathrm{H}}$ is psd as $\boldsymbol{x}^{\mathrm{H}}\boldsymbol{v}\boldsymbol{v}^{\mathrm{H}}\boldsymbol{x} = |\boldsymbol{x}^{\mathrm{H}}\boldsymbol{v}|^2 \geq 0, \forall \boldsymbol{x}, \boldsymbol{v} \in \mathbb{C}^{|\mathcal{V}|}$.

[10] More generally, due to voltage-decoupled subgrids an optimizer $\boldsymbol{V}^\star$ of the SDR (3.14) still allows exact recovery if it permits a decomposition $\boldsymbol{V}^\star = \sum_{i=1}^{N} \boldsymbol{v}_i \boldsymbol{v}_i^{\mathrm{H}}$, where N is the number of subgrids and $\boldsymbol{v}_i$ comprises only nonzero elements for bus voltages of subgrid i.

Corollary 2. *The optimal objective value $p^\star$ of the OPF problem* (3.12) *is bounded below by the optimal objective value $\hat{p}^\star$ of its SDR* (3.14)*, i.e., $p^\star \geq \hat{p}^\star$. If the SDR is* exact*, the bound is tight, i.e., $p^\star = \hat{p}^\star$.*

As first motivated in [51] for AC grids, exactness can be observed in many cases, but inexactness does occur frequently [3, 94–96]. Another issue of SDR is the quadratic increase in dimensionality by $|\mathcal{V}|^2 - 2|\mathcal{V}|$ (real-valued) variables, which impedes computational tractability for large-scale grids. Fortunately, as shown by Corollary 1 the coefficient matrices in (3.14) are sparse. This sparsity can be utilized to effectively solve (3.14) also for large-scale systems, e.g., via a *chordal conversion* [97], see also [95, 98–101].

3.2.2 Second-Order Cone Relaxation

As a means to mitigate the dimensionality uplift and improve computational efficiency, an additional *second-order cone relaxation* (SOCR) may be applied to an SDR [102] (see also the related works [103, 104]). To this end, it is observed that a necessary (but not sufficient) condition for $\boldsymbol{V} \succeq \mathbf{0}$ is that all 2×2 principal submatrices of $\boldsymbol{V}$ are psd [92, Ch. 7.1]. Consequently, (3.14c) may be *relaxed* to psd constraints on 2×2 principal submatrices, which can be implemented as second-order cone constraints. To illustrate the latter, consider the 2×2 principal submatrix of $\boldsymbol{V}$ for the index tuple $(i, j) \in \mathcal{V} \times \mathcal{V}$. For this Hermitian 2×2 matrix, nonnegativity of the trace (sum of eigenvalues) and determinant (product of eigenvalues) implies nonnegativity of its two eigenvalues, which in turn implies positive semidefiniteness. This equivalence can be stated as follows, where V_{kl} denotes $[\boldsymbol{V}]_{k,l}$ for better readability:

$$\begin{bmatrix} V_{ii} & V_{ij} \\ V_{ij}^* & V_{jj} \end{bmatrix} \succeq \mathbf{0} \quad \Leftrightarrow \quad V_{ii}, V_{jj} \geq 0 \text{ and } V_{ij}^* V_{ij} = \left\| \begin{bmatrix} \mathrm{Re}(V_{ij}) \\ \mathrm{Im}(V_{ij}) \end{bmatrix} \right\|^2 \leq V_{ii} V_{jj} \tag{3.15}$$

The formulation on the right characterizes a *rotated second-order cone*, which can be reformulated as a (standard) second-order cone constraint, see e.g. [105, Sec. 2.3]. By untying the constraint (3.14c) with this additional relaxation, the sparsity of the coefficient matrices in Corollary 1 can be directly exploited and only the 2×2 principal submatrices that coincide with the sparsity pattern need to be retained. This enables a dimensionality reduction by $|\mathcal{V}|^2 - |\mathcal{J}|$ (real-valued) optimization variables, where the sparsity pattern $\mathcal{J}$ in (2.74) is specified by the system's network topology.

In order to formulate the SOCR of (3.14), let the set $\tilde{\mathbb{S}}^{|\mathcal{V}|}$ of Hermitian partial

matrices with the sparsity pattern $\mathcal{J}$ be defined as

$$\tilde{\mathbb{S}}^{|\mathcal{V}|} = \{\mathscr{P}(\boldsymbol{V}) : \boldsymbol{V} \in \mathbb{S}^{|\mathcal{V}|}\} \subseteq \mathbb{S}^{|\mathcal{V}|} \tag{3.16}$$

where the projection $\mathscr{P}$ onto the sparsity pattern is given in (2.75). Furthermore, let

$$\boldsymbol{S}_k = [\boldsymbol{e}_{\hat{\varepsilon}(k)}, \boldsymbol{e}_{\check{\varepsilon}(k)}] \in \mathbb{R}^{|\mathcal{V}|\times 2} \tag{3.17}$$

such that $\boldsymbol{S}_k^{\mathrm{T}} \boldsymbol{V} \boldsymbol{S}_k$ selects the 2×2 principal submatrix of $\boldsymbol{V}$ associated with branch $k \in \mathcal{E}$. Therewith, the SOCR of the SDR (3.14) and, thus, of the OPF problem (3.12) can be stated as

$$\tilde{p}^\star = \underset{\substack{\boldsymbol{s}_j \in \mathcal{S}_j,\, \boldsymbol{V} \in \tilde{\mathbb{S}}^{|\mathcal{V}|} \\ \boldsymbol{f} \in \mathbb{R}^{4|\mathcal{C}|}}}{\text{minimize}} \quad \sum_{j\in\mathcal{I}} C_j(\boldsymbol{s}_j) + \tau L(\boldsymbol{V}, \boldsymbol{f}) \tag{3.18a}$$

$$\text{subject to} \quad (\boldsymbol{V}, \boldsymbol{f}, \boldsymbol{s}_\mathcal{I}) \in \mathcal{X} \tag{3.18b}$$

$$\boldsymbol{S}_k^{\mathrm{T}} \boldsymbol{V} \boldsymbol{S}_k \succeq \boldsymbol{0}, \quad k \in \mathcal{E}\,. \tag{3.18c}$$

Compared to the SDR, even with a chordal conversion, the dimensionality reduction and formulation as a second-order cone program reduces the computational complexity for (meshed) medium- and large-scale systems significantly as evident in [3].[11] By construction of the SOCR, an optimizer $(\boldsymbol{V}^\star, \boldsymbol{f}^\star, \boldsymbol{s}_\mathcal{I}^\star)$ of (3.18) provides a solution to the OPF problem (3.12) if $\boldsymbol{V}^\star$ permits a rank-1 completion, in which case the relaxation is called *exact*. However, being a relaxation of the SDR, exactness of the SOCR is observed less frequently than with the SDR. Furthermore, a direct consequence of the additional relaxation of the feasible set is the following relation of the optimal objective values.

Corollary 3. *The optimal objective value $\hat{p}^\star$ of the SDR* (3.14) *is bounded below by the optimal objective value $\tilde{p}^\star$ of its SOCR* (3.18)*, i.e., $\hat{p}^\star \geq \tilde{p}^\star$, and thus $p^\star \geq \hat{p}^\star \geq \tilde{p}^\star$. If the SOCR is* exact*, the bound is tight, i.e., $p^\star = \hat{p}^\star = \tilde{p}^\star$.*

[11] Note that the SDR with a chordal conversion for a system with radial subgrids, which induce a sparsity pattern associated with an *acyclic* (and, thus, chordal) graph with maximal cliques that comprise two vertices, reduces structurally to the SOCR, cf. [97].

4 Locational Marginal Pricing

The decision making implied by the OPF problem, which yields the optimal dispatch of the generation resources, aligns with centralized operation and, thus, with vertically integrated (monopoly) electric utilities. With the deregulation of the electric utility sector, the centralized decision making experiences a transition into liberalized electricity markets. In these markets, *nodal pricing* is an instrument to account for system constraints and losses [39, 106–108]. The limitations on the power flow in a congested grid impose restrictions on trades and electrical losses distort the balance of supply and demand, which is reflected by bus-dependent (nodal) prices for electric power. For a market with *perfect competition*, i.e., when all market participants are price takers and do not exert market power, the optimal nodal prices equal the *locational marginal prices* (LMPs) [39]. The marginal price of active power at a bus corresponds to the cost of serving an increment of load by the cheapest possible means of generation [39], i.e., LMPs capture the sensitivity of the minimum total generation cost to load variations. Accordingly, LMPs are tightly related to cost-minimizing OPF problems. In particular, LMPs quantify the sensitivity of the optimal objective value of the OPF problem with respect to the nodal power balance constraints.

In general, accurate LMPs are hard to obtain due to the nonconvexity of the OPF problem [109, 110]. As a consequence, LMPs are commonly determined on the basis of the simplified and linearized system model for AC grids known as the "DC power flow", which is discussed in Chapter 1. The OPF formulation based on the "DC power flow" is known as the "DC OPF" and constitutes a linear program. Due to strong duality in linear programs, the associated approximation of LMPs is given by the Lagrangian dual variables of the power balance constraints [39], which are efficiently computed, e.g., using an interior-point method. However, due to the model mismatch these approximate LMPs are potentially inaccurate and may induce constraint-violating power flows, necessitating compensation measures [111].

In the following, it is shown in what manner and under which conditions LMPs

are related to the nonconvex OPF problem (3.12) and its Lagrangian dual problem. Subsequently, the convex relaxations of the OPF problem in the previous chapter are considered, for which it is shown that they serve as an efficient means to compute the LMPs under exactness of the relaxation. This illustrates that the advantages arising from convex relaxation are not limited to computational aspects and, later on, it enables valuable insights that permit a characterization of exactness. The following exposition is based on our work in [2], which is generalized to the system model in Chapter 2 using the *unified* OPF formulation enabled by Theorem 1. This permits a discussion of LMPs *without* explicitly considering the hybrid nature of the grid.

4.1 Relation of the OPF Problem and Locational Marginal Prices

In order to relate the OPF problem to LMPs, the *Lagrangian dual problem* [42, 43] of the OPF problem (3.12) is considered. To this end, the active and reactive power balance constraints (3.10b) and (3.10c) are dualized using the dual variables $\boldsymbol{\lambda}_n \in \mathbb{R}^2$, with $n \in \mathcal{V}$, and the system constraints in (3.10d) are dualized using $\boldsymbol{\mu} \in \mathbb{R}_+^{|\mathcal{M}|}$. With the definition of the total electrical loss function in (2.49) and $\boldsymbol{b} = [b_1, \dots, b_{|\mathcal{M}|}]^{\mathrm{T}}$, the associated *Lagrangian function* $\mathscr{L} : \mathbb{C}^{|\mathcal{V}|} \times \mathbb{R}^{4|\mathcal{C}|} \times \mathcal{S}_{\mathcal{I}} \times \mathbb{R}^2_{\mathcal{V}} \times \mathbb{R}_+^{|\mathcal{M}|} \to \mathbb{R}$ reads

$$\begin{aligned}\mathscr{L}(\boldsymbol{v}, \boldsymbol{f}, \boldsymbol{s}_{\mathcal{I}}, \boldsymbol{\lambda}_{\mathcal{V}}, \boldsymbol{\mu}) = \sum_{j \in \mathcal{I}} C_j(\boldsymbol{s}_j) + \tau(\boldsymbol{v}^{\mathrm{H}} \boldsymbol{L} \boldsymbol{v} + \boldsymbol{l}^{\mathrm{T}} \boldsymbol{f}) \\ + \sum_{n \in \mathcal{V}} [\boldsymbol{\lambda}_n]_1 \Big[\boldsymbol{v}^{\mathrm{H}} \boldsymbol{P}_n \boldsymbol{v} + \boldsymbol{p}_n^{\mathrm{T}} \boldsymbol{f} - \boldsymbol{e}_1^{\mathrm{T}} \sum_{j \in \hat{\mathcal{B}}_{\mathcal{I}}(n)} \boldsymbol{s}_j \Big] \\ + \sum_{n \in \mathcal{V}} [\boldsymbol{\lambda}_n]_2 \Big[\boldsymbol{v}^{\mathrm{H}} \boldsymbol{Q}_n \boldsymbol{v} + \boldsymbol{q}_n^{\mathrm{T}} \boldsymbol{f} - \boldsymbol{e}_2^{\mathrm{T}} \sum_{j \in \hat{\mathcal{B}}_{\mathcal{I}}(n)} \boldsymbol{s}_j \Big] \\ + \sum_{m \in \mathcal{M}} [\boldsymbol{\mu}]_m \Big[\boldsymbol{v}^{\mathrm{H}} \boldsymbol{C}_m \boldsymbol{v} + \boldsymbol{c}_m^{\mathrm{T}} \boldsymbol{f} - b_m \Big] \qquad (4.1)\end{aligned}$$

$$\begin{aligned}= \sum_{j \in \mathcal{I}} \Big(C_j(\boldsymbol{s}_j) - \boldsymbol{\lambda}_{\hat{n}(j)}^{\mathrm{T}} \boldsymbol{s}_j \Big) \\ + \boldsymbol{v}^{\mathrm{H}} \Psi(\boldsymbol{\lambda}_{\mathcal{V}}, \boldsymbol{\mu}) \boldsymbol{v} + \psi(\boldsymbol{\lambda}_{\mathcal{V}}, \boldsymbol{\mu})^{\mathrm{T}} \boldsymbol{f} - \boldsymbol{\mu}^{\mathrm{T}} \boldsymbol{b} \qquad (4.2)\end{aligned}$$

in which $\Psi : \mathbb{R}^2_{\mathcal{V}} \times \mathbb{R}^{|\mathcal{M}|} \to \mathbb{S}^{|\mathcal{V}|}$ and $\psi : \mathbb{R}^2_{\mathcal{V}} \times \mathbb{R}^{|\mathcal{M}|} \to \mathbb{R}^{4|\mathcal{C}|}$ are given by

$$\Psi(\boldsymbol{\lambda}_{\mathcal{V}}, \boldsymbol{\mu}) = \sum_{n \in \mathcal{V}} \Big(([\boldsymbol{\lambda}_n]_1 + \tau) \boldsymbol{P}_n + [\boldsymbol{\lambda}_n]_2 \boldsymbol{Q}_n \Big) + \sum_{m \in \mathcal{M}} [\boldsymbol{\mu}]_m \boldsymbol{C}_m \qquad (4.3a)$$

$$\psi(\boldsymbol{\lambda}_\mathcal{V}, \boldsymbol{\mu}) = \sum_{n\in\mathcal{V}} \Big(([\boldsymbol{\lambda}_n]_1 + \tau)\boldsymbol{p}_n + [\boldsymbol{\lambda}_n]_2 \boldsymbol{q}_n \Big) \; + \sum_{m\in\mathcal{M}} [\boldsymbol{\mu}]_m \boldsymbol{c}_m \tag{4.3b}$$

and utilize the definition of $\boldsymbol{L}$ and $\boldsymbol{l}$ in (2.46) and (2.47) as the sum of all $\boldsymbol{P}_n$ and $\boldsymbol{p}_n$, respectively. The associated *Lagrangian dual function* $\theta : \mathbb{R}^2_\mathcal{V} \times \mathbb{R}_+^{|\mathcal{M}|} \to \mathbb{R}$ is thus

$$\begin{aligned}\theta(\boldsymbol{\lambda}_\mathcal{V}, \boldsymbol{\mu}) &= \inf_{\substack{\boldsymbol{s}_j \in \mathcal{S}_j \\ \boldsymbol{v}\in\mathbb{C}^{|\mathcal{V}|} \\ \boldsymbol{f}\in\mathbb{R}^{4|\mathcal{C}|}}} \mathscr{L}(\boldsymbol{v}, \boldsymbol{f}, \boldsymbol{s}_\mathcal{I}, \boldsymbol{\lambda}_\mathcal{V}, \boldsymbol{\mu}) \\ &= \begin{cases} -\sum_{j\in\mathcal{I}} \pi_j(\boldsymbol{\lambda}_{\hat{n}(j)}) - \boldsymbol{\mu}^\mathrm{T}\boldsymbol{b} & \text{if } \Psi(\boldsymbol{\lambda}_\mathcal{V}, \boldsymbol{\mu}) \succeq \mathbf{0} \;\wedge\; \psi(\boldsymbol{\lambda}_\mathcal{V}, \boldsymbol{\mu}) = \mathbf{0} \\ -\infty & \text{otherwise} \end{cases}\end{aligned} \tag{4.4}$$

in which $\pi_j : \mathbb{R}^2 \to \mathbb{R}$ is given by

$$\begin{aligned}\pi_j(\boldsymbol{\lambda}) &= -\inf_{\boldsymbol{s}_j\in\mathcal{S}_j} \big\{ C_j(\boldsymbol{s}_j) - \boldsymbol{\lambda}^\mathrm{T}\boldsymbol{s}_j \big\} \\ &= \max_{\boldsymbol{s}_j\in\mathcal{S}_j} \big\{ \boldsymbol{\lambda}^\mathrm{T}\boldsymbol{s}_j - C_j(\boldsymbol{s}_j) \big\}\end{aligned} \tag{4.5}$$

where the second equality considers the existence of the solution (cf. Weierstrass's theorem [43, Ch. 2.3]) and reformulates the minimization as an equivalent maximization. Therewith, the *Lagrangian dual problem* of the OPF problem (3.12), which is the supremum of the dual function over the feasible dual variables, can be stated as

$$d^\star = -\operatorname*{minimize}_{\boldsymbol{\lambda}_n\in\mathbb{R}^2,\, \boldsymbol{\mu}\in\mathbb{R}_+^{|\mathcal{M}|}} \; \sum_{j\in\mathcal{I}} \pi_j(\boldsymbol{\lambda}_{\hat{n}(j)}) + \boldsymbol{\mu}^\mathrm{T}\boldsymbol{b} \tag{4.6a}$$

$$\text{subject to} \quad \Psi(\boldsymbol{\lambda}_\mathcal{V}, \boldsymbol{\mu}) \succeq \mathbf{0} \tag{4.6b}$$

$$\psi(\boldsymbol{\lambda}_\mathcal{V}, \boldsymbol{\mu}) = \mathbf{0}\,. \tag{4.6c}$$

Now, let $(\boldsymbol{v}^\star, \boldsymbol{f}^\star, \boldsymbol{s}^\star_\mathcal{I}, \boldsymbol{\lambda}^\star_\mathcal{V}, \boldsymbol{\mu}^\star)$ be a primal and dual optimal solution of (3.12) and (4.6), i.e., $(\boldsymbol{v}^\star, \boldsymbol{f}^\star, \boldsymbol{s}^\star_\mathcal{I})$ is an optimizer of the nonconvex OPF problem (3.12) and $(\boldsymbol{\lambda}^\star_\mathcal{V}, \boldsymbol{\mu}^\star)$ an optimizer of its convex Lagrangian dual problem (4.6). If and only if *strong duality* holds, i.e., the optimal objective values satisfy $p^\star = d^\star$ or, in other words, the *duality gap* $p^\star - d^\star$ is zero, then this primal and dual optimal solution is a *saddle point* of the Lagrangian function (cf. [43, Theorem 6.2.5]). Consequently, the primal variables $(\boldsymbol{v}^\star, \boldsymbol{f}^\star, \boldsymbol{s}^\star_\mathcal{I})$ minimize the Lagrangian function at the dual variables $(\boldsymbol{\lambda}^\star_\mathcal{V}, \boldsymbol{\mu}^\star)$ and, hence, they satisfy some respective first-order optimality conditions.

At this point, it is important to consider the domain of the Lagrangian function, which is constrained by the domain $\mathcal{S}_j$ of the injector cost function C_j, for all $j \in \mathcal{I}$. Furthermore, also on $\mathrm{int}(\mathcal{S}_j)$ the cost function C_j is in general not continuously differentiable. In a managed spot market, the market operator collects the bids and offers of producers and consumers, respectively, to set the nodal prices and clear the market [39]. The bids and offers are in general increasing and decreasing staircase-shaped price-power curves that, by integration, translate to convex PWL injector cost functions (cf. e.g. [110]), which are not differentiable at the breakpoints. Still, for given dual variables the Lagrangian function is convex and *subdifferentiable* in $\boldsymbol{s}_j$.[12] The definition of a *subgradient* (see e.g. [43, Ch. 3.2]) thus implies the optimality condition

$$\mathbf{0} \in \partial_{\boldsymbol{s}_j} \mathscr{L}(\boldsymbol{v}^\star, \boldsymbol{f}^\star, \boldsymbol{s}_{\mathcal{I}}^\star, \boldsymbol{\lambda}_{\mathcal{V}}^\star, \boldsymbol{\mu}^\star) = \partial C_j(\boldsymbol{s}_j^\star) - \{\boldsymbol{\lambda}_{\hat{n}(j)}^\star\} \tag{4.7}$$

which is equivalent to

$$\boldsymbol{\lambda}_{\hat{n}(j)}^\star \in \partial C_j(\boldsymbol{s}_j^\star)\,. \tag{4.8}$$

Furthermore, if C_j is differentiable at $\boldsymbol{s}_j^\star$, then $\partial C_j(\boldsymbol{s}_j^\star) = \{\nabla C_j(\boldsymbol{s}_j^\star)\}$ and thus

$$\boldsymbol{\lambda}_{\hat{n}(j)}^\star = \nabla C_j(\boldsymbol{s}_j^\star)\,. \tag{4.9}$$

Summarizing, strong duality implies a saddle point of the Lagrangian function which itself implies (4.8) and, under differentiability, (4.9). The latter two relations illustrate that, under strong duality, the dual variables $\boldsymbol{\lambda}_{\mathcal{V}}^\star$ capture the *marginal cost* of injection at the optimal dispatch $\boldsymbol{s}_{\mathcal{I}}^\star$. Furthermore, with $\tau = 0$ in the OPF problem (3.12), the dispatch $\boldsymbol{s}_{\mathcal{I}}^\star$ is cost-minimizing and, therefore, the dual variables $\boldsymbol{\lambda}_{\mathcal{V}}^\star$ capture the LMPs. With the interpretation of $\boldsymbol{\lambda}_n$ as the nodal price at bus $n \in \mathcal{V}$, π_j in (4.5) can be identified as the *injector's profit function* (and, thus, the dual problem aims to minimize the total profit). This explains the suitability of $\boldsymbol{\lambda}_{\mathcal{V}}^\star$ as *nodal prices*: If the injectors act profit-maximizing, the nodal prices $\boldsymbol{\lambda}_{\mathcal{V}}^\star$ incentivize a behavior that minimizes the total injection cost (and, thus, maximizes the system's *economic welfare* [39]), as then $\boldsymbol{s}_j^\star$ is a maximizer in (4.5) by (4.8). In case of a loss penalty $\tau > 0$ in the OPF problem (3.12), these considerations apply analogously, with the

[12] Any convex function is subdifferentiable on the *interior* of its domain, see [43, Th. 3.2.5]. This proof is based on the *supporting hyperplane theorem*, which utilizes the fact that the element μ of the hyperplane's normal vector that relates to the ordinate of the epigraph is negative. While $\mu \not> 0$ follows from the definition of the epigraph, $\mu \neq 0$ is shown by contradiction using the fact that the point of interest lies in the interior. In fact, $\mu = 0$ if the supporting hyperplane is parallel to the ordinate. By the Lipschitz continuity of C_j, this is also prevented at the boundary, which extends the result to $\mathcal{S}_j$.

nodal prices incentivizing a behavior toward optimality in the hybrid objective. As visible in (4.3), this is reflected by a translation of the dual variable's sensitivity to the active power flow into grid (see also Proposition 1 for the opposite perspective).

On the contrary, if the duality gap is *nonzero*, the primal-dual optimal solution does *not* constitute a saddle point of the Lagrangian and, hence, $\boldsymbol{\lambda}_{\mathcal{V}}^{\star}$ may not match the LMPs, i.e., the coupling between the dual variables and LMPs is in general invalidated.

4.2 Convex Relaxation

The preceding discussion shows that the computation of LMPs with the OPF problem (3.12) requires (a) the globally optimal solution of the Lagrangian dual problem (4.6) and (b) strong duality, i.e., a zero duality gap. As Lagrangian dual problems are convex by construction, (a) is in general tractable. For example, with the commonly employed quadratic or PWL injector cost functions, (4.6) can be expressed as a *semidefinite program* (SDP), for which efficient solution methods are readily available [42, 112, 113]. However, due to the nonconvexity of the OPF problem, (b) represents a substantial impediment. While *convex* optimization problems typically exhibit strong duality (except in pathological cases whose absence can be ensured by *constraint qualifications*), this is in general *not* the case with nonconvex problems [42, 43]. Thus, as strong duality is not established by the structure of the problem, it needs to be verified by evaluating the duality gap. This requires the globally optimal solution of the OPF problem, which is in general not tractable, cf. the discussion in Chapter 3.

In Section 3.2, two convex relaxations of the OPF problem (3.12) are presented that, in case of exactness, enable an efficient globally optimal solution of the OPF problem with polynomial-time algorithms. In what follows, it is shown that these convex relaxations themselves exhibit strong ties to the LMPs and, by virtue of this, may be utilized directly for an efficient computation of LMPs.

4.2.1 Semidefinite Relaxation

Similar to before, the *Lagrangian dual problem* of the SDR (3.14) is considered to relate it to LMPs. In this context, it is important to recognize that the psd constraint (3.14c) is a so-called *generalized inequality* [42, Ch. 2.4]. Analogously to scalar-valued inequalities, the standard form of optimization problems with generalized inequalities considers zero-sublevel sets (here, $-\boldsymbol{V} \preceq \mathbf{0}$). Such a generalized inequality is then dualized by taking the inner product of the constraint function with a Lagrangian dual variable from the *dual cone* [42, Ch. 2.6] of the proper cone on which the generalized

inequality is defined [42, Ch. 5.9].[13] The matrix inequality (3.14c) is with respect to the set of psd matrices, where the latter is a proper and *self-dual* cone [42, Ch. 2.6], i.e., the dual variable is a psd matrix. Correspondingly, (3.14c) is dualized with $\boldsymbol{\Lambda} \succeq \mathbf{0}$, while (3.10b), (3.10c), and (3.10d) are dualized with $\boldsymbol{\lambda}_{\mathcal{V}} \in \mathbb{R}^2_{\mathcal{V}}$ and $\boldsymbol{\mu} \in \mathbb{R}_+^{|\mathcal{M}|}$ as before. The *Lagrangian function* $\hat{\mathscr{L}} : \mathbb{S}^{|\mathcal{V}|} \times \mathbb{R}^{4|\mathcal{C}|} \times \mathcal{S}_{\mathcal{I}} \times \mathbb{S}_+^{|\mathcal{V}|} \times \mathbb{R}^2_{\mathcal{V}} \times \mathbb{R}_+^{|\mathcal{M}|} \to \mathbb{R}$ thus reads

$$\begin{aligned}
\hat{\mathscr{L}}(\boldsymbol{V}, \boldsymbol{f}, \boldsymbol{s}_{\mathcal{I}}, \boldsymbol{\Lambda}, \boldsymbol{\lambda}_{\mathcal{V}}, \boldsymbol{\mu}) = \sum_{j \in \mathcal{I}} & C_j(\boldsymbol{s}_j) + \tau(\operatorname{tr}(\boldsymbol{L}\boldsymbol{V}) + \boldsymbol{l}^{\mathrm{T}}\boldsymbol{f}) + \operatorname{tr}(\boldsymbol{\Lambda}(-\boldsymbol{V})) \\
& + \sum_{n \in \mathcal{V}} [\boldsymbol{\lambda}_n]_1 \Big[\operatorname{tr}(\boldsymbol{P}_n \boldsymbol{V}) + \boldsymbol{p}_n^{\mathrm{T}} \boldsymbol{f} - \boldsymbol{e}_1^{\mathrm{T}} \sum_{j \in \hat{\mathcal{B}}_{\mathcal{I}}(n)} \boldsymbol{s}_j \Big] \\
& + \sum_{n \in \mathcal{V}} [\boldsymbol{\lambda}_n]_2 \Big[\operatorname{tr}(\boldsymbol{Q}_n \boldsymbol{V}) + \boldsymbol{q}_n^{\mathrm{T}} \boldsymbol{f} - \boldsymbol{e}_2^{\mathrm{T}} \sum_{j \in \hat{\mathcal{B}}_{\mathcal{I}}(n)} \boldsymbol{s}_j \Big] \\
& + \sum_{m \in \mathcal{M}} [\boldsymbol{\mu}]_m \Big[\operatorname{tr}(\boldsymbol{C}_m \boldsymbol{V}) + \boldsymbol{c}_m^{\mathrm{T}} \boldsymbol{f} - b_m \Big] \\
= \sum_{j \in \mathcal{I}} & \Big(C_j(\boldsymbol{s}_j) - \boldsymbol{\lambda}_{\hat{n}(j)}^{\mathrm{T}} \boldsymbol{s}_j \Big) - \boldsymbol{\mu}^{\mathrm{T}} \boldsymbol{b} \\
& + \operatorname{tr}((\Psi(\boldsymbol{\lambda}_{\mathcal{V}}, \boldsymbol{\mu}) - \boldsymbol{\Lambda})\boldsymbol{V}) + \psi(\boldsymbol{\lambda}_{\mathcal{V}}, \boldsymbol{\mu})^{\mathrm{T}} \boldsymbol{f}
\end{aligned} \tag{4.10}$$

Similar as before, the definition of $\boldsymbol{L}$ and $\boldsymbol{l}$ in (2.46) and (2.47) is utilized and Ψ and ψ read as in (4.3). The *Lagrangian dual function* $\hat{\theta} : \mathbb{S}_+^{|\mathcal{V}|} \times \mathbb{R}^2_{\mathcal{V}} \times \mathbb{R}_+^{|\mathcal{M}|} \to \mathbb{R}$ is then

$$\begin{aligned}
\hat{\theta}(\boldsymbol{\Lambda}, \boldsymbol{\lambda}_{\mathcal{V}}, \boldsymbol{\mu}) &= \inf_{\substack{\boldsymbol{s}_j \in \mathcal{S}_j \\ \boldsymbol{V} \in \mathbb{S}^{|\mathcal{V}|} \\ \boldsymbol{f} \in \mathbb{R}^{4|\mathcal{C}|}}} \hat{\mathscr{L}}(\boldsymbol{V}, \boldsymbol{f}, \boldsymbol{s}_{\mathcal{I}}, \boldsymbol{\Lambda}, \boldsymbol{\lambda}_{\mathcal{V}}, \boldsymbol{\mu}) \\
&= \begin{cases} -\sum_{j \in \mathcal{I}} \pi_j(\boldsymbol{\lambda}_{\hat{n}(j)}) - \boldsymbol{\mu}^{\mathrm{T}} \boldsymbol{b} & \text{if } \Psi(\boldsymbol{\lambda}_{\mathcal{V}}, \boldsymbol{\mu}) - \boldsymbol{\Lambda} = \mathbf{0} \ \wedge \ \psi(\boldsymbol{\lambda}_{\mathcal{V}}, \boldsymbol{\mu}) = \mathbf{0} \\ -\infty & \text{otherwise} \end{cases}
\end{aligned} \tag{4.11}$$

with π_j in (4.5). In (4.11), it can be observed that the dual variable $\boldsymbol{\Lambda} \succeq \mathbf{0}$ serves the purpose of a *slack variable*. Therewith, it follows that the *Lagrangian dual problem* of the SDR (3.14), which is the supremum of the dual function $\hat{\theta}$, is *equivalent* to the Lagrangian dual problem of the OPF problem in (4.6).

[13] The selection of the Lagrangian dual variable from the dual cone is readily motivated by deriving the dual problem as a lower bound on the optimal objective value that results in *weak duality*, cf. [112].

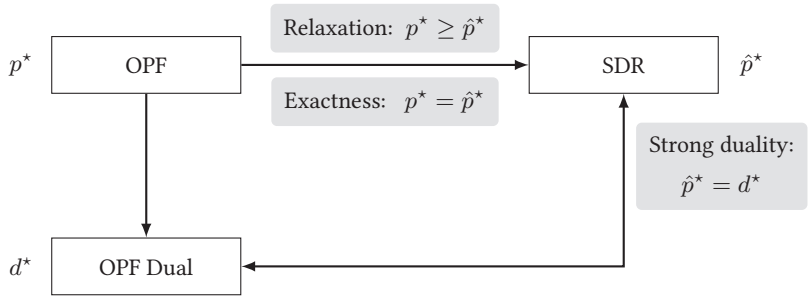

Figure 4.1: Relation of the OPF problem (3.12), the SDR (3.14), and their dual (4.6).

This particular property of the SDR (3.14), jointly with Corollary 2, implies a direct relation to LMPs as illustrated in Figure 4.1: If the SDR is *exact* and *strong duality* obtains, it follows that $p^\star = \hat{p}^\star = d^\star$ and, hence, the OPF problem (3.12) exhibits a *zero duality gap* (see also [51]) and the optimal dual variables $\boldsymbol{\lambda}_{\mathcal{V}}^\star$ constitute the LMPs. As strong duality usually obtains in convex problems, this relation essentially hinges on the exactness of the relaxation. Summarizing, certifying the dual variables as LMPs by verifying the exactness of the relaxation and determining the LMPs can be accomplished by jointly solving the SDR (3.14) and its Lagrangian dual (4.6) with a primal-dual interior-point method. Still, the computational challenges due to the increase in dimensionality during relaxation as discussed in Section 3.2.1 remain, which motivates the study whether the computationally more efficient SOCR also exhibits a relation to the LMPs.

Prior to that, it shall be shown that under some reasonable conditions strong duality can be formally ensured in the SDR (3.14) *a priori*.[14] The absence of a pathological case in which strong duality may not hold can be ensured by *constraint qualifications*, where *Slater's constraint qualification* [42, Ch. 5.2.3 and Ch. 5.9] is often employed due to its simplicity. Suppose the OPF problem (3.12) is essentially strictly feasible, then Slater's constraint qualification holds and strong duality obtains as shown below.

Assumption 1 (Essentially Strictly Feasible OPF Problem)**.** There exists a point $(\boldsymbol{V}, \boldsymbol{f}, \boldsymbol{s}_{\mathcal{I}}) \in \mathcal{X}$ for which (3.10d) holds strictly if $\boldsymbol{C}_m \neq \mathbf{0}$ and $\hat{\boldsymbol{s}}_n \in \operatorname{int}(\hat{\mathcal{S}}_n), \forall n \in \tilde{\mathcal{V}}$, and $\hat{\boldsymbol{s}}_n \in \operatorname{relint}(\hat{\mathcal{S}}_n), \forall n \in \bar{\mathcal{V}}$, where $\hat{\boldsymbol{s}}_n = \sum_{j \in \hat{\mathcal{B}}_{\mathcal{I}}(n)} \boldsymbol{s}_j$ and $\hat{\mathcal{S}}_n = \sum_{j \in \hat{\mathcal{B}}_{\mathcal{I}}(n)} \mathcal{S}_j$.

Proposition 2. *Under Assumption 1, strong duality is guaranteed in the SDR* (3.14).

Proof. In (3.14), all constraints are affine in the optimization variables and, hence, Slater's constraint qualification is satisfied if there exists a feasible point $(\boldsymbol{V}, \boldsymbol{f}, \boldsymbol{s}_{\mathcal{I}})$

[14] In practice, usually an interior-point method is used that solves the primal and dual simultaneously, enabling the verification of a (numerically) zero duality gap for the given problem instance *a posteriori*.

in (3.14) for which (3.14c) holds strictly, i.e., $\boldsymbol{V} \succ \boldsymbol{0}$. Consider the feasible point $(\boldsymbol{V}, \boldsymbol{f}, \boldsymbol{s}_{\mathcal{I}})$ in Assumption 1 and let $\bar{\boldsymbol{V}} = \boldsymbol{V} + \varepsilon \boldsymbol{I}$, where $\varepsilon > 0$ is an arbitrary positive scalar and $\boldsymbol{I}$ is the $|\mathcal{V}| \times |\mathcal{V}|$ identity matrix. Consequently,

$$\operatorname{tr}(\boldsymbol{P}_n \bar{\boldsymbol{V}}) + \boldsymbol{p}_n^{\mathrm{T}} \boldsymbol{f} = \operatorname{tr}(\boldsymbol{P}_n \boldsymbol{V}) + \boldsymbol{p}_n^{\mathrm{T}} \boldsymbol{f} + \varepsilon \operatorname{tr}(\boldsymbol{P}_n) = \boldsymbol{e}_1^{\mathrm{T}} \sum_{j \in \hat{\mathcal{B}}_{\mathcal{I}}(n)} \boldsymbol{s}_j + \varepsilon \operatorname{tr}(\boldsymbol{P}_n)$$
$$\operatorname{tr}(\boldsymbol{Q}_n \bar{\boldsymbol{V}}) + \boldsymbol{q}_n^{\mathrm{T}} \boldsymbol{f} = \operatorname{tr}(\boldsymbol{Q}_n \boldsymbol{V}) + \boldsymbol{q}_n^{\mathrm{T}} \boldsymbol{f} + \varepsilon \operatorname{tr}(\boldsymbol{Q}_n) = \boldsymbol{e}_2^{\mathrm{T}} \sum_{j \in \hat{\mathcal{B}}_{\mathcal{I}}(n)} \boldsymbol{s}_j + \varepsilon \operatorname{tr}(\boldsymbol{Q}_n)$$

for all $n \in \mathcal{V}$ and

$$\operatorname{tr}(\boldsymbol{C}_m \bar{\boldsymbol{V}}) + \boldsymbol{c}_m^{\mathrm{T}} \boldsymbol{f} = \operatorname{tr}(\boldsymbol{C}_m \boldsymbol{V}) + \boldsymbol{c}_m^{\mathrm{T}} \boldsymbol{f} + \varepsilon \operatorname{tr}(\boldsymbol{C}_m) \begin{cases} < b_m + \varepsilon \operatorname{tr}(\boldsymbol{C}_m) & \text{if } \boldsymbol{C}_m \neq \boldsymbol{0} \\ \leq b_m & \text{otherwise} \end{cases}$$

for all $m \in \mathcal{M}$. For ε sufficiently small, there exist $\bar{\boldsymbol{s}}_{\mathcal{I}} \in \mathcal{S}_{\mathcal{I}}$ such that

$$\sum_{j \in \hat{\mathcal{B}}_{\mathcal{I}}(n)} \bar{\boldsymbol{s}}_j \;\; = \sum_{j \in \hat{\mathcal{B}}_{\mathcal{I}}(n)} \boldsymbol{s}_j + \varepsilon \begin{bmatrix} \operatorname{tr}(\boldsymbol{P}_n) \\ \operatorname{tr}(\boldsymbol{Q}_n) \end{bmatrix}$$

for all $n \in \mathcal{V}$, considering that $\operatorname{tr}(\boldsymbol{Q}_n) = 0$ for $n \in \bar{\mathcal{V}}$ due to (2.70), (2.26), (2.24), and (2.17) in conjunction with Definition 5 and Definition 7. Hence, there exists some $\varepsilon > 0$ such that $(\bar{\boldsymbol{V}}, \boldsymbol{f}, \bar{\boldsymbol{s}}_{\mathcal{I}})$ is feasible in (3.14) with $\bar{\boldsymbol{V}} \succ \boldsymbol{0}$. □

4.2.2 Second-Order Cone Relaxation

Again, the *Lagrangian dual problem* is considered to study the relation to LMPs, here for the SOCR (3.18). The matrix inequalities (3.18c) are dualized with $\boldsymbol{\Lambda}_k \in \mathbb{S}^2_+$, where $k \in \mathcal{E}$, while (3.10b), (3.10c), and (3.10d) are dualized with $\boldsymbol{\lambda}_{\mathcal{V}} \in \mathbb{R}^2_{\mathcal{V}}$ and $\boldsymbol{\mu} \in \mathbb{R}^{|\mathcal{M}|}_+$. The *Lagrangian function* $\tilde{\mathscr{L}} : \tilde{\mathbb{S}}^{|\mathcal{V}|} \times \mathbb{R}^{4|\mathcal{C}|} \times \mathcal{S}_{\mathcal{I}} \times \mathbb{S}^2_{+,\mathcal{E}} \times \mathbb{R}^2_{\mathcal{V}} \times \mathbb{R}^{|\mathcal{M}|}_+ \to \mathbb{R}$ is then

$$\begin{aligned} \tilde{\mathscr{L}}(\boldsymbol{V}, \boldsymbol{f}, \boldsymbol{s}_{\mathcal{I}}, \boldsymbol{\Lambda}_{\mathcal{E}}, \boldsymbol{\lambda}_{\mathcal{V}}, \boldsymbol{\mu}) = \sum_{j \in \mathcal{I}} C_j(\boldsymbol{s}_j) + \tau(\operatorname{tr}(\boldsymbol{L}\boldsymbol{V}) + \boldsymbol{l}^{\mathrm{T}} \boldsymbol{f}) - \sum_{k \in \mathcal{E}} \operatorname{tr}(\boldsymbol{\Lambda}_k \boldsymbol{S}_k^{\mathrm{T}} \boldsymbol{V} \boldsymbol{S}_k) \\ + \sum_{n \in \mathcal{V}} [\boldsymbol{\lambda}_n]_1 \Big[\operatorname{tr}(\boldsymbol{P}_n \boldsymbol{V}) + \boldsymbol{p}_n^{\mathrm{T}} \boldsymbol{f} - \boldsymbol{e}_1^{\mathrm{T}} \sum_{j \in \hat{\mathcal{B}}_{\mathcal{I}}(n)} \boldsymbol{s}_j \Big] \\ + \sum_{n \in \mathcal{V}} [\boldsymbol{\lambda}_n]_2 \Big[\operatorname{tr}(\boldsymbol{Q}_n \boldsymbol{V}) + \boldsymbol{q}_n^{\mathrm{T}} \boldsymbol{f} - \boldsymbol{e}_2^{\mathrm{T}} \sum_{j \in \hat{\mathcal{B}}_{\mathcal{I}}(n)} \boldsymbol{s}_j \Big] \\ + \sum_{m \in \mathcal{M}} [\boldsymbol{\mu}]_m \Big[\operatorname{tr}(\boldsymbol{C}_m \boldsymbol{V}) + \boldsymbol{c}_m^{\mathrm{T}} \boldsymbol{f} - b_m \Big] \end{aligned}$$

$$= \sum_{j\in\mathcal{I}} \Big(C_j(\boldsymbol{s}_j) - \boldsymbol{\lambda}_{\hat{n}(j)}^{\mathrm{T}} \boldsymbol{s}_j \Big) - \boldsymbol{\mu}^{\mathrm{T}} \boldsymbol{b} + \psi(\boldsymbol{\lambda}_{\mathcal{V}}, \boldsymbol{\mu})^{\mathrm{T}} \boldsymbol{f} + \operatorname{tr}\left(\left[\Psi(\boldsymbol{\lambda}_{\mathcal{V}}, \boldsymbol{\mu}) - \sum_{k\in\mathcal{E}} \boldsymbol{S}_k \boldsymbol{\Lambda}_k \boldsymbol{S}_k^{\mathrm{T}} \right] \boldsymbol{V} \right) \tag{4.12}$$

As before, the definition of $\boldsymbol{L}$ and $\boldsymbol{l}$ in (2.46) and (2.47) is utilized and Ψ and ψ read as in (4.3). The corresponding *Lagrangian dual function* $\tilde{\theta} : \mathbb{S}^2_{+,\mathcal{E}} \times \mathbb{R}^2_{\mathcal{V}} \times \mathbb{R}_+^{|\mathcal{M}|} \to \mathbb{R}$ is

$$\begin{aligned} &\tilde{\theta}(\boldsymbol{\Lambda}_{\mathcal{E}}, \boldsymbol{\lambda}_{\mathcal{V}}, \boldsymbol{\mu}) \\ &\quad = \inf_{\substack{\boldsymbol{s}_j \in \mathcal{S}_j \\ \boldsymbol{V} \in \tilde{\mathbb{S}}^{|\mathcal{V}|} \\ \boldsymbol{f} \in \mathbb{R}^{4|\mathcal{C}|}}} \tilde{\mathscr{L}}(\boldsymbol{V}, \boldsymbol{f}, \boldsymbol{s}_{\mathcal{I}}, \boldsymbol{\Lambda}_{\mathcal{E}}, \boldsymbol{\lambda}_{\mathcal{V}}, \boldsymbol{\mu}) \\ &\quad = \begin{cases} -\sum_{j\in\mathcal{I}} \pi_j(\boldsymbol{\lambda}_{\hat{n}(j)}) - \boldsymbol{\mu}^{\mathrm{T}} \boldsymbol{b} & \text{if } \Psi(\boldsymbol{\lambda}_{\mathcal{V}}, \boldsymbol{\mu}) = \sum_{k\in\mathcal{E}} \boldsymbol{S}_k \boldsymbol{\Lambda}_k \boldsymbol{S}_k^{\mathrm{T}} \ \wedge \ \psi(\boldsymbol{\lambda}_{\mathcal{V}}, \boldsymbol{\mu}) = \boldsymbol{0} \\ -\infty & \text{otherwise} \end{cases} \end{aligned} \tag{4.13}$$

with π_j in (4.5). The *Lagrangian dual problem* of the SOCR (3.18) can thus be stated as

$$\tilde{d}^{\star} = - \underset{\substack{\boldsymbol{\lambda}_n \in \mathbb{R}^2, \, \boldsymbol{\mu} \in \mathbb{R}_+^{|\mathcal{M}|} \\ \boldsymbol{\Lambda}_k \in \mathbb{S}^2}}{\text{minimize}} \quad \sum_{j\in\mathcal{I}} \pi_j(\boldsymbol{\lambda}_{\hat{n}(j)}) + \boldsymbol{\mu}^{\mathrm{T}} \boldsymbol{b} \tag{4.14a}$$

$$\text{subject to} \quad \Psi(\boldsymbol{\lambda}_{\mathcal{V}}, \boldsymbol{\mu}) = \sum_{k\in\mathcal{E}} \boldsymbol{S}_k \boldsymbol{\Lambda}_k \boldsymbol{S}_k^{\mathrm{T}} \tag{4.14b}$$

$$\psi(\boldsymbol{\lambda}_{\mathcal{V}}, \boldsymbol{\mu}) = \boldsymbol{0} \tag{4.14c}$$

$$\boldsymbol{\Lambda}_k \succeq \boldsymbol{0}, \quad k \in \mathcal{E}\,. \tag{4.14d}$$

It can be observed that the equivalence to the Lagrangian dual (4.6) of the OPF problem as observed for the SDR is invalidated for the SOCR. The constraint $\Psi(\boldsymbol{\lambda}_{\mathcal{V}}, \boldsymbol{\mu}) \succeq \boldsymbol{0}$ in (4.6b) is superseded by (4.14b) and (4.14d), where the right-hand side in (4.14b) describes a class of psd matrices that is parameterized by $\boldsymbol{\Lambda}_{\mathcal{E}}$. Therefore, the OPF dual (4.6) is a relaxation of the SOCR dual (4.14) as shown by the following result.

Lemma 2. *Let* $(\boldsymbol{\Lambda}_{\mathcal{E}}, \boldsymbol{\lambda}_{\mathcal{V}}, \boldsymbol{\mu})$ *be feasible in* (4.14)*. Then,* $(\boldsymbol{\lambda}_{\mathcal{V}}, \boldsymbol{\mu})$ *is feasible in* (4.6)*.*

Proof. From (4.14d) it follows that $\boldsymbol{S}_k \boldsymbol{\Lambda}_k \boldsymbol{S}_k^{\mathrm{T}} \succeq \boldsymbol{0}$. As a sum of psd matrices is psd, (4.14b) implies $\Psi(\boldsymbol{\lambda}_{\mathcal{V}}, \boldsymbol{\mu}) \succeq \boldsymbol{0}$. □

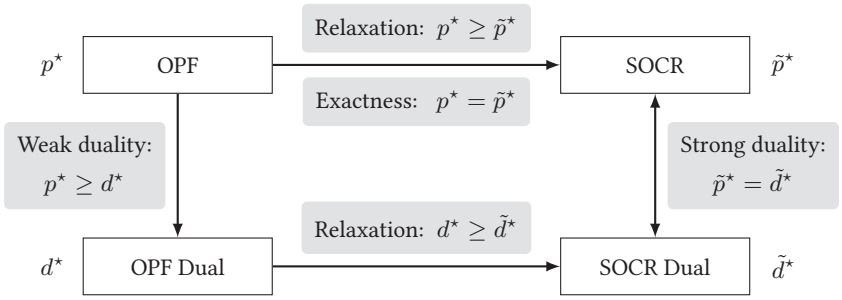

Figure 4.2: Relation of the OPF problem (3.12), the SOCR (3.18), as well as their Lagrangian dual problems in (4.6) and (4.14), respectively.

Corollary 4. *For the OPF dual* (4.6) *and the SOCR dual* (4.14)*, it holds that* $d^\star \geq \tilde{d}^\star$.

This result, along with Corollary 3, weak duality in the nonconvex OPF problem (3.12), and strong duality in the convex SOCR (3.18), is shown in Figure 4.2 and reveals the following relation of the *duality gap* of the OPF problem and *exactness* of the SOCR.

Theorem 2. *If the SOCR* (3.18) *is exact and obtains strong duality, then the OPF problem* (3.12) *obtains strong duality, i.e.,* $p^\star = d^\star$.

Proof. By Corollary 3, exactness of the SOCR implies $p^\star = \tilde{p}^\star$ and strong duality in the SOCR states $\tilde{p}^\star = \tilde{d}^\star$. Furthermore, Corollary 4 yields $d^\star \geq \tilde{d}^\star$ and *weak duality* [43, Ch. 6.2] in the OPF problem implies $p^\star \geq d^\star$. Therefore,

$$p^\star = \tilde{p}^\star = \tilde{d}^\star \leq d^\star \quad \wedge \quad p^\star \geq d^\star \qquad \Longrightarrow \qquad p^\star = d^\star. \qquad \square$$

Therefore, even though the Lagrangian dual of the SOCR does *not* match the Lagrangian dual of the OPF problem as in case of the SDR, exactness and strong duality in the SOCR still implies a zero duality gap in the OPF problem. Consequently, it certifies the optimal dual variables $\boldsymbol{\lambda}_{\mathcal{V}}^\star$ in the OPF dual (4.6) as LMPs. Yet, in the SDR certifying and determining the dual variables as LMPs is accomplished *jointly* by solving the SDR (3.14) and its dual (4.6) with a primal-dual interior-point method. This raises the question whether the dual variables in the SOCR dual (4.14) match the dual variables in the OPF dual (4.6) under exactness. To this end, consider the following result.

Theorem 3. *Let* $(\boldsymbol{V}^\star, \boldsymbol{f}^\star, \boldsymbol{s}_{\mathcal{I}}^\star, \boldsymbol{\Lambda}_{\mathcal{E}}^\star, \boldsymbol{\lambda}_{\mathcal{V}}^\star, \boldsymbol{\mu}^\star)$ *be a primal and dual optimal solution of the SOCR, i.e., of* (3.18) *and* (4.14)*, which obtains strong duality and where* $\boldsymbol{V}^\star$ *permits a psd rank-1 completion. Then,* $(\boldsymbol{v}^\star, \boldsymbol{f}^\star, \boldsymbol{s}_{\mathcal{I}}^\star, \boldsymbol{\lambda}_{\mathcal{V}}^\star, \boldsymbol{\mu}^\star)$*, where* $\boldsymbol{v}^\star(\boldsymbol{v}^\star)^{\mathrm{H}}$ *is a psd*

rank-1 completion of $\boldsymbol{V}^\star$, is a primal and dual optimal solution of the OPF problem, i.e., of (3.12) *and* (4.6)*.*

Proof. By construction of the SOCR (3.18), $(\boldsymbol{v}^\star, \boldsymbol{f}^\star, \boldsymbol{s}_\mathcal{I}^\star)$ is optimal in the OPF problem (3.12) and $p^\star = \tilde{p}^\star$. Jointly with Theorem 2 and strong duality in the SOCR, this implies that $d^\star = \tilde{d}^\star$. Lemma 2 states that $(\boldsymbol{\lambda}_\mathcal{V}^\star, \boldsymbol{\mu}^\star)$ is feasible in the OPF dual (4.6) and, by the equivalence of the objective functions, attains $\tilde{d}^\star = d^\star$ and is thus optimal in (4.6). □

Consequently, if the SOCR is *exact* and *strong duality* obtains, it follows that the OPF problem (3.12) exhibits a *zero duality gap* and the optimal dual variables $\boldsymbol{\lambda}_\mathcal{V}^\star$ of the SOCR dual (4.14) constitute the LMPs. Thus, analogous to the SDR, certifying and determining the dual variables as LMPs is accomplished *jointly* by solving the SOCR (3.18) and its dual (4.14) with a primal-dual interior-point method, with the additional computational advantages discussed in Section 3.2.2.

As the SOCR (3.18) is a convex problem, strong duality usually obtains and the above relation essentially hinges on the exactness of the relaxation. To show that strong duality is ensured *a priori* under some reasonable conditions, suppose that the OPF problem (3.12) is essentially strictly feasible as established in Assumption 1.

Proposition 3. *Under Assumption 1, strong duality is guaranteed in the SOCR* (3.18)*.*

Proof. In (3.18), all constraints are affine in the optimization variables and, hence, Slater's constraint qualification holds if there exists a feasible point $(\boldsymbol{V}, \boldsymbol{f}, \boldsymbol{s}_\mathcal{I})$ in (3.18) for which (3.18c) holds strictly. By the proof of Proposition 2, it follows that under Assumption 1 there exists a point $(\boldsymbol{V}, \boldsymbol{f}, \boldsymbol{s}_\mathcal{I}) \in \mathcal{X}$ with $\boldsymbol{s}_\mathcal{I} \in \mathcal{S}_\mathcal{I}$ for which $\boldsymbol{V} \succ \boldsymbol{0}$. As all principal submatrices of a positive definite matrix are positive definite [92, Ch. 7.1], it follows with Corollary 1 that $(\bar{\boldsymbol{V}}, \boldsymbol{f}, \boldsymbol{s}_\mathcal{I})$ with $\bar{\boldsymbol{V}} = \mathscr{P}(\boldsymbol{V})$ is feasible in (3.18) and that $\boldsymbol{S}_k^\mathrm{T} \bar{\boldsymbol{V}} \boldsymbol{S}_k \succ \boldsymbol{0}$, for all $k \in \mathcal{E}$. □

5 The Hybrid Architecture

The preceding chapters discuss two fundamentally important problems in power systems, i.e., the *optimal power flow* and *locational marginal pricing*, and make evident that the inherent difficulty of solving these problems arises from the nonconvexity of the OPF problem, which is inevitably induced by the system's physical laws. By augmenting the OPF problem with *non-physical states*, it can be *relaxed* from a nonconvex to a convex optimization problem, which facilitates the computation of both the OPF and LMPs with polynomial-time algorithms and enables the utilization of the powerful theory of convex analysis. However, by the nature of the relaxation, the solution obtained from a convex relaxation of the OPF problem is only reasonable if it corresponds to a *physically valid state* of the system, i.e., if it can be mapped to a point in the feasible set of the OPF problem, in which case the relaxation is called *exact*, see Section 3.2. While regularization or feasibility recovery may be employed to obtain a (generally suboptimal) physically valid state in case of inexactness (see e.g. [34, 63, 114–116]), an actual *shift* of the OPF problem into the *convex domain* is only attained under *exactness* of a relaxation.[15] In that sense, *exactness* classifies power systems into those that can be solved in the convex domain and those that, at the current state of science, remain in the nonconvex domain. From this perspective, it is interesting to mathematically identify and characterize power systems that exhibit an inherent tendency toward exactness of a relaxation. In the literature, several results were reported for AC grids [51, 52, 60–64] and DC grids [61, 65, 66]. For radial AC grids [52, 60–62, 64] and meshed AC grids with cycles limited to three branches [63], exactness has been proven under certain technical conditions, e.g., the omission of power injection lower bounds ("load oversatisfaction"). However, in case of the most relevant and challenging application for OPF and LMP computations, i.e., on the *transmission level* of a power system, the network topology is essentially always widely *meshed* for reasons of reliability

[15] Exactness may be supported by tightening or adding valid inequalities, see e.g. [117] and the references therein. For the results on exactness presented later in this work, this is *not* required.

and capacity. Thus, for those systems that may benefit the most from a shift of the OPF problem into the convex domain, guarantees of exactness have not yet been established and, as indicated by computational studies [3, 95, 114], it may also not be possible to do so for general meshed systems.

Historically, most large-scale power systems evolved from the interconnection of utility systems [118] and in 1962, when Carpentier [16, 17] first formulated the OPF problem to identify the economically optimal operation of a power system, such historically grown large-scale systems were already in place. From today's perspective, knowing that power systems span continents and that economic operation is a fundamental requirement, it may be asked whether the system could be designed differently in order to support or simplify its economically optimal operation. This question motivated us to study the exactness of convex relaxations of the OPF problem on the *transmission level*: Can we find a power system design with a *meshed* network topology that facilitates the shift of the OPF problem into the convex domain?

One such approach, and to the best of our knowledge the only one besides our work, was proposed by Farivar and Low in [73]: Motivated by the solution recovery condition for a relaxation of the OPF problem for AC grids based on the branch flow model, which requires that the voltage angle differences along every loop of branches sum up to zero (or a multiple of 2π), they propose the installation of *phase shifters* in every branch outside some arbitrary spanning tree of the system's network topology. These phase shifters may be interpreted as providing the "slack" to satisfy the recovery condition and, therewith, enable the mapping of the solution of the relaxation to a physically valid state. However, as the slack phase shifts are an unregulated consequence of the relaxation, they may be large, stability-endangering, or even intractable. Therefore, while this is a very stimulating and mathematically interesting result, such a redesign of a power system is potentially not attractive from an engineering perspective. With this dilemma in mind that conditions arising from a direct mathematical study of exactness are potentially not reasonable from an engineering point of view, we tried to approach this challenge from another angle: Can we identify grid upgrade measures that are motivated from an engineering perspective and which have the potential to transform the structure of the OPF problem?

This research question led us to HVDC systems and, as a consequence, to the study of hybrid AC/DC power systems. To counteract the climate change, many countries consider a decarbonization of the energy sector, especially via a transition of electricity generation based on fossil fuels toward RES [13, 67]. This transition

introduces an increasingly distributed and fluctuating energy production, which generally necessitates additional transmission capacity as well as stronger interconnections of regional and national grids to balance and smooth the variability of RES-based generation [13, 15]. However, the implementation of new transmission corridors is, on one hand, often difficult and time consuming, most notably due to the obtainment of right of way, and, on the other hand, it can cause substantial public opposition, e.g., concerning the impact on humans, landscape, and real estate value [68–71]. As a consequence, *transmission system operators* (TSOs) and regulators can be willing to accept extensive additional costs to avoid or mitigate issues related to new corridors. This is exemplified by the preference of DC *cables* in the network development plan of Germany ("Erdkabelvorrang" as per § 3 Bundesbedarfsplangesetz) to foster public acceptance, which causes additional costs of several billion Euros [119, 120]. One approach to improve the utilization of *existing* transmission corridors is the conversion of AC lines to DC operation, which can enable a major increase in corridor transmission capacity [121, 122]. Additionally, VSC-based HVDC systems offer a rapid and independent control of active and reactive power, which further enables the provision of ancillary services to the system [12]. Thus, even though HVDC technology is still rather expensive [123], there can be strong driving forces to consider the conversion of AC lines to DC operation. Motivated by this observation, we started to study the exactness of convex relaxations of the OPF problem for *hybrid AC/DC power systems* considering the impact of such conversions.

Our approach to identify hybrid AC/DC power systems with a strong tendency toward exactness was inspired by a remarkable observation of Bose, Gayme, Low, and Chandy [124, 125] in the context of the SDR of the OPF problem for AC grids: They established a connection between the *exactness* of the relaxation (optimizer with rank 1) and the *network topology* of the system via the *complementary slackness* at optimality. The complementary slackness specifies that the inner product of two psd matrices, i.e., an optimizer and a weighted sum of the coefficient matrices, vanishes, which implies orthogonality of their ranges. On this basis, using the result of van der Holst [126, Th. 3.4] (see also [127, 128]) that a psd matrix with an associated tree graph has nullity at most one and considering that, under certain conditions, the weighted sum of the coefficient matrices inherits the graph of the system's network topology, they show that exactness is guaranteed for *radial* power systems under some technical conditions. For our objective of identifying hybrid AC/DC grids with a strong tendency toward exactness, an important conclusion from this result is that the *sparsity pattern* of the *coefficient matrices*, which is defined by the system's *network topology*, may be utilized to manipulate the optimizers of the relaxation

toward exactness. Furthermore, it can observed that the controllability of converters "decouples" the AC- and DC-side voltage, which is reflected in the structure of the coefficient matrices. This is illustrated by Corollary 1 in Section 2.4.1, which shows that the sparsity pattern solely depends on the system's *branches* and is independent of its converters. Based on this key insight, we developed and analyzed a hybrid AC/DC system structure in the series of work in [1–3] that exhibits both a meshed network topology and a strong tendency toward exactness. This system structure, which we refer to as the *hybrid architecture*, is defined as follows.

Definition 13 (Hybrid Architecture)**.** The underlying undirected graph of the directed subgraph $\mathcal{G}' = \{\mathcal{V}, \mathcal{E}, \hat{\epsilon}, \check{\epsilon}\}$ is *acyclic*, i.e., its connected components are *trees*.

With the *hybrid architecture*, any *arbitrary* meshed network topology can be formed by an interconnection of radial AC and DC subgrids. In an existing AC transmission grid such a structural transformation may be attained, for example, by the conversion of AC branches outside some arbitrary spanning tree, i.e., every loop within the transmission grid is resolved by a conversion measure. In the following, Section 5.1 presents the proof of the strong tendency toward exactness under the *hybrid architecture*, which extends our work in [2] to the more general system model and OPF formulation in Chapter 2 and Chapter 3. Subsequently, Section 5.2 is devoted to an engineering interpretation of this result as well as the deduction of implications on the design and expansion of power systems.

5.1 Exactness of the Relaxations under the Hybrid Architecture

This section develops a series of results to show that the convex relaxations of the OPF problem presented in this work exhibit a strong tendency toward exactness under the *hybrid architecture*. In preparation for this characterization of exactness, the discussion is first turned toward the identification of physical properties of the power system in Section 5.1.1 and the introduction of some preliminaries in Section 5.1.2. The latter are primarily concerned with the derivation of certain properties of the coefficient matrices, specifically the relation of their off-diagonal elements to cones and half-spaces in the complex plane due to the physical properties of the system. On this basis, Section 5.1.3 develops an interpretable characterization of exactness by relating a sufficient condition for exactness of the OPF problem to properties of LMPs. The concluding discussion of these results elucidates as to why the relaxations are typically exact under the *hybrid architecture*.

5.1.1 Physical Properties and Assumptions

The study hereafter utilizes the following assumptions. Assumption 2 to 7 generally holds, while Assumption 8 can typically be established by representing (balanced) parallel branches by an equivalent single branch. Note that Assumption 8 is only considered to simplify the exposition and the results can be generalized to parallel branches. Some systems, e.g., with series-overcompensated or unbalanced parallel lines, may require (local) approximations to comply with these model assumptions.

Assumption 2 (Passive Branches)**.** All branches are passive, i.e.,

$$\forall k \in \mathcal{E}: \quad \mathrm{Re}(\bar{y}_k) \geq 0, \quad \mathrm{Re}(\hat{y}_k) \geq 0, \quad \mathrm{Re}(\check{y}_k) \geq 0\,. \tag{5.1}$$

Assumption 3 (Lossy Branches)**.** All branches are lossy, i.e.,

$$\forall k \in \mathcal{E}: \quad \mathrm{Re}(\bar{y}_k) > 0\,. \tag{5.2}$$

Assumption 4 (Inductive Branches)**.** All branches are inductive, i.e.,

$$\forall k \in \mathcal{E}: \quad \mathrm{Im}(\bar{y}_k) \leq 0\,. \tag{5.3}$$

Assumption 5 (Properly Insulated Branches)**.** All branches are well insulated, i.e.,

$$\forall k \in \mathcal{E}: \quad \frac{|\hat{y}_k|}{|\bar{y}_k|} \leq 1 \quad \text{and} \quad \frac{|\check{y}_k|}{|\bar{y}_k|} \leq 1\,. \tag{5.4}$$

Assumption 6 (Proper Phase Shifts)**.** All branches exhibit a total phase shift of less than or equal to 90 degrees, i.e.,

$$\forall k \in \mathcal{E}: \quad |\arg(\rho_k)| \leq \frac{\pi}{2}\,. \tag{5.5}$$

Assumption 7 (Proper Angle Limits)**.** The angle difference limits satisfy

$$\forall k \in \mathcal{E}: \quad -\frac{\pi}{2} < \underline{\delta}_k \leq -\arg(\rho_k) \quad \text{and} \quad -\arg(\rho_k) \leq \bar{\delta}_k < \frac{\pi}{2}\,. \tag{5.6}$$

Assumption 8 (Unique Branches)**.** The multigraph $\mathcal{G}$ does not comprise any parallel or antiparallel branches, i.e.,

$$\text{1)} \quad \nexists\, k_1, k_2 \in \mathcal{E}, k_1 \neq k_2: \ \hat{\epsilon}(k_1) = \hat{\epsilon}(k_2) \ \wedge \ \check{\epsilon}(k_1) = \check{\epsilon}(k_2) \tag{5.7a}$$

$$\text{2)} \quad \nexists\, k_1, k_2 \in \mathcal{E}, k_1 \neq k_2: \ \hat{\epsilon}(k_1) = \check{\epsilon}(k_2) \ \wedge \ \check{\epsilon}(k_1) = \hat{\epsilon}(k_2)\,. \tag{5.7b}$$

5.1.2 Preliminaries

In the following, the notion of cones and half-spaces in the complex plane is introduced to subsequently establish some properties of the coefficient matrices. Prior to that, for the sake of completeness the known[16] result in Lemma 3 is documented here for later reference.

Lemma 3. *Let* $\boldsymbol{A}, \boldsymbol{B} \in \mathbb{S}_+^N$. *Then,* $\operatorname{tr}(\boldsymbol{AB}) = 0$ *implies* $\operatorname{rank}(\boldsymbol{A}) + \operatorname{rank}(\boldsymbol{B}) \leq N$.

Proof. Let $\boldsymbol{A} = \boldsymbol{Q}\boldsymbol{\Sigma}\boldsymbol{Q}^{\mathrm{H}}$ and $\boldsymbol{B} = \boldsymbol{U}\boldsymbol{\Lambda}\boldsymbol{U}^{\mathrm{H}}$ be the *eigenvalue decompositions* (EVDs) of the psd matrices $\boldsymbol{A}$ and $\boldsymbol{B}$, i.e., $\boldsymbol{\Sigma} = \operatorname{diag}(\sigma_1, \ldots, \sigma_N)$ and $\boldsymbol{\Lambda} = \operatorname{diag}(\lambda_1, \ldots, \lambda_N)$ comprise the *nonnegative* eigenvalues and the unitary matrices $\boldsymbol{Q} = [\boldsymbol{q}_1, \ldots, \boldsymbol{q}_N]$ and $\boldsymbol{U} = [\boldsymbol{u}_1, \ldots, \boldsymbol{u}_N]$ comprise the eigenvectors of $\boldsymbol{A}$ and $\boldsymbol{B}$. It follows that

$$\operatorname{tr}(\boldsymbol{AB}) = \sum_{i=1}^{N} \sum_{j=1}^{N} \sigma_i \lambda_j \left| \boldsymbol{q}_i^{\mathrm{H}} \boldsymbol{u}_j \right|^2 \geq 0 \,. \tag{5.8}$$

This holds with equality if and only if $\sigma_i \lambda_j \left| \boldsymbol{q}_i^{\mathrm{H}} \boldsymbol{u}_j \right|^2 = 0$, $\forall i, j$. For $\sigma_i = 0$ and/or $\lambda_j = 0$ the respective summand is trivially zero. For $\sigma_i > 0$ and $\lambda_j > 0$ the summand is zero if and only if $\boldsymbol{q}_i^{\mathrm{H}} \boldsymbol{u}_j = 0$. As the range of a Hermitian matrix is the space spanned by the eigenvectors corresponding to nonzero eigenvalues, it follows that $\operatorname{tr}(\boldsymbol{AB}) = 0$ if and only if $\operatorname{range}(\boldsymbol{A})$ and $\operatorname{range}(\boldsymbol{B})$ are *orthogonal*, i.e., $\boldsymbol{q}^{\mathrm{H}} \boldsymbol{u} = 0$, $\forall \boldsymbol{q} \in \operatorname{range}(\boldsymbol{A})$ and $\forall \boldsymbol{u} \in \operatorname{range}(\boldsymbol{B})$. As for Hermitian matrices the nullspace is the orthogonal complement of the range, it follows that

$$\operatorname{range}(\boldsymbol{A}) \subseteq \operatorname{null}(\boldsymbol{B}) \quad \text{and} \quad \operatorname{range}(\boldsymbol{B}) \subseteq \operatorname{null}(\boldsymbol{A}) \,. \tag{5.9}$$

For a subspace $\mathcal{Z} \subseteq \mathcal{W}$ of a linear space $\mathcal{W}$, their dimensions satisfy $\dim(\mathcal{Z}) \leq \dim(\mathcal{W})$. Further, for a Hermitian matrix $\boldsymbol{X} \in \mathbb{S}^N$, $\dim(\operatorname{range}(\boldsymbol{X})) = \operatorname{rank}(\boldsymbol{X})$ and $\dim(\operatorname{null}(\boldsymbol{X})) = N - \operatorname{rank}(\boldsymbol{X})$. Thus, (5.9) implies $\operatorname{rank}(\boldsymbol{A}) + \operatorname{rank}(\boldsymbol{B}) \leq N$. □

5.1.2.1 Cones and Half-Spaces in the Complex Plane

Definition 14. The *conic hull* $\operatorname{cone}(\mathcal{S}) \subseteq \mathbb{C}$ of a countable set $\mathcal{S} \subset \mathbb{C}$ is

$$\operatorname{cone}(\mathcal{S}) = \left\{ x \in \mathbb{C} : x = \sum_{i=1}^{j} \alpha_i x_i, \; x_i \in \mathcal{S}, \; \alpha_i \in \mathbb{R}_+, \; i, j \in \{1, \ldots, |\mathcal{S}|\} \right\}. \tag{5.10}$$

[16] For example, Bose *et al.* [124] derives a variant of Lemma 3 in the proof of [124, Th. 3.1].

Corollary 5. *For a countable set $\mathcal{S} \subset \mathbb{C}$ with $\mathcal{S} \neq \{0\}$,*

$$\operatorname{cone}(\mathcal{S}) = \operatorname{cone}(\{\exp(\mathbf{i} \arg(x))\}_{x \in \mathcal{S}:|x|>0}) \,. \tag{5.11}$$

Definition 15. The set $\mathcal{S} \subset \mathbb{C}$ is a *half-space* with *normal* $p \in \mathbb{C} \setminus \{0\}$ if[17]

$$\mathcal{S} = \{x \in \mathbb{C} : \operatorname{Re}(p^* x) \leq 0\} \,. \tag{5.12}$$

Proposition 4. *The interior $\operatorname{int}(\mathcal{S})$ of a half-space $\mathcal{S} \subset \mathbb{C}$ with normal $p \in \mathbb{C} \setminus \{0\}$ is*

$$\operatorname{int}(\mathcal{S}) = \{x \in \mathbb{C} : \operatorname{Re}(p^* x) < 0\} \,. \tag{5.13}$$

Proof. Let $\mathcal{U}_\varepsilon(x) = \{\bar{x} \in \mathbb{C} : |\bar{x} - x| \leq \varepsilon\}$ be the ε-neighborhood of $x \in \mathbb{C}$. Consider a point $x \in \mathcal{S}$ and $\bar{x} = x + \varepsilon p/|p| \in \mathcal{U}_\varepsilon(x)$. It follows immediately that if and only if $\operatorname{Re}(p^* x) < 0$ there exists some $\varepsilon > 0$ such that $\mathcal{U}_\varepsilon(x) \subseteq \mathcal{S}$. □

Corollary 6. *If $\mathcal{S} \subset \mathbb{C}$ is a half-space, then $0 \notin \operatorname{int}(\mathcal{S})$.*

Corollary 7. *If $\mathcal{S} \subset \mathbb{C}$ is a half-space and $x \in \operatorname{int}(\mathcal{S})$, then $\alpha x \in \operatorname{int}(\mathcal{S})$ for $\alpha > 0$.*

Proposition 5. *Let $\mathcal{S} \subset \mathbb{C}$ be a half-space, $x_1 \in \mathcal{S}$, $x_2 \in \operatorname{int}(\mathcal{S})$, and $\bar{x} = x_1 + x_2$. Then, $\bar{x} \in \operatorname{int}(\mathcal{S})$.*

Proof. Let $p \in \mathbb{C} \setminus \{0\}$ be a normal of $\mathcal{S}$. Then, by definition, $\operatorname{Re}(p^* x_1) \leq 0$ and $\operatorname{Re}(p^* x_2) < 0$. Therefore, $\operatorname{Re}(p^* \bar{x}) = \operatorname{Re}(p^* x_1) + \operatorname{Re}(p^* x_2) < 0$. □

5.1.2.2 Properties of the Coefficient Matrices

Lemma 4. *Consider the set $\mathcal{K}$ of coefficient matrices in* (2.73) *and, for $k \in \mathcal{E}$, let*

$$\mathcal{K}_k = \left\{0, -1, \frac{\hat{\beta}_k}{2}, \frac{\check{\beta}_k^*}{2}, -\frac{\hat{\beta}_k}{2\mathbf{i}}, \frac{\check{\beta}_k^*}{2\mathbf{i}}, \hat{\alpha}_k^* \hat{\beta}_k, \check{\alpha}_k \check{\beta}_k^*, \tan(\underline{\delta}_k) + \mathbf{i}, -\tan(\bar{\delta}_k) - \mathbf{i}\right\} \subset \mathbb{C}. \tag{5.14}$$

Under Assumption 8, for all $k \in \mathcal{E}$,

$$[\boldsymbol{X}]_{\hat{\epsilon}(k),\check{\epsilon}(k)} \in \mathcal{K}_k \,, \qquad \forall \boldsymbol{X} \in \mathcal{K} \,. \tag{5.15}$$

[17] Note that an inner product $\langle \cdot, \cdot \rangle : \mathbb{C} \times \mathbb{C} \to \mathbb{R}$ of the complex plane over $\mathbb{R}$ is employed, which follows from $\langle a, b \rangle = \operatorname{Re}(b^* a) = [\operatorname{Re}(b), \operatorname{Im}(b)]^{\mathrm{T}} [\operatorname{Re}(a), \operatorname{Im}(a)]$. For simplicity, it is kept explicit.

Proof. Consider any $k \in \mathcal{E}$ and let $i = \hat{\epsilon}(k)$ and $j = \check{\epsilon}(k)$, where $i \neq j$ by the self-loop free network graph in Definition 4. It follows from (2.69) that

$$[\boldsymbol{P}_i]_{i,j} = [\boldsymbol{Y}]_{i,j}/2 \tag{5.16}$$
$$[\boldsymbol{P}_j]_{i,j} = [\boldsymbol{Y}]^*_{j,i}/2 \tag{5.17}$$
$$[\boldsymbol{P}_n]_{i,j} = 0\,, \qquad \forall n \in \mathcal{V} \setminus \{i,j\} \tag{5.18}$$

and, analogously, from (2.70) that

$$[\boldsymbol{Q}_i]_{i,j} = -[\boldsymbol{Y}]_{i,j}/(2\mathbf{i}) \tag{5.19}$$
$$[\boldsymbol{Q}_j]_{i,j} = [\boldsymbol{Y}]^*_{j,i}/(2\mathbf{i}) \tag{5.20}$$
$$[\boldsymbol{Q}_n]_{i,j} = 0\,, \qquad \forall n \in \mathcal{V} \setminus \{i,j\}\,. \tag{5.21}$$

Furthermore, the definition of $\boldsymbol{Y}$ in (2.26) and the absence of (anti-) parallel branches by Assumption 8 implies

$$\begin{aligned}
[\boldsymbol{Y}]_{i,j} &= \boldsymbol{e}_i^{\mathrm{T}} \boldsymbol{Y} \boldsymbol{e}_j \\
&= \boldsymbol{e}_i^{\mathrm{T}} \sum_{n \in \mathcal{V}} \boldsymbol{e}_n \Big[\alpha_n \boldsymbol{e}_n^{\mathrm{T}} + \sum_{k \in \hat{\mathcal{B}}_{\mathcal{E}}(n)} \hat{\beta}_k \boldsymbol{e}_{\check{\epsilon}(k)}^{\mathrm{T}} + \sum_{k \in \check{\mathcal{B}}_{\mathcal{E}}(n)} \check{\beta}_k \boldsymbol{e}_{\hat{\epsilon}(k)}^{\mathrm{T}} \Big] \boldsymbol{e}_j \\
&= \Big[\alpha_i \boldsymbol{e}_i^{\mathrm{T}} + \sum_{k \in \hat{\mathcal{B}}_{\mathcal{E}}(i)} \hat{\beta}_k \boldsymbol{e}_{\check{\epsilon}(k)}^{\mathrm{T}} + \sum_{k \in \check{\mathcal{B}}_{\mathcal{E}}(i)} \check{\beta}_k \boldsymbol{e}_{\hat{\epsilon}(k)}^{\mathrm{T}} \Big] \boldsymbol{e}_j \\
&= \hat{\beta}_k
\end{aligned} \tag{5.22}$$

and, analogously, that $[\boldsymbol{Y}]_{j,i} = \check{\beta}_k$. Therewith, it follows that

$$[\boldsymbol{P}_i]_{i,j} = \hat{\beta}_k/2 \qquad [\boldsymbol{P}_j]_{i,j} = \check{\beta}^*_k/2 \tag{5.23}$$
$$[\boldsymbol{Q}_i]_{i,j} = -\hat{\beta}_k/(2\mathbf{i}) \qquad [\boldsymbol{Q}_j]_{i,j} = \check{\beta}^*_k/(2\mathbf{i})\,. \tag{5.24}$$

As $\boldsymbol{M}_n$ in (2.51) is diagonal, $[\boldsymbol{M}_n]_{i,j} = 0$, for all $n \in \mathcal{V}$. The analysis of the remaining coefficient matrices in Table 2.1 completes the proof. □

Lemma 5. *Consider the total voltage ratio ρ_k in* (2.10) *and, for $k \in \mathcal{E}$, let $\mathcal{H}_k \subset \mathbb{C}$ be a half-space with normal ρ_k, i.e.,*

$$\mathcal{H}_k = \{x \in \mathbb{C} : \mathrm{Re}(\rho_k^* x) \leq 0\}\,. \tag{5.25}$$

Under Assumption 2 and Assumption 4 – 7, for all $k \in \mathcal{E}$,

$$\operatorname{cone}(\mathcal{K}_k) \subseteq \mathcal{H}_k \,. \tag{5.26}$$

Proof. In the following, to simplify the exposition, for $x \in \mathbb{C} \setminus \{0\}$ and $\theta \in \mathbb{R}$ we use $\theta \equiv \arg(x)$ to denote that $\exp(\mathbf{i}\theta) = \exp(\mathbf{i}\arg(x))$, i.e., equivalence under the projection onto the principal interval $(-\pi, \pi]$. Corollary 5 states that $\operatorname{cone}(\mathcal{K}_k)$ is described by the arguments of all nonzero elements of $\mathcal{K}_k$. Considering that $\bar{y}_k \neq 0$ and $\rho_k \neq 0$ by the definition of the model in Chapter 2, and using (2.17) and

$$\varphi_k = \arg(-\rho_k) \equiv \pi + \arg(\rho_k) \tag{5.27}$$

the arguments can be expressed as follows.

$$\begin{aligned}
\arg(-1) &= \pi \equiv \varphi_k - \arg(\rho_k) && \text{(5.28a)}\\
\arg(\hat{\beta}_k/2) &= \arg(-\rho_k\bar{y}_k/2) \equiv \varphi_k + \arg(\bar{y}_k) && \text{(5.28b)}\\
\arg(\check{\beta}_k^*/2) &= \arg(-\rho_k\bar{y}_k^*/2) \equiv \varphi_k - \arg(\bar{y}_k) && \text{(5.28c)}\\
\arg(-\hat{\beta}_k/(2\mathbf{i})) &= \arg(\rho_k\bar{y}_k/(2\mathbf{i})) \equiv \varphi_k + \pi/2 + \arg(\bar{y}_k) && \text{(5.28d)}\\
\arg(\check{\beta}_k^*/(2\mathbf{i})) &= \arg(-\rho_k\bar{y}_k^*/(2\mathbf{i})) \equiv \varphi_k - \pi/2 - \arg(\bar{y}_k) && \text{(5.28e)}\\
\arg(\hat{\alpha}_k^*\hat{\beta}_k) &= \arg(|\hat{\rho}_k|^2(\bar{y}_k^* + \hat{y}_k^*)(-\rho_k\bar{y}_k))\\
&= \arg(-\rho_k|\hat{\rho}_k|^2|\bar{y}_k|^2[1 + \hat{y}_k^*\bar{y}_k/|\bar{y}_k|^2])\\
&\equiv \varphi_k + \arg(1 + \hat{y}_k^*\bar{y}_k/|\bar{y}_k|^2) && \text{(5.28f)}\\
\arg(\check{\alpha}_k\check{\beta}_k^*) &= \arg(|\check{\rho}_k|^2(\bar{y}_k + \check{y}_k)(-\rho_k\bar{y}_k^*))\\
&= \arg(-\rho_k|\check{\rho}_k|^2|\bar{y}_k|^2[1 + \check{y}_k\bar{y}_k^*/|\bar{y}_k|^2])\\
&\equiv \varphi_k + \arg(1 + \check{y}_k\bar{y}_k^*/|\bar{y}_k|^2) && \text{(5.28g)}\\
\arg(\tan(\underline{\delta}_k) + \mathbf{i}) &= \pi/2 - \underline{\delta}_k && \text{(5.28h)}\\
\arg(-\tan(\bar{\delta}_k) - \mathbf{i}) &= 3\pi/2 - \bar{\delta}_k && \text{(5.28i)}
\end{aligned}$$

Assumption 2 and Assumption 4 imply that $\bar{y}_k$ is in the fourth quadrant of the complex plane, thus $-\pi/2 \leq \arg(\bar{y}_k) \leq 0$. From Assumption 5 it follows that

$$\left|\frac{\hat{y}_k^*\bar{y}_k}{|\bar{y}_k|^2}\right| = \frac{|\hat{y}_k||\bar{y}_k|}{|\bar{y}_k|^2} = \frac{|\hat{y}_k|}{|\bar{y}_k|} \leq 1 \tag{5.29}$$

$$\left|\frac{\check{y}_k\bar{y}_k^*}{|\bar{y}_k|^2}\right| = \frac{|\check{y}_k||\bar{y}_k|}{|\bar{y}_k|^2} = \frac{|\check{y}_k|}{|\bar{y}_k|} \leq 1 \,. \tag{5.30}$$

Consequently, the values $1 + \hat{y}_k^* \bar{y}_k / |\bar{y}_k|^2$ and $1 + \check{y}_k \bar{y}_k^* / |\bar{y}_k|^2$ are in the right half of the complex plane, which implies that

$$-\pi/2 \leq \arg(1 + \hat{y}_k^* \bar{y}_k / |\bar{y}_k|^2) \leq \pi/2 \tag{5.31}$$

$$-\pi/2 \leq \arg(1 + \check{y}_k \bar{y}_k^* / |\bar{y}_k|^2) \leq \pi/2 \,. \tag{5.32}$$

Furthermore, Assumption 6 states that $-\pi/2 \leq \arg(\rho_k) \leq \pi/2$ and together with Assumption 7 it follows that

$$\varphi_k - \pi/2 \leq \pi/2 - \underline{\delta}_k < \varphi_k - \arg(\rho_k) \tag{5.33}$$

$$\varphi_k - \arg(\rho_k) < 3\pi/2 - \bar{\delta}_k \leq \varphi_k + \pi/2 \,. \tag{5.34}$$

This analysis of the arguments in (5.28) shows that

$$\forall x \in \mathcal{K}_k \setminus \{0\} : \quad \arg(x) \equiv \theta \quad \text{for some} \quad \theta \in [\varphi_k - \pi/2, \varphi_k + \pi/2] \,. \tag{5.35}$$

In order to utilize Corollary 5 for a characterization of $\mathrm{cone}(\mathcal{K}_k)$ based on (5.35), let

$$\xi = \exp(\mathbf{i}\varphi_k) = \exp(\mathbf{i}[\pi + \arg(\rho_k)]) = -\rho_k / |\rho_k| \tag{5.36}$$

and consider the conic combination of ξ, $\mathbf{i}\xi$, and $-\mathbf{i}\xi$ given by

$$\bar{\xi} = \alpha\xi + \alpha^+(\mathbf{i}\xi) + \alpha^-(-\mathbf{i}\xi) = \xi[\alpha + \mathbf{i}(\alpha^+ - \alpha^-)] \tag{5.37}$$

with $\alpha, \alpha^+, \alpha^- \in \mathbb{R}_+$. Then, for $\alpha = 1$,

$$\arg(\bar{\xi}) \equiv \arg(\xi) + \arg(1 + \mathbf{i}[\alpha^+ - \alpha^-]) \equiv \varphi_k + \arctan(\alpha^+ - \alpha^-) \tag{5.38}$$

and, for $\alpha = 0$,

$$\arg(\bar{\xi}) \equiv \varphi_k + \pi/2 \qquad \text{if} \qquad \alpha^+ > 0 \ \wedge \ \alpha^- = 0 \tag{5.39}$$

$$\arg(\bar{\xi}) \equiv \varphi_k - \pi/2 \qquad \text{if} \qquad \alpha^+ = 0 \ \wedge \ \alpha^- > 0 \,. \tag{5.40}$$

Considering that $\arctan : \mathbb{R} \to (-\pi/2, \pi/2)$, these conic combinations show that

$$\begin{aligned} &\forall \theta \in [\varphi_k - \pi/2, \varphi_k + \pi/2] : \\ &\qquad \exists x \in \mathrm{cone}(\{\xi, \mathbf{i}\xi, -\mathbf{i}\xi\}) \setminus \{0\} \quad \text{such that} \quad \theta \equiv \arg(x) \end{aligned} \tag{5.41}$$

and, therefore, (5.35) and Corollary 5 imply that

$$\operatorname{cone}(\mathcal{K}_k) \subseteq \operatorname{cone}(\{\xi, \mathbf{i}\xi, -\mathbf{i}\xi\})\,. \tag{5.42}$$

Furthermore, it follows from the definition of ξ that $\rho_k^*\xi = -|\rho_k|$ and thus

$$\operatorname{Re}(\rho_k^*\bar{\xi}) = -|\rho_k| \operatorname{Re}(\alpha + \mathbf{i}[\alpha^+ - \alpha^-]) = -\alpha|\rho_k| \leq 0 \tag{5.43}$$

for all $\alpha, \alpha^+, \alpha^- \in \mathbb{R}_+$. Therefore,

$$\operatorname{cone}(\{\xi, \mathbf{i}\xi, -\mathbf{i}\xi\}) \subseteq \{x \in \mathbb{C} : \operatorname{Re}(\rho_k^* x) \leq 0\} = \mathcal{H}_k \tag{5.44}$$

which, together with (5.42), completes the proof. □

Lemma 6. *Consider any $k \in \mathcal{E}$ and let $i = \hat{\epsilon}(k)$ and $j = \check{\epsilon}(k)$. It holds that*

$$\forall n \in \mathcal{V} \setminus \{i, j\} : \quad [\boldsymbol{P}_n]_{i,j} = 0 \tag{5.45}$$

and, under Assumption 3 and Assumption 8, that

$$[\boldsymbol{P}_i]_{i,j} \in \operatorname{int}(\mathcal{H}_k) \qquad \textit{and} \qquad [\boldsymbol{P}_j]_{i,j} \in \operatorname{int}(\mathcal{H}_k)\,. \tag{5.46}$$

Proof. The statement (5.45) follows from the intermediate result (5.18) in the proof of Lemma 4. Furthermore, under Assumption 8, the same proof arrives at (5.23) and, with the definition of $\hat{\beta}_k$ and $\check{\beta}_k$ in (2.17), this results in

$$[\boldsymbol{P}_i]_{i,j} = \hat{\beta}_k/2 = -\rho_k \bar{y}_k/2 \tag{5.47}$$

$$[\boldsymbol{P}_j]_{i,j} = \check{\beta}_k^*/2 = -\rho_k \bar{y}_k^*/2\,. \tag{5.48}$$

Considering that $\operatorname{Re}(\bar{y}_k) > 0$ by Assumption 3, this implies that

$$\operatorname{Re}(\rho_k^*[\boldsymbol{P}_i]_{i,j}) = -\frac{|\rho_k|^2}{2} \operatorname{Re}(\bar{y}_k) < 0 \tag{5.49}$$

$$\operatorname{Re}(\rho_k^*[\boldsymbol{P}_j]_{i,j}) = -\frac{|\rho_k|^2}{2} \operatorname{Re}(\bar{y}_k^*) < 0 \tag{5.50}$$

and Proposition 4 completes the proof. □

5.1.3 A Characterization of Exactness

In the following, a mathematical study and characterization of exactness of the SDR and SOCR of the OPF problem in Chapter 3 under the *hybrid architecture* is presented. To focus the exposition, it is observed that exactness of the SOCR (3.18) implies exactness of the SDR (3.14): If an optimizer $(\boldsymbol{V}^\star, \boldsymbol{f}^\star, \boldsymbol{s}_{\mathcal{I}}^\star)$ of (3.18) permits a rank-1 completion $\boldsymbol{v}^\star(\boldsymbol{v}^\star)^{\mathrm{H}}$ of $\boldsymbol{V}^\star$, i.e., $\mathscr{P}(\boldsymbol{v}^\star(\boldsymbol{v}^\star)^{\mathrm{H}}) = \boldsymbol{V}^\star$, then $(\boldsymbol{v}^\star(\boldsymbol{v}^\star)^{\mathrm{H}}, \boldsymbol{f}^\star, \boldsymbol{s}_{\mathcal{I}}^\star)$ is an optimizer of the SDR (3.14) and $(\boldsymbol{v}^\star, \boldsymbol{f}^\star, \boldsymbol{s}_{\mathcal{I}}^\star)$ is an optimizer of the OPF problem (3.12). Correspondingly, the discussion hereafter targets a characterization of exactness of the SOCR (3.18). In order to simplify the presentation of the following results, it is assumed throughout that the power system exhibits the *hybrid architecture* in Definition 13, that Assumption 2 – 8 holds, and that the SOCR (3.18) obtains strong duality. Regarding the latter, see the respective discussion in Section 4.2.2 and Proposition 3. It should be pointed out that some intermediate results do not depend on all of the aforementioned assumptions, where the specific dependencies are evident from the respective proofs. To begin with, consider the following results.

Lemma 7. *Let* $(\boldsymbol{V}, \boldsymbol{f}, \boldsymbol{s}_{\mathcal{I}})$ *be feasible in* (3.18)*. Then, for all* $n \in \mathcal{V}$, $[\boldsymbol{V}]_{n,n} > 0$.

Proof. Due to (3.18b), the voltage constraints (2.52) in $\mathcal{X}$ in (3.10), and $\underline{V}_n > 0$, feasibility in (3.18) implies that $\mathrm{tr}(\boldsymbol{M}_n\boldsymbol{V}) = [\boldsymbol{V}]_{n,n} \geq \underline{V}_n^2 > 0$, for all $n \in \mathcal{V}$. □

Theorem 4. *Let* $(\boldsymbol{V}^\star, \boldsymbol{f}^\star, \boldsymbol{s}_{\mathcal{I}}^\star)$ *be an optimizer of the SOCR* (3.18)*. If*

$$\forall k \in \mathcal{E}: \quad \mathrm{rank}(\boldsymbol{S}_k^{\mathrm{T}}\boldsymbol{V}^\star\boldsymbol{S}_k) = 1 \tag{5.51}$$

then $\boldsymbol{V}^\star$ *permits a rank-1 completion and the relaxation is* exact.

Proof. By construction of the SOCR, exactness is obtained if $\boldsymbol{V}^\star$ permits a rank-1 completion. The following constructive proof of rank-1 completability under (5.51) is an adaptation of the method proposed by Gan in [129, Sec. III-B-3] from connected graphs to *forests*, i.e., to acyclic graphs whose connected components are trees.

Due to the *hybrid architecture* in Definition 13, there exists a *unique* path between every two distinct buses $i, j \in \mathcal{V}$ of a connected component in the underlying undirected graph of $\mathcal{G}' = \{\mathcal{V}, \mathcal{E}, \hat{\epsilon}, \check{\epsilon}\}$ and let this path be denoted by the set $\mathcal{P}(i, j)$, which comprises the ordered tuples of adjacent buses along the path from i to j. Define a unique *reference bus* in every subgrid and let $r : \mathcal{V} \to \mathcal{V}$ map a bus n to the reference bus $r(n)$ of its subgrid. To improve readability, let $V_{ij}^\star$ denote $[\boldsymbol{V}^\star]_{i,j}$. By

Lemma 7, $V^\star_{nn} \geq 0$ for all $n \in \mathcal{V}$.[18] Define the (bus voltage) vector $\boldsymbol{v}^\star \in \mathbb{C}^{|\mathcal{V}|}$ as

$$[\boldsymbol{v}^\star]_n = \sqrt{V^\star_{nn}} \exp(-\mathbf{i}\varphi_n) \quad \text{with} \quad \varphi_n = \sum_{(i,j)\in\mathcal{P}(r(n),n)} \arg(V^\star_{ij}) \tag{5.52}$$

where $n \in \mathcal{V}$. Then, $\mathscr{P}(\boldsymbol{v}^\star(\boldsymbol{v}^\star)^{\mathrm{H}}) = \boldsymbol{V}^\star$ as shown below.

For the diagonal, the equivalence follows trivially. To show the equivalence for the off-diagonal elements, consider any $k \in \mathcal{E}$ and let $i = \hat{\epsilon}(k)$ and $j = \check{\epsilon}(k)$. From (5.51) it follows that $\det(\boldsymbol{S}_k^{\mathrm{T}} \boldsymbol{V}^\star \boldsymbol{S}_k) = V^\star_{ii} V^\star_{jj} - |V^\star_{ij}|^2 = 0$ and, by the nonnegativity of the diagonal of $\boldsymbol{V}^\star$, that $|V^\star_{ij}| = \sqrt{V^\star_{ii}}\sqrt{V^\star_{jj}}$. Consequently,

$$[\boldsymbol{v}^\star(\boldsymbol{v}^\star)^{\mathrm{H}}]_{i,j} = [\boldsymbol{v}^\star]_i [\boldsymbol{v}^\star]_j^* = \sqrt{V^\star_{ii}}\sqrt{V^\star_{jj}} \exp(\mathbf{i}(\varphi_j - \varphi_i)) = |V^\star_{ij}| \exp(\mathbf{i} \arg(V^\star_{ij}))$$

where the last equality further considers that $\varphi_j - \varphi_i$ is independent of the ordering of i and j on the path to the reference $r(i) = r(j)$ as the conjugate symmetry of $\boldsymbol{V}^\star$ implies $\arg(V^\star_{ji}) = -\arg(V^\star_{ij})$. Thus, $\boldsymbol{v}^\star(\boldsymbol{v}^\star)^{\mathrm{H}}$ is a rank-1 completion of $\boldsymbol{V}^\star$. □

Theorem 4 states that, *given* an optimizer $(\boldsymbol{V}^\star, \boldsymbol{f}^\star, \boldsymbol{s}^\star_{\mathcal{I}})$ of the SOCR (3.18) which satisfies (5.51), the relaxation is exact under the *hybrid architecture*. Hence, it provides a sufficient condition to detect exactness *a posteriori*, but, by its very nature, it does not facilitate *a priori* insights into a system's tendency toward exactness. In what follows, Theorem 4 is translated into an interpretable *characterization* of exactness. To this end, the *sufficient condition* for *exactness* in (5.51), which is enabled by the *hybrid architecture*, is combined with a *necessary condition* for *optimality* (under strong duality), namely the *complementary slackness*, in order to further utilize the physical properties of the system for a characterization of exactness.

Lemma 8. *Let* $(\boldsymbol{\Lambda}_\mathcal{E}, \boldsymbol{\lambda}_\mathcal{V}, \boldsymbol{\mu})$ *be feasible in* (4.14)*. Then, for all* $k \in \mathcal{E}$*,*

$$[\boldsymbol{\Lambda}_k]_{1,2} = [\boldsymbol{\Lambda}_k]^*_{2,1} = [\Psi(\boldsymbol{\lambda}_\mathcal{V}, \boldsymbol{\mu})]_{\hat{\epsilon}(k),\check{\epsilon}(k)}\,. \tag{5.53}$$

Proof. Considering (4.14b), the definition of $\boldsymbol{S}_k$ in (3.17), and the absence of (anti-) parallel branches by Assumption 8, feasibility of $(\boldsymbol{\Lambda}_\mathcal{E}, \boldsymbol{\lambda}_\mathcal{V}, \boldsymbol{\mu})$ in (4.14) implies that

$$[\Psi(\boldsymbol{\lambda}_\mathcal{V}, \boldsymbol{\mu})]_{\hat{\epsilon}(k),\check{\epsilon}(k)} = \sum_{l\in\mathcal{E}} \boldsymbol{e}^{\mathrm{T}}_{\hat{\epsilon}(k)} \boldsymbol{S}_l \boldsymbol{\Lambda}_l \boldsymbol{S}_l^{\mathrm{T}} \boldsymbol{e}_{\check{\epsilon}(k)} = \boldsymbol{e}_1^{\mathrm{T}} \boldsymbol{\Lambda}_k \boldsymbol{e}_2 = [\boldsymbol{\Lambda}_k]_{1,2} \tag{5.54}$$

while the conjugate symmetry of $\boldsymbol{\Lambda}_k \in \mathbb{S}^2$ completes the proof. □

[18] The second-order cone constraints (3.18c) do *not* ensure nonnegativity of the diagonal if the system contains subgrids that consist of a single bus, which necessitates the recourse to the voltage constraints.

Theorem 5. *Let* $(\boldsymbol{V}^\star, \boldsymbol{f}^\star, \boldsymbol{s}_\mathcal{I}^\star, \boldsymbol{\Lambda}_\mathcal{E}^\star, \boldsymbol{\lambda}_\mathcal{V}^\star, \boldsymbol{\mu}^\star)$ *be a primal and dual optimal solution of the SOCR, i.e., of* (3.18) *and* (4.14)*, and let the sets* $\mathcal{A}_k$*, with* $k \in \mathcal{E}$*, be defined as*

$$\mathcal{A}_k = \left\{(\boldsymbol{\lambda}_\mathcal{V}, \boldsymbol{\mu}) \in \mathbb{R}^2_\mathcal{V} \times \mathbb{R}^{|\mathcal{M}|} : [\Psi(\boldsymbol{\lambda}_\mathcal{V}, \boldsymbol{\mu})]_{\hat{e}(k),\check{e}(k)} = 0\right\}. \tag{5.55}$$

For any $k \in \mathcal{E}$*, if* $(\boldsymbol{\lambda}_\mathcal{V}^\star, \boldsymbol{\mu}^\star) \notin \mathcal{A}_k$*, then* $\operatorname{rank}(\boldsymbol{S}_k^\mathrm{T} \boldsymbol{V}^\star \boldsymbol{S}_k) = 1$.

Proof. Due to strong duality, *complementary slackness* [42] holds at optimality. For the matrix inequalities (3.18c), this states that, for all $k \in \mathcal{E}$,

$$\operatorname{tr}(\boldsymbol{\Lambda}_k^\star \boldsymbol{S}_k^\mathrm{T} \boldsymbol{V}^\star \boldsymbol{S}_k) = 0 \tag{5.56}$$

and, by Lemma 3, this implies that

$$\operatorname{rank}(\boldsymbol{\Lambda}_k^\star) + \operatorname{rank}(\boldsymbol{S}_k^\mathrm{T} \boldsymbol{V}^\star \boldsymbol{S}_k) \leq 2\,. \tag{5.57}$$

By Lemma 8, if $(\boldsymbol{\lambda}_\mathcal{V}^\star, \boldsymbol{\mu}^\star) \notin \mathcal{A}_k$, then $[\boldsymbol{\Lambda}_k^\star]_{1,2} \neq 0$ and, thus, $\operatorname{rank}(\boldsymbol{\Lambda}_k^\star) \geq 1$, for which (5.57) implies $\operatorname{rank}(\boldsymbol{S}_k^\mathrm{T} \boldsymbol{V}^\star \boldsymbol{S}_k) \leq 1$. By Lemma 7, the diagonal of $\boldsymbol{V}^\star$ is strictly positive and, thus, $\operatorname{rank}(\boldsymbol{S}_k^\mathrm{T} \boldsymbol{V}^\star \boldsymbol{S}_k) \geq 1$. Therefore, if $(\boldsymbol{\lambda}_\mathcal{V}^\star, \boldsymbol{\mu}^\star) \notin \mathcal{A}_k$, then $\operatorname{rank}(\boldsymbol{S}_k^\mathrm{T} \boldsymbol{V}^\star \boldsymbol{S}_k) = 1$. □

Corollary 8. *Let* $(\boldsymbol{V}^\star, \boldsymbol{f}^\star, \boldsymbol{s}_\mathcal{I}^\star, \boldsymbol{\Lambda}_\mathcal{E}^\star, \boldsymbol{\lambda}_\mathcal{V}^\star, \boldsymbol{\mu}^\star)$ *be a primal and dual optimal solution of the SOCR, i.e., of* (3.18) *and* (4.14)*. Then,*

$$(\boldsymbol{\lambda}_\mathcal{V}^\star, \boldsymbol{\mu}^\star) \notin \bigcup_{k \in \mathcal{E}} \mathcal{A}_k \tag{5.58}$$

implies that, for all $k \in \mathcal{E}$*,* $\operatorname{rank}(\boldsymbol{S}_k^\mathrm{T} \boldsymbol{V}^\star \boldsymbol{S}_k) = 1$ *and, thus, the relaxation is* exact*.*

These results translate the *sufficient condition* for *exactness* in Theorem 4 for a *primal optimal solution* to the *avoidance* of the sets $\mathcal{A}_k$ in *dual optimality*, i.e., the property (5.58) of a dual optimal solution implies exactness of the relaxation. In order to render the condition (5.58) interpretable, the structure of the sets $\mathcal{A}_k$ is analyzed.

Theorem 6. *For all* $k \in \mathcal{E}$*,* $\mathcal{A}_k$ *is a proper affine subspace and*

$$2|\mathcal{V}| + |\mathcal{M}| - 2 \leq \dim(\mathcal{A}_k) \leq 2|\mathcal{V}| + |\mathcal{M}| - 1\,. \tag{5.59}$$

Proof. Consider a tuple $(\boldsymbol{\lambda}_\mathcal{V}, \boldsymbol{\mu}) \in \mathbb{R}^2_\mathcal{V} \times \mathbb{R}^{|\mathcal{M}|}$ and let

$$\boldsymbol{\xi} = \left[\boldsymbol{\lambda}_1^\mathrm{T}, \ldots, \boldsymbol{\lambda}_{|\mathcal{V}|}^\mathrm{T}, \boldsymbol{\mu}^\mathrm{T}\right]^\mathrm{T} \in \mathbb{R}^{2|\mathcal{V}|+|\mathcal{M}|} \tag{5.60}$$

and

$$\boldsymbol{\chi} = \left[\, \mathbf{1}_{|\mathcal{V}|}^{\mathrm{T}} \otimes [\, \tau,\ 0\,],\ \mathbf{0}_{|\mathcal{M}|}^{\mathrm{T}} \,\right]^{\mathrm{T}} \in \mathbb{R}^{2|\mathcal{V}|+|\mathcal{M}|} \tag{5.61}$$

in which $\mathbf{1}_{|\mathcal{V}|} \in \mathbb{R}^{|\mathcal{V}|}$ is the all-ones vector, $\mathbf{0}_{|\mathcal{M}|} \in \mathbb{R}^{|\mathcal{M}|}$ the zero vector, and "$\otimes$" denotes the Kronecker product. Consider some $k \in \mathcal{E}$, let $i = \hat{\epsilon}(k)$ and $j = \check{\epsilon}(k)$, let

$$\boldsymbol{Z}'_{k,n} = \left[[\boldsymbol{P}_n]_{i,j}\,,\ [\boldsymbol{Q}_n]_{i,j} \right] \in \mathbb{C}^{1\times 2}, \quad \forall n \in \mathcal{V} \tag{5.62}$$

$$\boldsymbol{Z}''_{k} = \left[[\boldsymbol{C}_1]_{i,j}\,,\ \ldots\,,\ [\boldsymbol{C}_{|\mathcal{M}|}]_{i,j} \right] \in \mathbb{C}^{1\times|\mathcal{M}|} \tag{5.63}$$

and let $\boldsymbol{Z}_k \in \mathbb{R}^{2\times(2|\mathcal{V}|+|\mathcal{M}|)}$ be defined as

$$\boldsymbol{Z}_k = \begin{bmatrix} \mathrm{Re}(\boldsymbol{Z}'_{k,1}) & \ldots & \mathrm{Re}(\boldsymbol{Z}'_{k,|\mathcal{V}|}) & \mathrm{Re}(\boldsymbol{Z}''_{k}) \\ \mathrm{Im}(\boldsymbol{Z}'_{k,1}) & \ldots & \mathrm{Im}(\boldsymbol{Z}'_{k,|\mathcal{V}|}) & \mathrm{Im}(\boldsymbol{Z}''_{k}) \end{bmatrix}. \tag{5.64}$$

Therewith, $\mathcal{A}_k$ can be expressed as

$$\mathcal{A}_k = \{\, \boldsymbol{\xi} \in \mathbb{R}^{2|\mathcal{V}|+|\mathcal{M}|} : \boldsymbol{Z}_k(\boldsymbol{\xi}+\boldsymbol{\chi}) = \mathbf{0} \,\} = \mathrm{null}(\boldsymbol{Z}_k) - \{\boldsymbol{\chi}\} \tag{5.65}$$

which is an affine subspace. Furthermore, it follows from Lemma 6 and Corollary 6 that $[\boldsymbol{P}_i]_{i,j} \neq 0$ and $[\boldsymbol{P}_j]_{i,j} \neq 0$, thus $\boldsymbol{Z}_k \neq \mathbf{0}$ and $1 \leq \mathrm{rank}(\boldsymbol{Z}_k) \leq 2$. The *rank-nullity theorem* [92] completes the proof. □

Therefore, the sets $\mathcal{A}_k$ are proper affine subspaces in the $(2|\mathcal{V}|+|\mathcal{M}|)$-dimensional Euclidean space and, thus, have *zero volume* (Lebesgue measure zero). Furthermore, as shown below, these affine subspaces adopt a particular location and orientation in the ambient space – roughly speaking, to support a first reading, they essentially do not intersect the nonnegative orthant with respect to the first $2|\mathcal{V}|$ dimensions.

Theorem 7. *Let* $(\boldsymbol{\Lambda}^\star_{\mathcal{E}}, \boldsymbol{\lambda}^\star_{\mathcal{V}}, \boldsymbol{\mu}^\star)$ *be an optimizer of the SOCR dual* (4.14)*. Consider any* $k \in \mathcal{E}$ *and let* $i = \hat{\epsilon}(k)$ *and* $j = \check{\epsilon}(k)$*. If*

$$\boldsymbol{\lambda}^\star_i \geq -\tau\boldsymbol{e}_1 \quad \wedge \quad \boldsymbol{\lambda}^\star_j \geq -\tau\boldsymbol{e}_1 \quad \wedge \quad [\boldsymbol{\lambda}^\star_i]_1 + [\boldsymbol{\lambda}^\star_j]_1 > -2\tau \tag{5.66}$$

then $(\boldsymbol{\lambda}^\star_{\mathcal{V}}, \boldsymbol{\mu}^\star) \notin \mathcal{A}_k$*.*

Proof. By definition, $\boldsymbol{\lambda}^\star_n + \tau\boldsymbol{e}_1 \geq \mathbf{0}$, $\forall n \in \{i, j\}$, and $\boldsymbol{\mu}^\star \geq \mathbf{0}$. Therewith, Lemma 4, (the first statement of) Lemma 6, and Definition 14 implies $[\Psi(\boldsymbol{\lambda}^\star_{\mathcal{V}}, \boldsymbol{\mu}^\star)]_{i,j} \in \mathrm{cone}(\mathcal{K}_k)$ and Lemma 5 states that $[\Psi(\boldsymbol{\lambda}^\star_{\mathcal{V}}, \boldsymbol{\mu}^\star)]_{i,j} \in \mathcal{H}_k$. Furthermore, Lemma 6, Corollary 7,

and Proposition 5 implies

$$([\boldsymbol{\lambda}_i^\star]_1 + \tau)[\boldsymbol{P}_i]_{i,j} + ([\boldsymbol{\lambda}_j^\star]_1 + \tau)[\boldsymbol{P}_j]_{i,j} \in \operatorname{int}(\mathcal{H}_k)\,. \tag{5.67}$$

As the left-hand side in (5.67) is a summand in $[\Psi(\boldsymbol{\lambda}_\mathcal{V}^\star, \boldsymbol{\mu}^\star)]_{i,j}$, Proposition 5 yields

$$[\Psi(\boldsymbol{\lambda}_\mathcal{V}^\star, \boldsymbol{\mu}^\star)]_{i,j} \in \operatorname{int}(\mathcal{H}_k) \tag{5.68}$$

for which Corollary 6 implies $[\Psi(\boldsymbol{\lambda}_\mathcal{V}^\star, \boldsymbol{\mu}^\star)]_{i,j} \neq 0$. Thus, $(\boldsymbol{\lambda}_\mathcal{V}^\star, \boldsymbol{\mu}^\star) \notin \mathcal{A}_k$. □

Corollary 9. *Let* $(\boldsymbol{V}^\star, \boldsymbol{f}^\star, \boldsymbol{s}_\mathcal{I}^\star, \boldsymbol{\Lambda}_\mathcal{E}^\star, \boldsymbol{\lambda}_\mathcal{V}^\star, \boldsymbol{\mu}^\star)$ *be a primal and dual optimal solution of the SOCR, i.e., of* (3.18) *and* (4.14)*. If, for all* $n \in \mathcal{V}$*,*

$$[\boldsymbol{\lambda}_n^\star]_1 > -\tau \qquad \wedge \qquad [\boldsymbol{\lambda}_n^\star]_2 \geq 0 \tag{5.69}$$

then, for all $k \in \mathcal{E}$*,* $\operatorname{rank}(\boldsymbol{S}_k^{\mathrm{T}} \boldsymbol{V}^\star \boldsymbol{S}_k) = 1$ *and, thus, the relaxation is* exact*.*

With these results, the *sufficient condition for exactness* in Theorem 4 in the *primal domain* is translated into a *characterization of exactness* in the *dual domain*. In order to render this characterization interpretable, Theorem 3 and its interpretation in Chapter 4 shall be recalled: If the SOCR is exact (and obtains strong duality), then the optimal dual variables $\boldsymbol{\lambda}_\mathcal{V}^\star$ are the LMPs. Thus, for injection cost minimization ($\tau = 0$), Corollary 9 states that if the LMP of active power is positive and the LMP of reactive power is nonnegative at all buses, then exactness of the relaxation is *guaranteed*. Furthermore, if a loss penalty is included ($\tau > 0$), then the requirement on the LMP of active power is relaxed to exceeding the negative threshold $-\tau$. Under typical operating conditions, a predominantly nonnegative price profile is generally observed (see also the related study and discussion in [2, Sec. VIII and App. F]). By the nature of LMPs (see Section 4.1), this is evident for active power due to the generally *increasing* injection cost functions, but it may not be obvious for reactive power in AC subgrids that is usually associated with zero cost. In this case, if the constraints on reactive power injections are not binding, then the LMP is zero, and, if they are binding, it is often due to a demand for capacitive reactive power which induces a positive price. However, buses with negative LMPs do arise, e.g., in case of a demand for more inductive reactive power. Still, exactness obtains as long as the optimal dual variables are not forced into the union of the affine subspaces $\mathcal{A}_k$, see Corollary 8. In case that the optimal dual variables do lie in the union of the affine subspaces $\mathcal{A}_k$, exactness may be compromised. Then, as shown by Theorem 8 below, the optimal dual variable of at least one psd constraint in (3.18c) on the 2×2 principal

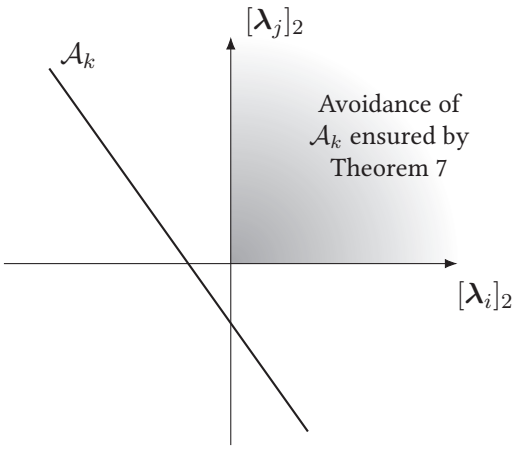

Figure 5.1: Qualitative illustration of pathological price profiles [2].

submatrices of $\boldsymbol{V}^\star$ is zero. This indicates potential inactivity of the corresponding constraint, while inactivity implies that the respective 2×2 principal submatrix of $\boldsymbol{V}^\star$ is rank-2 and the sufficient condition for exactness in Theorem 4 is violated. As a means to refer to such an unfortunate LMP constellation, the notion of a *pathological price profile* is introduced in Definition 16.

Theorem 8. *Let* $(\boldsymbol{V}^\star, \boldsymbol{f}^\star, \boldsymbol{s}_{\mathcal{I}}^\star, \boldsymbol{\Lambda}_{\mathcal{E}}^\star, \boldsymbol{\lambda}_{\mathcal{V}}^\star, \boldsymbol{\mu}^\star)$ *be a primal and dual optimal solution of the SOCR, i.e., of* (3.18) *and* (4.14)*. For any* $k \in \mathcal{E}$*, if* $(\boldsymbol{\lambda}_{\mathcal{V}}^\star, \boldsymbol{\mu}^\star) \in \mathcal{A}_k$*, then* $\boldsymbol{\Lambda}_k^\star = \boldsymbol{0}$*.*

Proof. It follows from $(\boldsymbol{\lambda}_{\mathcal{V}}^\star, \boldsymbol{\mu}^\star) \in \mathcal{A}_k$ and Lemma 8 that $[\boldsymbol{\Lambda}_k^\star]_{1,2} = [\boldsymbol{\Lambda}_k^\star]_{2,1}^* = 0$, while (4.14d) implies $[\boldsymbol{\Lambda}_k^\star]_{1,1} \geq 0$ and $[\boldsymbol{\Lambda}_k^\star]_{2,2} \geq 0$. Furthermore, it follows from Lemma 7 that $[\boldsymbol{S}_k^{\mathrm{T}} \boldsymbol{V}^\star \boldsymbol{S}_k]_{1,1} > 0$ and $[\boldsymbol{S}_k^{\mathrm{T}} \boldsymbol{V}^\star \boldsymbol{S}_k]_{2,2} > 0$. Thus, the *complementary slackness* in (5.56) forces the sum of the positively weighted diagonal elements of $\boldsymbol{\Lambda}_k^\star$ to zero, which implies that $[\boldsymbol{\Lambda}_k^\star]_{1,1} = [\boldsymbol{\Lambda}_k^\star]_{2,2} = 0$. Hence, $\boldsymbol{\Lambda}_k^\star = \boldsymbol{0}$. □

Definition 16. If an optimizer $(\boldsymbol{\Lambda}_{\mathcal{E}}^\star, \boldsymbol{\lambda}_{\mathcal{V}}^\star, \boldsymbol{\mu}^\star)$ of the SOCR dual (4.14) satisfies

$$(\boldsymbol{\lambda}_{\mathcal{V}}^\star, \boldsymbol{\mu}^\star) \in \bigcup_{k\in\mathcal{E}} \mathcal{A}_k \tag{5.70}$$

then the $|\mathcal{V}|$-tuple $\boldsymbol{\lambda}_{\mathcal{V}}^\star$ is a *pathological price profile*.

To illustrate pathological price profiles, consider an optimizer $(\boldsymbol{\Lambda}_{\mathcal{E}}^\star, \boldsymbol{\lambda}_{\mathcal{V}}^\star, \boldsymbol{\mu}^\star)$ of the SOCR dual (4.14) and suppose that all affine subspaces are avoided except the subspace $\mathcal{A}_k$ associated with AC branch k, i.e., $(\boldsymbol{\lambda}_{\mathcal{V}}^\star, \boldsymbol{\mu}^\star) \notin \bigcup_{l\in\mathcal{E}\setminus\{k\}} \mathcal{A}_l$. In this case, exactness is guaranteed by Corollary 8 if $\mathcal{A}_k$ is avoided, i.e., $(\boldsymbol{\lambda}_{\mathcal{V}}^\star, \boldsymbol{\mu}^\star) \notin \mathcal{A}_k$. Let

$i = \hat{\epsilon}(k)$ and $j = \check{\epsilon}(k)$ denote the adjacent buses of branch k and suppose that the LMP for *active* power at bus i and j exceeds the threshold $-\tau$. From Theorem 7, it follows that exactness is then determined by the LMP for *reactive* power at bus i and j, i.e., $[\boldsymbol{\lambda}_i^\star]_2$ and $[\boldsymbol{\lambda}_j^\star]_2$. For this setting, the pathological price profiles can be visualized qualitatively as depicted in Figure 5.1:[19] Exactness of the SOCR may only be lost if the optimal dual variables $[\boldsymbol{\lambda}_i^\star]_2$ and $[\boldsymbol{\lambda}_j^\star]_2$ combine to a point on the $\mathcal{A}_k$-line, while in all other cases exactness is guaranteed. Considering the nature of LMPs as well as their sensitivity to operating conditions, this appears unlikely – or *pathological*. The argument of this example extends similarly to further subspaces and LMPs. In this context, it is worth noting that, for some branch k, the avoidance of $\mathcal{A}_k$ depends *exclusively* on the LMPs at the adjacent buses $\hat{\epsilon}(k)$ and $\check{\epsilon}(k)$. This follows from the definition of $\mathcal{A}_k$ and $\Psi(\boldsymbol{\lambda}_\mathcal{V}, \boldsymbol{\mu})$ in (5.55) and (4.3a) in conjunction with the properties (5.18) and (5.21) of the coefficient matrices $\boldsymbol{P}_n$ and $\boldsymbol{Q}_n$.

This characterization of exactness explains the strong tendency toward exactness under the *hybrid architecture*, which is confirmed by the case studies in Chapter 7 later on. Finally, before moving on to an engineering interpretation of the *hybrid architecture*, two further conclusions from this result on exactness are presented.

Remark 1 ("Load Over-Satisfaction"). In the literature, many results on exactness including [52,60,124,125] require the (mathematically motivated) technical condition of "load over-satisfaction", i.e., the omission of power injection lower bounds. This corresponds to replacing the power flow *equations* in (3.10b) and (3.10c) by *inequalities*, i.e., the power flow into the grid (left-hand side) is only upper-bounded by the power injections (right-hand side). In this case, the optimal dual variables $\boldsymbol{\lambda}_\mathcal{V}^\star$ are *nonnegative* by definition. Correspondingly, with a loss penalty $\tau > 0$, Corollary 9 actually *guarantees* exactness. In this sense, the results presented here may be considered as a generalization of the aforementioned works, as it a applies to a more general system model, network topology, and OPF formulation, while it also extends the characterization of exactness beyond this technical condition.

Remark 2 (Regularization). In Corollary 9, it can be observed that the loss penalty, which is parameterized by τ, acts as a *regularization* toward exactness: If the loss penalty is increased, the condition on the LMPs for active power is relaxed. This regularization may be extended by introducing an analogous penalty term $\hat{\tau}\hat{L}(\boldsymbol{V}, \boldsymbol{f})$ with $\hat{\tau} \in \mathbb{R}_+$ for *reactive* power to the OPF objective. Then, the condition on the

[19] Figure 5.1 is the projection of a cut through the ambient space of $\mathcal{A}_k$. This cut is parallel to the $[\boldsymbol{\lambda}_i]_2$-$[\boldsymbol{\lambda}_j]_2$-plane and includes the point $(\boldsymbol{\lambda}_\mathcal{V}^\star, \boldsymbol{\mu}^\star)$. The shape of $\mathcal{A}_k$ follows from Theorem 6. In this respect, the cut illustrates the worst case ($\boldsymbol{Z}_k$ in (5.65) is rank-1), i.e., a line. The location of $\mathcal{A}_k$ follows from Theorem 7, which states that it does not intersect the nonnegative quadrant.

LMPs that ensures exactness can be relaxed for both active *and* reactive power. In particular, the net reactive power injection function $\hat{L} : \mathbb{S}^{|\mathcal{V}|} \times \mathbb{R}^{4|\mathcal{C}|} \to \mathbb{R}$ is

$$\hat{L}(\boldsymbol{V}, \boldsymbol{f}) = \operatorname{tr}(\hat{\boldsymbol{L}}\boldsymbol{V}) + \hat{\boldsymbol{l}}^{\mathrm{T}}\boldsymbol{f} \tag{5.71}$$

where $\hat{\boldsymbol{L}} \in \mathbb{S}^{|\mathcal{V}|}$ and $\hat{\boldsymbol{l}} \in \mathbb{R}^{4|\mathcal{C}|}$ are defined as

$$\hat{\boldsymbol{L}} = \sum_{n\in\mathcal{V}} \boldsymbol{Q}_n = \sum_{n\in\mathcal{V}} \frac{1}{2\mathbf{i}}(\boldsymbol{Y}^{\mathrm{H}}\boldsymbol{e}_n\boldsymbol{e}_n^{\mathrm{T}} - \boldsymbol{e}_n\boldsymbol{e}_n^{\mathrm{T}}\boldsymbol{Y}) = \frac{1}{2\mathbf{i}}(\boldsymbol{Y}^{\mathrm{H}} - \boldsymbol{Y}) \tag{5.72}$$

and

$$\hat{\boldsymbol{l}} = \sum_{n\in\mathcal{V}} \boldsymbol{q}_n = -\sum_{l\in\mathcal{C}} \left[\boldsymbol{e}_{4l-1} + \boldsymbol{e}_{4l}\right] . \tag{5.73}$$

Then, the condition (5.66) of Theorem 7 develops into

$$\boldsymbol{\lambda}_i^\star \geq -\begin{bmatrix}\tau\\ \hat{\tau}\end{bmatrix} \quad \wedge \quad \boldsymbol{\lambda}_j^\star \geq -\begin{bmatrix}\tau\\ \hat{\tau}\end{bmatrix} \quad \wedge \quad [\boldsymbol{\lambda}_i^\star]_1 + [\boldsymbol{\lambda}_j^\star]_1 > -2\tau \tag{5.74}$$

and, correspondingly, the condition (5.69) of Corollary 9 renders

$$[\boldsymbol{\lambda}_n^\star]_1 > -\tau \qquad \wedge \qquad [\boldsymbol{\lambda}_n^\star]_2 \geq -\hat{\tau}\,. \tag{5.75}$$

In order to interpret this penalization, consider the affine subspaces $\mathcal{A}_k$ as formulated in (5.65), where the offset $\boldsymbol{\chi}$ now comprises $\mathbf{1}_{|\mathcal{V}|}\otimes[\,\tau,\ \hat{\tau}\,]^{\mathrm{T}}$ in the first $2|\mathcal{V}|$ dimensions. Thus, the penalization corresponds to a *translation* of the affine subspaces and the *pathological price profiles* are *shifted* in the direction of negative prices. Furthermore, this translation can be performed individually for every bus by replacing the common penalty factors τ and $\hat{\tau}$ by nodal penalty factors τ_n and $\hat{\tau}_n$ for $(\boldsymbol{P}_n, \boldsymbol{p}_n)$ and $(\boldsymbol{Q}_n, \boldsymbol{q}_n)$ in (2.46), (2.47), (5.72), and (5.73), respectively. Then, the first $2|\mathcal{V}|$ dimensions of $\boldsymbol{\chi}$ in (5.65) render $\left[\,\tau_1,\ \hat{\tau}_1, \ldots,\ \tau_{|\mathcal{V}|},\ \hat{\tau}_{|\mathcal{V}|}\,\right]^{\mathrm{T}}$ and the pathological price profiles can be shifted on a nodal basis (while the condition (5.69) of Corollary 9 refines to $[\boldsymbol{\lambda}_n^\star]_1 > -\tau_n$ and $[\boldsymbol{\lambda}_n^\star]_2 \geq -\hat{\tau}_n$). Thus, in the event of inexactness, a highly targeted regularization toward exactness is possible, where the dual solution $\boldsymbol{\lambda}_{\mathcal{V}}^\star$ with the insights from pathological price profiles guides the selection of appropriate penalties.

5.2 Engineering Interpretation and Design Implications

By developing a characterization of exactness based on LMPs, the previous section illustrates that the SDR and SOCR of the OPF problem exhibits a strong tendency

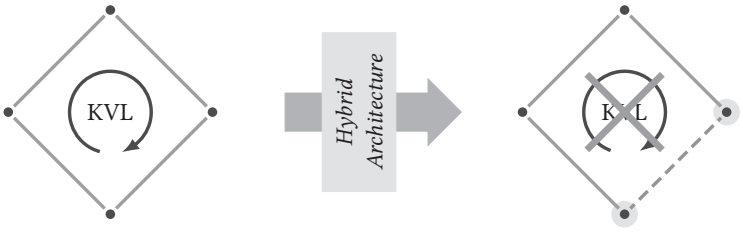

Figure 5.2: Annulment of KVL around a loop of branches by the *hybrid architecture*.

toward exactness under the *hybrid architecture*. Considering that a convex relaxation augments the feasible set of the OPF problem with non-physical states, the SDR and SOCR may be viewed as an OPF formulation in which the physical laws are loosened. From this perspective, inexactness of a relaxation indicates structural limitations of the system such that the additional states, which disobey the physical laws, enable a superior performance in terms of the OPF's objective. In this light, the *hybrid architecture*, which induces a strong tendency toward exactness, may thus be viewed as a *structural transformation* of a system that introduces *flexibility*, as the loosening of physical laws is typically *not* required to achieve optimality under the relaxation.

A closer look at the structural requirements of the *hybrid architecture* reveals that it indeed mitigates restrictions by physical laws via a systematic incorporation of power electronics. The voltages and currents in (the model of) the system are governed by Kirchhoff's laws, i.e., KCL and KVL. KVL states that the sum of the voltages around any closed loop is equal to zero. Thus, for a loop of branches, the sum of the voltages along the branches must vanish. Consequently, if a branch is congested and, hence, the voltage along this branch is constrained, this restriction can "propagate" via KVL to other branches that share a loop with the congested branch. In the *hybrid architecture*, all loops of branches (in the model of the system) are resolved using the controllability of power electronics, which suppresses this "propagation" of restrictions via KVL. This is illustrated in Figure 5.2, which shows a loop of AC branches (solid) and the annulment of KVL around that loop by the conversion of one branch to DC operation (dashed).

The *hybrid architecture* may thus be regarded as a systematic approach to *grid flexibilization* via a structural transformation to a hybrid AC/DC system. It is further supported by the use of VSCs for AC/DC conversion, which provide a rapid and flexible power flow control as well as reactive power compensation [12, 13]. In a system that faces congestion, this flexibilization may increase the *effective transmission capacity*. Additionally, the conversion of AC lines to DC operation enables

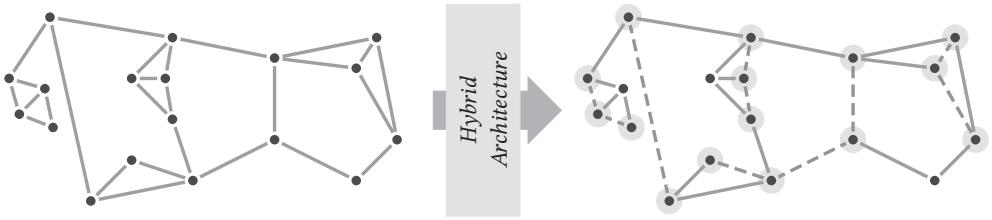

Figure 5.3: Topology-preserving capacity expansion with the *hybrid architecture*.

a major increase in corridor transmission capacity [121, 122], which renders the *hybrid architecture* a *topology-preserving capacity expansion strategy* as illustrated in Figure 5.3.

The structural transformation of an AC power system to the *hybrid architecture*, i.e., the conversion of one AC branch in every loop to DC operation, is often extensive and potentially introduces more flexibility than required. The *hybrid architecture* depends exclusively on the network topology and, therefore, does not inherently focus on the bottlenecks of a given system that arise due to its particular electrical design, injector distribution, and load profiles. Correspondingly, a "focusing" of the *hybrid architecture* to critical parts of the system is in general necessary for the technical and economic viability of this capacity expansion strategy. In the following, two different approaches are presented. The first approach is based on associating a "focused network topology" with the system to which the *hybrid architecture* is applied. In the second approach, the *hybrid architecture* is considered directly on the network topology but only some selected conversion measures are implemented.

5.2.1 Focusing the Hybrid Architecture with Network Reduction

By revisiting Definition 13, it can be observed that the *hybrid architecture* is a structural property of the *system model* and, thus, not an immediate requirement on the physical infrastructure. The purpose of the system model is to adequately describe the system behavior for proper operational planning. Therefore, the detailed model of a large-scale power system may be subjected to *network reduction* in order to reduce the model complexity while retaining an adequate modeling of the system behavior. If the *hybrid architecture* is then applied to the reduced system model, its structural requirements are focused to those parts of the system that are crucial to its behavior, cf. Figure 5.4.

For this purpose, not all network reduction methods are suitable. For example, the popular *Ward equivalent* [130] (see also [131–135]) as well as the *REI equivalent* [136]

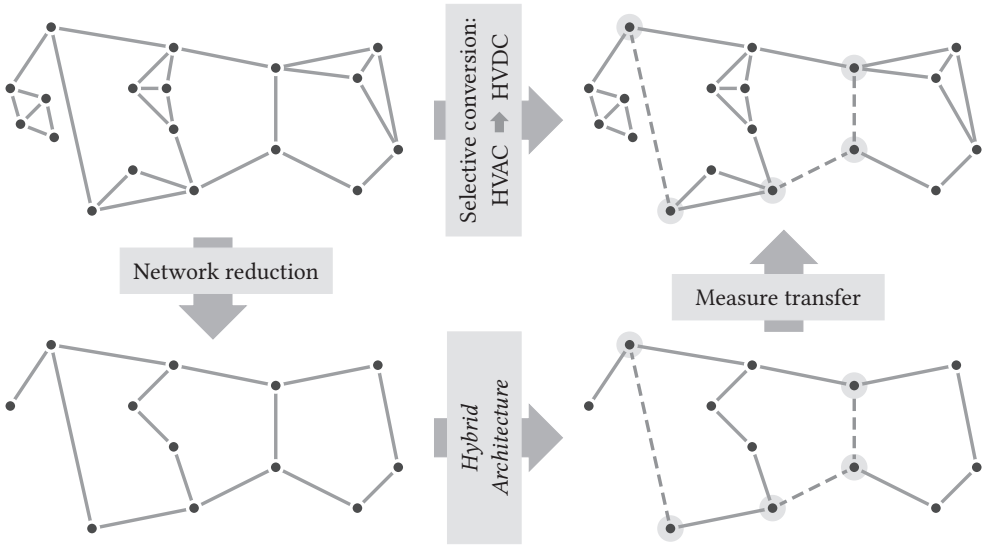

Figure 5.4: Focusing the *hybrid architecture* with network reduction.

(see also [137–141]) introduce *artificial* branches to the reduced model. Then, if the *hybrid architecture* identifies such an artificial branch for conversion to DC operation, there does not exist a physical counterpart that can actually be converted to implement the flexibilization measure. Consequently, a network reduction method is required that maintains a relation of the retained entities to physical counterparts. To this end, we collaborated with Julia Sistermanns and the Professorship for Power Transmission Systems at *Technische Universität München* (TUM) to devise a data-driven feature- and structure-preserving network reduction method for large-scale power systems [7]. This method targets the identification of a multitude of small subgrids within the power grid whose internal structure exhibits a negligible impact on the overall system behavior. These subgrids are selected based on topological, electrical, and market-related characteristics. Subsequently, after an optional feature-based filtering, these subgrids are reduced to designated representative buses in a fashion that avoids the introduction of artificial entities. Therewith, the relation of buses and branches in the reduced model to physical counterparts is maintained, rendering this method applicable to the focusing of the *hybrid architecture*.

A particular characteristic and advantage of the network reduction based focusing of the *hybrid architecture* is that the results on exactness of the relaxations in Section 5.1 hold for the reduced model. Thus, the efficient solution methods for the OPF and LMPs discussed in Chapter 3 and Chapter 4 can be utilized.

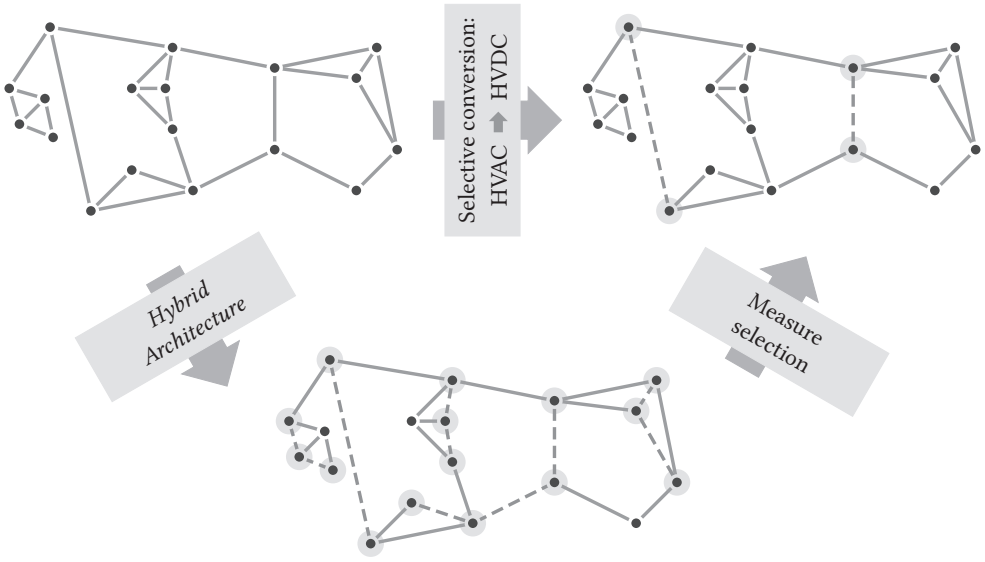

Figure 5.5: Focusing the *hybrid architecture* with measure selection.

5.2.2 Focusing the Hybrid Architecture with Measure Selection

The network reduction based focusing of the *hybrid architecture* concentrates the structural requirements to parts of the system that are crucial to the overall behavior. However, potentially not all parts that are decisive to the overall behavior are actually limiting the system's performance, leading to more grid flexibilization than required.

For a more specific and fine-grained focusing, the impact of the conversion measures proposed by the *hybrid architecture* may be evaluated in a data-driven manner and selected with respect to the objective of the flexibilization as well as other decision criteria, e.g., the suitability for conversion and compatibility with other operational aspects like resilience and switching maneuvers. Therewith, a partial implementation of the *hybrid architecture* with a particular focus of the flexibilization can be obtained, cf. Figure 5.5. In contrast to the network reduction based focusing, the results on exactness of the relaxations in Section 5.1 are then in general not applicable.

6 The Software Framework "*hynet*"

The previous chapters discuss the modeling of hybrid AC/DC power systems, the two central problems of the *optimal power flow* and *locational marginal pricing*, and the *hybrid architecture* as well as the implications of the latter on the design and expansion of power systems. In order to study the operation, expansion, and techno-economic aspects of specific (large-scale) hybrid AC/DC power systems, a software framework for the nontrivial task of the specification, formulation, solution, and evaluation of the OPF problem and the associated LMPs is desired. Furthermore, for transparency, reproducibility, and flexible adoption in research, this framework should be available as open-source software. Several open-source software packages for OPF computation have already been published, including the established toolboxes MATPOWER [84, 142] (and its Python-port PYPOWER [143]) and PSAT [144, 145] as well as the recently released PowerModels [89, 146] and `pandapower` [147, 148]. While PSAT is targeted at small to medium-sized systems, MATPOWER, PowerModels, and `pandapower` also support large-scale systems, but they are limited to a simple model of P2P-HVDC systems and do not support MT-HVDC systems. On the contrary, the open-source software MATACDC [149] features an elaborate model for hybrid AC/DC grids, but it is limited to (sequential) power flow computations.

In order to support the study of large-scale hybrid AC/DC power systems, we developed *hynet* [3, 8], an open-source OPF framework for hybrid AC/DC grids with P2P-HVDC and radial MT-HVDC systems.[20] *hynet* is based on the system model and the theory presented in the previous chapters and, in its design, we emphasized ease of use and extensibility to facilitate its effortless adoption in research and education. To this end, the mathematical foundation was embedded in a clearly structured and flexible object-oriented software design, while the framework was written in the popular high-level open-source programming language Python [72] that is freely available for all major platforms. On the *hynet* project website [8], a

[20] In parallel and independent of our work, another open-source OPF software for hybrid AC/DC grids was proposed in [35]. See the introductory section of Chapter 2 for remarks on modeling aspects.

comprehensive documentation is provided, including an installation guide, a series of tutorials, and a detailed documentation of the source code. Here, this documentation is complemented by relating the modeling and theory in the previous chapters to *hynet*'s software design and presenting an exemplary extension of this framework.

6.1 Fundamental Software Design

The fundamental software design of *hynet* is based on a systematic partitioning of the data flow into object relations as depicted in Figure 6.1 on page 77. This design is complemented by a carefully devised relational database schema to offer an adequate data format for hybrid AC/DC power systems for use in research and education. It is based on the established *structured query language* (SQL) and enables the platform-independent storage of infrastructure and scenario data.

An OPF study is initiated by loading infrastructure and scenario data from a grid database into a scenario object, where the latter organizes the data using *pandas* [150] data frames. Optionally, this scenario may be further adjusted programmatically, e.g., to analyze postulated contingencies or variations of the load profile or RES feed-in from the forecast. The scenario then is used to create an OPF model object, which represents the unified OPF formulation in (3.12) for the given scenario and whose base class implements the system model in Chapter 2. This object serves as a *builder* [151] for the OPF problem, which is represented by an object of a *quadratically-constrained quadratic problem* (QCQP). This QCQP is solved via a solver interface, where the underlying implementation may solve the nonconvex QCQP (3.12), its SDR (3.14), or its SOCR (3.18). A solver further includes an interface to a rank-1 approximator that, in case of a relaxation, facilitates a customized bus voltage recovery. After the solution process, the solver returns an object containing the result and solution process information, which is routed through a *factory function* [151] of the OPF model object to obtain an appropriate representation of the result data.

This object-oriented design offers a transparent structure and data flow, while its ease of use is further supported by a set of convenience functions for standard use cases. Additionally, this design renders *hynet* amenable to extensions via inheritance and standard design patterns. For example, extensions to additional solvers and other relaxations can be implemented via corresponding solver classes. Furthermore, the problem formulation can be customized by subclassing the OPF model or its base class and, by overriding the respective factory function, the result representation can be adjusted. Such a problem customization is exemplified by the *maximum loadability problem*, which is discussed in Section 6.3.1 later on.

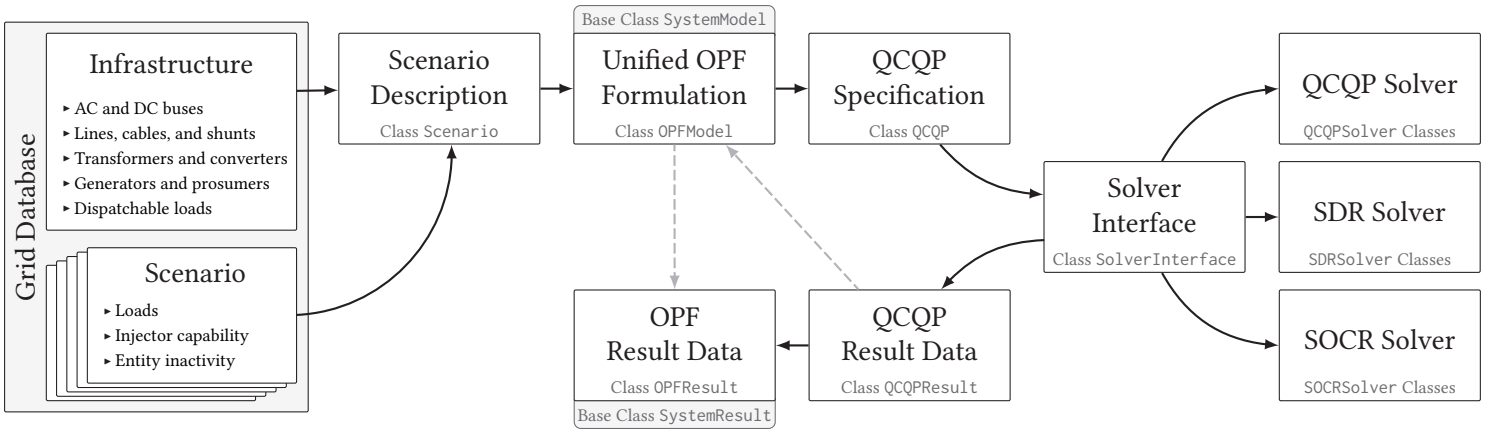

Figure 6.1: Illustration of *hynet*'s fundamental design and data flow.

6.2 Complementary Mathematical Details

In the preceding chapters, some mathematical entities are specified in an abstract form only, as it suffices for the respective discussion and results while any further characterization would impede generality. For the software implementation, however, these entities need to be characterized and parameterized in an explicit form. In the following, this explicit formulation and implementation in *hynet* is documented.

6.2.1 Injector Model

In *hynet*, the polyhedral P/Q-capability $\mathcal{S}_j \subset \mathbb{R}^2$ of injector $j \in \mathcal{I}$ is described by the intersection of up to 8 half-spaces, which can approximate the physical capabilities and restrict the power factor, see also Figure 2.3. For ease of use, a fixed nodal load or feed-in can be specified separately and need not be modeled as an injector.

The injector's convex cost function $C_j : \mathcal{S}_j \to \mathbb{R}$ is considered to be linearly separable in the active and reactive power costs, i.e.,

$$C_j(\boldsymbol{s}) = C_j^{\mathrm{p}}(\boldsymbol{e}_1^{\mathrm{T}}\boldsymbol{s}) + C_j^{\mathrm{q}}(\boldsymbol{e}_2^{\mathrm{T}}\boldsymbol{s})\,. \tag{6.1}$$

The active and reactive power cost functions $C_j^{\mathrm{p}} : \mathbb{R} \to \mathbb{R}$ and $C_j^{\mathrm{q}} : \mathbb{R} \to \mathbb{R}$ are convex PWL functions, which can approximate any convex function with arbitrary accuracy. In order to cast the OPF problem as a QCQP, the active and reactive power cost functions are included in *epigraph form* (see e.g. [42, Ch. 4.1.3]).

6.2.2 Converter Model

Similarly to injectors, the P/Q-capabilities $\hat{\mathcal{F}}_l \subset \mathbb{R}^2$ and $\check{\mathcal{F}}_l \subset \mathbb{R}^2$ of converter $l \in \mathcal{C}$ at its source and destination bus are as well specified by an intersection of up to 8 half-spaces, which offers adequate accuracy at a moderate number of constraints and parametrization effort, see also Figure 2.2.

In addition to the dynamic losses that are parameterized by the forward and backward conversion loss factor $\hat{\eta}_l \in [0, 1)$ and $\check{\eta}_l \in [0, 1)$, static (no-load) converter losses can be specified explicitly for transparency and ease of use (while the mathematical model, in contrast, includes them as fixed loads). Furthermore, any possibly occuring loss error ϑ_l in (2.35) is monitored and, if it exceeds a predefined tolerance, the converter mode is fixed according to the net active power flow to ensure a zero loss error and the computation is reissued (see also the discussion in Section 2.2.3).

6.2.3 Bus Voltage Recovery

As discussed in Section 3.2, under exactness the SDR and SOCR necessitate a rank-1 factorization or completion of the obtained optimizer $\boldsymbol{V}^\star$. In fact, as a consequence of the sparsity of the coefficient matrices as per Corollary 1, the rank-1 factorization only needs to agree on the *sparsity pattern*, i.e., under the projection $\mathscr{P}$ defined in (2.75). More generally, considering also the potential inexactness of a relaxation and the finite precision of solvers, the bus voltages $\hat{\boldsymbol{v}}^\star$ associated with an optimizer $\boldsymbol{V}^\star$ of the SDR or SOCR must thus be recovered via a *rank-1 approximation* under the projection $\mathscr{P}$.

This rank-1 approximation may be implemented using different methods and accuracy measures, which, in turn, can lead to a different impact on the accuracy of the resulting system state.[21] For this reason, *hynet* supports the integration and utilization of different rank-1 approximation methods. At this point, it includes the method for rank-1 completion in the proof of Theorem 4 (see also [129, Sec. III-B-3] and [21, Sec. IV-D]), which is a computationally highly efficient graph traversal based approximation, as well as an approximation in the least-squares sense, i.e.,

$$\hat{\boldsymbol{v}}^\star = \arg\min_{\boldsymbol{v}\in\mathbb{C}^{|\mathcal{V}|}} \left\| \mathscr{P}(\boldsymbol{v}\boldsymbol{v}^{\mathrm{H}} - \boldsymbol{V}^\star) \right\|_{\mathrm{F}}^2 . \tag{6.2}$$

The (generally nonconvex) optimization problem (6.2) is solved with a Wirtinger calculus based gradient descent method (see e.g. [152]) and Armijo's rule for step size control (see e.g. [43, Ch. 8.3]). The initial point is computed with the aforementioned graph traversal based approximation and, as a consequence of the employed step size control and termination criteria, the obtained approximation of a (local) optimizer of (6.2) is at least as accurate as the initial point in the least-squares sense.

For a solution $(\boldsymbol{V}^\star, \boldsymbol{f}^\star, \boldsymbol{s}_{\mathcal{I}}^\star)$ of the SDR or SOCR with the corresponding rank-1 approximation $\hat{\boldsymbol{v}}^\star$, *hynet* reports two different error measures, i.e., a *reconstruction error* to quantify the (numerical or inherent) inexactness of the relaxation as well as the nodal *power balance error* to quantify the impact of the rank-1 approximation on the system state accuracy. The *reconstruction error* is the mean squared error

$$\hat{\kappa}(\boldsymbol{V}^\star) = \left\| \mathscr{P}(\hat{\boldsymbol{v}}^\star(\hat{\boldsymbol{v}}^\star)^{\mathrm{H}} - \boldsymbol{V}^\star) \right\|_{\mathrm{F}}^2 / \left|\mathcal{J}\right| \tag{6.3}$$

while the (complex-valued) *power balance error* ϵ_n at bus $n \in \mathcal{V}$ is the imbalance in

[21] Note that AC subgrids typically exhibit a strong relation btw. the bus voltage angles and the active power flow as well as the bus voltage magnitudes and the reactive power flow (see e.g. [75, Ch. 10.7]).

the nodal power balance equations (2.42) for the state approximation $(\hat{\boldsymbol{v}}^\star, \boldsymbol{f}^\star, \boldsymbol{s}_\mathcal{I}^\star)$, i.e.,

$$\epsilon_n = (\hat{\boldsymbol{v}}^\star)^\mathrm{H}(\boldsymbol{P}_n + \mathbf{i}\boldsymbol{Q}_n)\hat{\boldsymbol{v}}^\star + (\boldsymbol{p}_n + \mathbf{i}\boldsymbol{q}_n)^\mathrm{T}\boldsymbol{f}^\star - \sum_{j \in \hat{\mathcal{B}}_\mathcal{I}(n)} \left([\boldsymbol{s}_j^\star]_1 + \mathbf{i}[\boldsymbol{s}_j^\star]_2\right) . \tag{6.4}$$

6.3 Additional Problem Formulations

The object-oriented design of *hynet* supports extensions to OPF-related problem formulations. It is visible in Figure 6.1 that the OPF formulation acts as a *mapping* from the scenario description to the QCQP specification, for which the base class that implements the system model in Chapter 2 offers the basic building blocks. Correspondingly, *hynet* can be extended to other problem formulations by customizing this mapping, while using and sharing its software ecosystem. Moreover, as the result representation is associated with the problem formulation, it can be adapted as well to support the result evaluation. Actually, *hynet* already includes such an extension and, as it is utilized later on, this problem formulation is briefly discussed.

6.3.1 Maximum Loadability

The *maximum loadability* is an important characteristic of a power system and, e.g., relevant in expansion planning and voltage stability assessment (cf. [76, Ch. 14]). In [153], it is shown that the maximum loadability can be identified via an optimization problem which maximizes the load increase in the system. Using the power flow equations and the collective system constraints in (3.10), the *maximum loadability problem* for hybrid AC/DC power systems can be cast as

$$\underset{\substack{\boldsymbol{s}_j \in \mathcal{S}_j,\, \boldsymbol{v} \in \mathbb{C}^{|\mathcal{V}|} \\ \boldsymbol{f} \in \mathbb{R}^{4|\mathcal{C}|},\, \theta \in \mathbb{R}_+}}{\text{maximize}} \quad \theta \quad \text{subject to} \quad (\boldsymbol{v}\boldsymbol{v}^\mathrm{H}, \boldsymbol{f}, \boldsymbol{s}_\mathcal{I}, \theta) \in \mathcal{X}_{\boldsymbol{d}} \tag{6.5}$$

in which the polyhedral set $\mathcal{X}_{\boldsymbol{d}}$ is given by

$$\mathcal{X}_{\boldsymbol{d}} = \Big\{ (\boldsymbol{V}, \boldsymbol{f}, \boldsymbol{s}_\mathcal{I}, \theta) \in \mathbb{S}^{|\mathcal{V}|} \times \mathbb{R}^{4|\mathcal{C}|} \times \mathbb{R}^2_\mathcal{I} \times \mathbb{R} : \tag{6.6a}$$

$$\operatorname{tr}(\boldsymbol{P}_n\boldsymbol{V}) + \boldsymbol{p}_n^\mathrm{T}\boldsymbol{f} = \boldsymbol{e}_1^\mathrm{T} \sum_{j \in \hat{\mathcal{B}}_\mathcal{I}(n)} \boldsymbol{s}_j - \theta \operatorname{Re}(\boldsymbol{e}_n^\mathrm{T}\boldsymbol{d}) , \quad \forall n \in \mathcal{V} \tag{6.6b}$$

$$\operatorname{tr}(\boldsymbol{Q}_n\boldsymbol{V}) + \boldsymbol{q}_n^\mathrm{T}\boldsymbol{f} = \boldsymbol{e}_2^\mathrm{T} \sum_{j \in \hat{\mathcal{B}}_\mathcal{I}(n)} \boldsymbol{s}_j - \theta \operatorname{Im}(\boldsymbol{e}_n^\mathrm{T}\boldsymbol{d}) , \quad \forall n \in \mathcal{V} \tag{6.6c}$$

$$\operatorname{tr}(\boldsymbol{C}_m\boldsymbol{V}) + \boldsymbol{c}_m^\mathrm{T}\boldsymbol{f} \leq b_m , \qquad \forall m \in \mathcal{M} \Big\} . \tag{6.6d}$$

Therein, $\boldsymbol{d} \in \mathbb{C}^{|\mathcal{V}|}$ is the direction of the *load increment*. In particular, at bus $n \in \mathcal{V}$ the quantities $\mathrm{Re}(\boldsymbol{e}_n^{\mathrm{T}}\boldsymbol{d})$ and $\mathrm{Im}(\boldsymbol{e}_n^{\mathrm{T}}\boldsymbol{d})$ specify the nodal active and reactive power load increment, respectively. In the adapted power balance equations (6.6b) and (6.6c), it can be observed that the nodal load increment is scaled by $\theta \in \mathbb{R}_+$ and imposed as an additional load. The objective of the maximum loadability problem (6.5) is the maximization of this load increase while satisfying the system constraints.

Depending on the parameterization, the optimization problem (6.5) may thus identify the maximum loadability with respect to the entire system, a specific area, or a set of buses. Furthermore, note that if the nodal load increment is set to the fixed load at the respective bus, a constant power factor is maintained.

7 Case Studies on Grid Flexibilization

This chapter presents some case studies that analyze and illustrate the utilization of the *hybrid architecture* in Chapter 5 as a guide for grid flexibilization and topology-preserving capacity expansion. The following results were computed with *hynet* v1.2.1 in Python 3.7.3. For the OPF problem, *hynet*'s solver interfaces for IPOPT [154] (v3.12.12 with MUMPS [155,156]), MOSEK [113] (v9.0.101), and CPLEX [157] (v12.9.0) were utilized for the QCQP, (chordal) SDR, and SOCR, respectively. For the maximum loadability problem, the QCQP formulation was considered and solved using *hynet*'s IPOPT solver interface.

The grid flexibilization and topology-preserving capacity expansion strategy suggested by the *hybrid architecture* is based on the conversion of existing AC lines to DC operation. Such a conversion of a line is a nontrivial process that involves comprehensive and case-specific considerations, see e.g. [121] for more details. The following case studies involve an extensive number of conversions and a detailed consideration of the individual conversion processes is not possible, not least because of the unavailability of sufficient information on the systems. For this reason, a simplified representation of the conversion process is adopted here. Specifically, the conversion of an AC line to DC operation is modeled by introducing AC/DC converter models at the line's terminals and updating the line's model parameters. In case that already some HVDC system is connected to either or both terminals of the AC line, the converted line is connected to this DC subgrid and the respective existing converters are uprated accordingly. The converters are considered as VSCs with a forward and backward loss of 1% and a Q/P capability ratio of 25%, which is rather conservative, see e.g. the brochure [11] of ABB. For simplicity, the transformer, filter, and phase reactor of a VSC station is not modeled explicitly. The update of the line model parameters considers the change from AC to DC as well as a base voltage increase by the factor $\sqrt{2}$ (cf. e.g. [69, Sec. 4.3.2]). The conversion of a transformer to DC operation constitutes its replacement by an AC/AC B2B converter model, which is considered with an analogous parameterization as above but with a forward and

backward loss of 2%.

To support the exposition hereafter, "% BCL" is defined as a percentage of the base case load of the considered system. For example, 125% BCL is a scaling of the individual loads of the base case by a factor of 1.25. Some results report the *optimality gap*, which is defined as $100 \cdot (1 - p_{\text{SDR|SOCR}}/p_{\text{QCQP}})$, where p_{QCQP}, p_{SDR}, and p_{SOCR} is the objective value of the obtained solution of the QCQP, SDR, and SOCR formulation of the OPF problem, respectively. As the relaxations provide a lower bound on the optimal objective value of the OPF problem (see Corollary 2 and Corollary 3), a small optimality gap serves as a "certificate" for the proximity of the obtained QCQP solution to the global optimum in terms of the objective. If the QCQP is solved with an interior-point method, as is the case here, this is a valuable predicate for the quality the obtained solution, which is potentially only locally optimal due to the nonconvex nature of the problem. In case that the optimality gap is not negligible, this can be due to the inexactness of the relaxation, a "poor" locally optimal solution of the QCQP, or a combination of both.

7.1 The PJM Test System

As an illustrative introductory example, the PJM 5-bus system in [158] with the adaptations in [1] is considered, which is depicted in Figure 7.1 and provided via `pjm_adapted.db` in [9]. Under cost-optimal operation, this system faces the congestion of line 4-5, due to which the generator at bus 5 with the lowest marginal cost cannot be fully utilized. Even though the generator is connected with sufficient line capacity, this underutilization occurs as only approximately half of the thermal capacity of line 1-5 can be exploited due to the congestion of line 4-5. This example illustrates the propagation of restrictions due to congested lines as discussed in Section 5.2 and, in the following, it is investigated if this congestion can be mitigated or resolved by the *hybrid architecture*.

7.1.1 Transition to the Hybrid Architecture

For the transition of an AC grid to the *hybrid architecture*, all branches outside an arbitrary spanning tree of the AC grid are converted to DC operation. It follows from *Kirchhoff's matrix tree theorem* (see e.g. [159]) that the adapted PJM system in Figure 7.1 comprises 11 spanning trees and, thus, offers eleven different options for the transition. For example, consider the conversion of AC line 3-4 and 4-5,

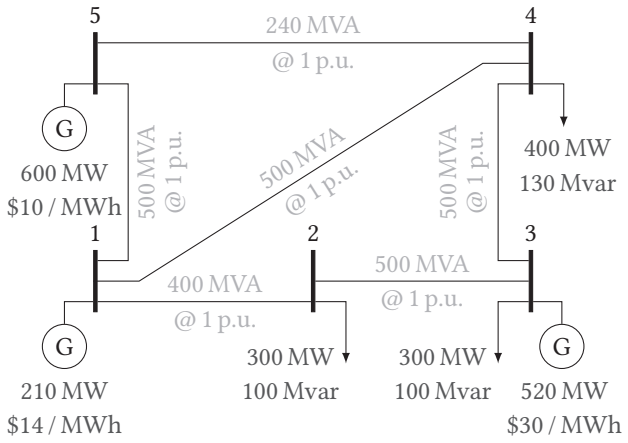

Figure 7.1: Single line diagram of the adapted PJM system [1].

which results in the hybrid PJM system depicted in Figure 7.2.[22] This hybrid system maintains the same meshed network topology as the original system, but it is now established by the interconnection of a radial AC grid and a radial MT-HVDC system. In order to focus the results on the impact of *grid flexibilization*, an uprating of the lines during the conversion is intentionally omitted such that both systems exhibit the same total line capacity. Below, an analogous transition based on the other 10 spanning trees is also considered.[23]

7.1.2 Results and Discussion

In Table 7.1, the OPF results and the maximum loadability are documented for the adapted PJM system (№ 0) as well as the eleven different implementations of the *hybrid architecture* (№ 1 to 11). All eleven hybrid PJM systems enable a significant reduction of the total injection cost, which is due to their ability to resolve the impact of the congested line and completely utilize the generator at bus 5. While all implementations of the *hybrid architecture* successfully provide a sufficient flexibilization of the grid, their performance differs slightly, primarily due to different incurred transmission losses. The SDR of the OPF problem is exact in all cases and the vanishing optimality gap certifies the global optimality of the obtained QCQP solution. The SOCR of the OPF problem is inexact for the adapted PJM system, while it is exact for all hybrid PJM systems as anticipated by the results in Chapter 5.

[22] This is a MT-HVDC variant of the hybrid system in [1] and provided via `pjm_hybrid.db` in [9].

[23] For the generation of all spanning trees, the algorithm in [160, p. 464, Algorithm S] was employed. Its implementation, as developed in the course of this dissertation, is provided open source in [161].

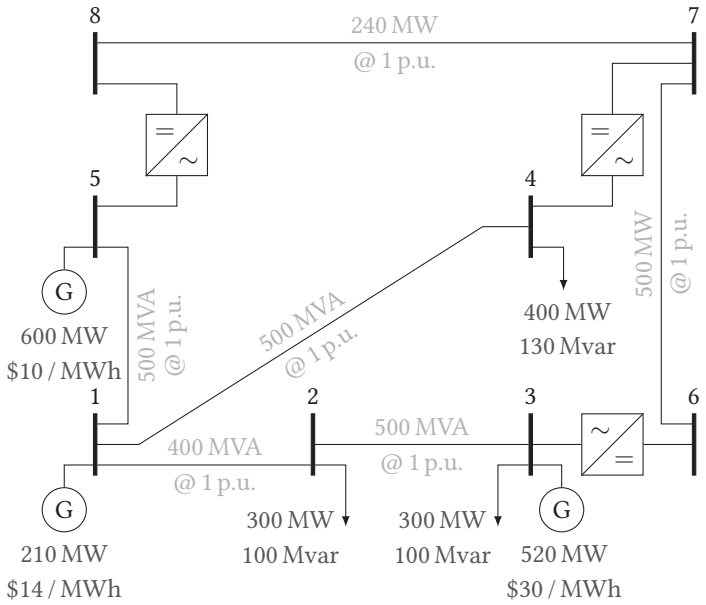

Figure 7.2: Single line diagram of an exemplary hybrid PJM system.

With respect to the maximum loadability, it can be observed that the hybrid PJM systems enable a significant increase in loadability compared to the adapted PJM system. In fact, even at their maximum loadability the hybrid PJM systems are not limited by congestion but by the available generation capacity. This is illustrated by a proportional increase of the generation capacity by 25%, where the corresponding results are documented in Table 7.2. In contrast to the limited loadability gain in the adapted PJM system, all hybrid PJM systems are capable of efficiently utilizing the additional generation capacity by virtue of their flexible power flow.

This case study illustrates that a grid flexibilization via the conversion of AC lines to DC operation as suggested by the *hybrid architecture* may significantly increase the effective transmission capacity and offer operational benefits. Moreover, it can be observed that all different implementations of the *hybrid architecture* offer similar performance advantages. This shows that there are potentially many degrees of freedom in this topology-preserving capacity expansion strategy, which can be utilized, e.g., to consider engineering-related decision factors. In the following sections, it is shown that the conclusions for this illustrative example indeed generalize to large-scale power systems.

	Converted	Inj. Cost	Reduction	Opt. Gap (%)		Rec. Error $\hat{\kappa}(\boldsymbol{V}^\star)$		Loadability	Increase
№	Lines	($/h)	(%)	SDR	SOCR	SDR	SOCR	(% BCL)	(%)
0		16 130.18	0.00	0.00	8.03	4.499e−16	2.232e−5	121.96	0.00
1	3-4, 4-5	14 929.99	7.44	0.00	0.00	3.908e−18	4.932e−19	131.99	8.22
2	2-3, 4-5	14 941.11	7.37	0.00	0.00	1.122e−19	2.163e−17	131.98	8.21
3	1-2, 4-5	15 087.57	6.46	0.00	0.00	1.627e−19	6.492e−17	131.53	7.85
4	1-4, 4-5	15 052.63	6.68	0.00	0.00	6.129e−19	4.387e−18	131.58	7.89
5	1-2, 1-4	15 092.90	6.43	0.00	0.00	1.187e−18	1.106e−17	131.49	7.81
6	1-4, 2-3	14 947.56	7.33	0.00	0.00	8.839e−21	2.643e−18	132.03	8.26
7	1-4, 3-4	14 921.24	7.49	0.00	0.00	3.040e−21	1.097e−17	131.94	8.18
8	1-4, 1-5	14 994.72	7.04	0.00	0.00	2.271e−19	8.438e−19	131.84	8.10
9	1-5, 3-4	15 033.55	6.80	0.00	0.00	3.096e−19	5.936e−18	131.74	8.02
10	1-5, 2-3	15 023.04	6.86	0.00	0.00	7.127e−19	1.598e−18	131.63	7.92
11	1-2, 1-5	14 984.16	7.10	0.00	0.00	4.264e−19	9.740e−19	131.83	8.09

Table 7.1: Comparison of the original and the hybrid PJM systems for 100% generation capacity.

	Converted	Inj. Cost	Reduction	Opt. Gap (%)		Rec. Error $\hat{\kappa}(\boldsymbol{V}^\star)$		Loadability	Increase
№	Lines	($/h)	(%)	SDR	SOCR	SDR	SOCR	(% BCL)	(%)
0		15 955.83	0.00	0.00	29.99	1.308e−17	2.147e−4	134.66	0.00
1	3-4, 4-5	11 239.67	29.56	0.00	0.00	2.301e−19	2.588e−17	164.77	22.36
2	2-3, 4-5	11 305.74	29.14	0.00	0.00	1.548e−18	1.344e−18	164.63	22.25
3	1-2, 4-5	11 439.50	28.31	0.00	0.00	7.963e−18	6.830e−17	164.21	21.95
4	1-4, 4-5	11 406.13	28.51	0.00	0.00	2.071e−17	6.979e−20	164.26	21.98
5	1-2, 1-4	11 464.52	28.15	0.00	0.00	5.613e−18	1.142e−17	164.10	21.86
6	1-4, 2-3	11 341.06	28.92	0.00	0.00	1.775e−19	6.746e−18	164.57	22.21
7	1-4, 3-4	11 261.30	29.42	0.00	0.00	3.408e−19	2.515e−18	164.63	22.25
8	1-4, 1-5	11 350.28	28.86	0.00	0.00	4.264e−19	2.402e−18	164.52	22.17
9	1-5, 3-4	11 476.08	28.08	0.00	0.00	1.991e−19	1.563e−17	164.28	21.99
10	1-5, 2-3	11 446.17	28.26	0.00	0.00	4.843e−16	4.190e−18	164.13	21.88
11	1-2, 1-5	11 347.83	28.88	0.00	0.00	3.360e−18	3.443e−18	164.46	22.13

Table 7.2: Comparison of the original and the hybrid PJM systems for 125% generation capacity.

7.2 The Polish Transmission Grid

This case study considers a model of the Polish transmission grid (400, 220, and 110 kV) during peak conditions in winter 1999/2000, which is provided by Roman Korab via `case2383wp.m` of MATPOWER [162]. It consists of 2383 buses that are interconnected by 2725 AC lines and 171 transformers. In the preparation of the model, tie lines to foreign grids were replaced by an artificial load or generator, multiple generators at a bus were aggregated, and generators that are not centrally dispatchable in the Polish energy market were given a cost of zero, see [162, `case2383wp.m`]. It was observed in [2] that two AC lines, i.e., branch 2239 and 2862, significantly limit the loadability of the system. These two lines are part of *all* spanning trees of the system and, thus, their congestion cannot be alleviated by grid flexibilization as there are no alternative power flow paths. On that account, this study considers an increase of the rating of branch 2239 and 2862 by 35%, i.e., from 9 MVA to 12.15 MVA and 68 MVA to 91.8 MVA, respectively. Furthermore, it was observed in [2] that the two parallel transformers modeled by branch 18 and 19 exhibit the same electrical parameters but a different tap ratio. For this study, the tap ratio of branch 19 is set to the tap ratio of branch 18. Additionally, the 195 lossless branches of the model are imposed with negligible losses by setting their series resistance to 10^{-6} p.u., cf. Assumption 3. This adapted model of the Polish transmission grid is provided as `case2383wp_a.db` in [9] and, in the following, it is referred to as the "reference AC grid".

The reference AC grid exhibits a maximum loadability of 106.82% BCL. The primary objective of this study is to demonstrate the potential of topology-preserving capacity expansion as suggested by the *hybrid architecture* based on *grid flexibilization* only. To this end, as in Section 7.1, an uprating of the lines and transformers during the conversion to DC operation is omitted. In addition to illustrating the impact of grid flexibilization, the obtained models are also employed to showcase and discuss the SDR and SOCR of the OPF problem for large-scale systems.

7.2.1 Capacity Expansion via Grid Flexibilization

Section 5.2 shows that the *hybrid architecture* can be interpreted as a topology-preserving capacity expansion strategy that relies on grid flexibilization. The flexibility is introduced by converting one branch in each cycle of the AC grid topology to DC operation. In other words, a spanning tree of AC branches is retained and all branches outside this spanning tree are converted. Typically, large-scale transmission grids exhibit an immense number of spanning trees due to their extensive and meshed network topology. For example, the computation of the number of

spanning trees for the reference AC grid via Kirchhoff's matrix tree theorem using NumPy [163] in Python and MATLAB [164] both results in an overflow, which implies that there are more than 10^{308} spanning trees. Hence, the first challenge in applying the *hybrid architecture* to a large-scale system is the selection of an appropriate spanning tree, as their exhaustive evaluation as in Section 7.1 is not tractable. Then, as transmission grids are in general reasonably meshed, the conversion of all branches outside the spanning tree to DC operation is typically extensive and often introduces more flexibility than required. Consequently, the second challenge constitutes the reduction of the number of conversion measures while maintaining the effective grid flexibilization to render the capacity expansion economically viable. In the following, several different transitions of the reference AC grid to a hybrid AC/DC grid are investigated based on the concepts discussed in Section 5.2.

7.2.1.1 The Hybrid Architecture

The example in Section 7.1 motivates the utilization of the degrees of freedom offered by the spanning tree selection to consider further decision factors. For example, in our work in [2] the length of an AC line is considered as a measure for its suitability for conversion, as long-distance transmission is a common application of HVDC systems [12]. More precisely, the series resistance of a branch is utilized a proxy for the line length, as the latter is not provided with the model. This suitability measure is then utilized to define a weighted graph on the system's network topology, for which the *minimum spanning tree* (MST) (see e.g. [165–167]) is identified and all branches outside the MST are considered for the conversion to DC operation.

Here, the same procedure is applied to the reference AC grid to obtain a hybrid AC/DC grid with the *hybrid architecture*, which is provided via `case2383wp_ha.db` in [9]. This hybrid grid exhibits a maximum loadability of 117.28% BCL and, thus, the grid flexibilization enables an increase in loadability by 9.8% compared to the reference AC grid. It should be highlighted that this significant increase in the effective capacity arises *exclusively* from the introduced flexibility in power flow, as the branch capacity is not uprated during conversion. While this capacity gain is remarkable, so is the number of conversions: For this hybrid grid, 488 AC lines and 16 transformers are converted to DC operation. Therefore, an actual transition of the considered system to the *hybrid architecture* is probably not appropriate, but it serves as a valuable indicator for the potential of grid flexibilization and as a point of departure for identifying effective flexibilization measures. In the following, the approaches to the latter as proposed in Section 5.2.1 and Section 5.2.2 are explored.

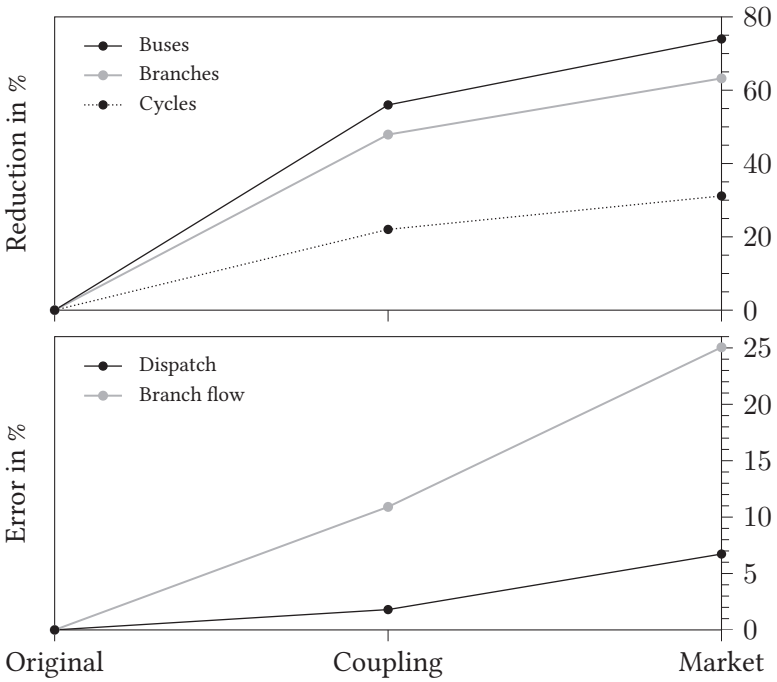

Figure 7.3: Feature- and structure-preserving network reduction of the Polish system.

7.2.1.2 Focusing with Network Reduction

Section 5.2.1 motivates the use of network reduction as a means to focus the *hybrid architecture* and its induced grid flexibilization to the critical parts of a system. In the context of (optimal) power flow, the objective of network reduction is to reduce the system model to those parts that are essential to an adequate modeling of the power flow in the system. Accordingly, the application of the *hybrid architecture* to the reduced model focuses its structural requirements to these parts.

This study utilizes the feature- and structure-preserving network reduction method in [7] (see also Section 5.2.1), for which an open-source implementation is provided with *hynet* [3]. Typically, the network reduction targets a decrease in the number of buses and branches to reduce the computational effort associated with studies based on the reduced model. However, for a focusing of the *hybrid architecture*, the reduction of the number of *cycles* in the network topology of the reduced model is the primary objective as it translates to a reduction of the conversion measures. To this end, a reduction based on the electrical coupling and market based subgrid selection of [7] with $\tau = 0.05$ and $\delta = 3$ is applied under consideration

of the standard features [7, Sec. III] (with "highly loaded" referring to a utilization of 90% or more of the branch rating). The topology-based subgrid selection and heuristic feature refinement in [7] are ineffective for the reduction of cycles in this model and, for this reason, are not utilized. The result of the reduction is depicted in Figure 7.3, which shows that the number of cycles is reduced considerably at a moderate dispatch and branch flow deviation.

For the reduced system model, a spanning tree is selected using the same procedure as in Section 7.2.1.1 above and all AC branches outside the spanning tree are considered for the conversion to DC operation. These conversion measures, which target 370 AC lines and 9 transformers, are then applied to the reference AC grid to obtain the hybrid AC/DC grid with a network reduction focused *hybrid architecture* (NR-focused HA) that is provided via `case2383wp_hr.db` in [9].[24] This hybrid grid exhibits a maximum loadability of 117.22% BCL and, thus, achieves essentially the same loadability gain as the hybrid AC/DC grid with the full *hybrid architecture*. It confirms the intuition that a grid flexibilization is only effective in the parts of the system that prominently shape or restrict the power flow, as they are retained during network reduction due to their impact on the dispatch and branch flow.

Although the number of converted AC lines and transformers is significantly reduced by this focusing technique, it is still extensive. A direct conclusion may be that a more rigorous network reduction should be applied to further reduce the number of cycles in the reduced model and, therewith, the number of conversion measures. However, in our experience with this network reduction method, we observed that beyond a certain amount of reduction the ability of the reduced model to adequately describe the power flow deteriorates very rapidly. As this quality deteriorates, the selection of conversion measures via this approach potentially becomes increasingly arbitrary and, thus, inappropriate. Therefore, to further distill the structural implications of the *hybrid architecture* for grid flexibilization, a more direct and granular approach is required, which is the subject of the following section.

7.2.1.3 Focusing with Measure Selection

As motivated and discussed in Section 5.2.2, a direct evaluation of the benefit attained by the individual conversion measures suggested by the *hybrid architecture* may enable a more targeted selection of effective flexibilization measures. Here, the joint impact of an increasing number of conversion measures selected from the

[24] Additionally, the corresponding reduced model is provided via `case2383wp_hr_nr.db` in [9]. By virtue of this particular focusing, the reduced model exhibits the *hybrid architecture*, cf. Section 5.2.1.

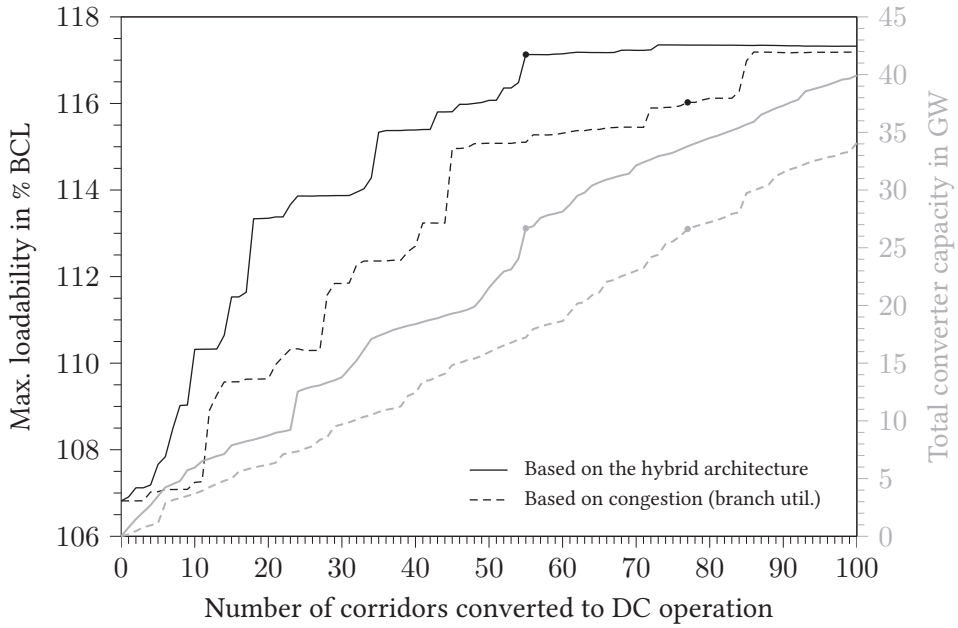

Figure 7.4: Max. loadability (black) and converter capacity (gray) w.r.t. conversions.

hybrid architecture is evaluated. As the number of all possible subsets of conversion measures is vast, the conversion measures are ranked to simplify the evaluation to the analysis of an increasing number of top-ranked conversion measures. To this end, consider the hybrid AC/DC grid with the *hybrid architecture* in Section 7.2.1.1 again and, for simplicity, assume that the utilization of an HVDC system indicates its benefit for flexibilization. Then, the ranking is induced by the utilization of a DC line, which is determined via an OPF computation. The association of this ranking with the respective AC lines in the reference AC grid results in a ranking of the conversion measures, which, for the sake of simplicity, excludes transformers. In case of parallel lines, this work considers their joint conversion to DC operation. For this reason, the conversion of an increasing number of transmission *corridors* based on the top-ranked conversion measures is considered, which is illustrated in Figure 7.4.

In Figure 7.4, it can be observed that even a small number of conversion measures selected from the *hybrid architecture* can offer a significant capacity gain with respect to the reference AC grid. Furthermore, approximately the same loadability as the full *hybrid architecture* is achieved with the conversion of only 55 AC lines (in 55 corridors), which yields a maximum loadability of 117.13% BCL. This exemplary hybrid AC/DC grid is provided via `case2383wp_ha55.db` in [9] and considered later on.

The plateaus in Figure 7.4 reveal that this straightforward approach has room for improvement, as several conversion measures do not directly induce a capacity gain. In fact, once this perspective on capacity expansion with the *hybrid architecture* is adopted, many different methods may be devised. The purpose of this simple ranking-based measure selection scheme is, on one hand, to show that the *hybrid architecture* can serve as a valuable guide for grid flexibilization. On the other hand, it enables the direct comparison to an analogous scheme that neglects the impact on the AC grid topology, which is discussed below.

7.2.1.4 Congestion-Based Grid Flexibilization

The previous examples illustrate that the *hybrid architecture* can guide to effective grid flexibilization measures for capacity expansion. It proposes the systematic conversion of AC branches to DC operation to introduce flexibility, where each conversion resolves a cycle in the AC grid topology. The expedience of the latter, i.e., the flexibilization of cycles, is motivated in Section 5.2. To demonstrate that this systematic flexibilization of cycles can indeed be advantageous, the previous measure selection is contrasted by an analogous scheme that neglects the impact on the AC grid topology. To this end, the same ranking-based measure selection scheme as above is adopted and the ranking is again defined by the branch utilization, but in this case considering the AC line utilization in an OPF of the reference AC grid. It follows the rationale that highly loaded branches potentially congest under an increasing load and, therefore, may benefit from the controllability attained by a conversion to DC operation.

The efficacy of the thereby identified conversion measures is depicted in Figure 7.4. It can be observed that the induced grid flexibilization is less effective compared to the measure selection with the *hybrid architecture*. For example, the *hybrid architecture* based measure selection attains approximately the same flexibilization as the full *hybrid architecture* with the conversion of 55 AC lines. At the same total converter capacity, the congestion based measure selection proposes the conversion of 78 AC lines (in 77 corridors), but only achieves a maximum loadability of 116.02% BCL. For a further comparison, this exemplary hybrid AC/DC grid is also considered below and provided via `case2383wp_hc77.db` in [9].

7.2.2 Evaluation of the Optimal Power Flow

In the grid flexibilization discussed above, the focus is put on the maximum loadability as a means to quantify the gain in effective transmission capacity. This is

complemented in this section with a discussion of the impact of the flexibilization on a cost-optimal operation based on the OPF. Additionally, the solutions to the SDR and SOCR of the OPF problem are presented to showcase the impact of the conversions on the exactness of the relaxations. In order to study the systems under different load levels, the typical range reported in [168, Tab. 4] is considered, which starts at 56% BCL and is extended here up to the maximum loadability of the respective system. Within this range, the QCQP, SDR, and SOCR OPF is computed for all load levels in steps of 0.5% BCL. The respective results are documented in Figure 7.5a to Figure 7.9a.

In Figure 7.5a, it can be observed that effective congestion is reflected by a relative increase of the injection costs. This is most pronounced for the reference AC grid, which exhibits a rapid increase and, shortly afterwards, reaches the loadability limit as the congestion prevents the system from further utilizing the available generation capacity. The more flexibility is introduced, this effect is mitigated and eventually vanishes for the *hybrid architecture*. In this regard, two notable observations can be made. First, the network reduction focused *hybrid architecture* exhibits an equally thorough flexibilization as the full *hybrid architecture*, confirming the adequacy to condense the structural transformation to critical parts of the system. Second, the 77 congestion-based conversions that neglect the impact on the AC grid topology introduce flexibility at more locations in the system compared to the 55 *hybrid architecture* based conversions, but still the latter are more effective in the flexibilization of the power flow. In those cases where none of systems faces congestion, all perform essentially equally well, with the reference AC grid being slightly more efficient than the hybrid AC/DC grids due to lower transmission losses.

In Figure 7.6a, it can be observed that the SDR of the OPF problem is consistently exact for the *hybrid architecture* as anticipated by the results in Chapter 5.[25] For the other systems, the reconstruction error increases the further they depart structurally from the *hybrid architecture* and the less grid flexibilization they provide. A qualitatively similar observation can be made for the corresponding optimality gap in Figure 7.7a, which is consistently zero for the *hybrid architecture* and increases for the other systems. The fluctuations with respect to the different load levels, which could indicate a scenario dependency, are presumably artefacts of the solver. This is suggested by the respective results for the SOCR of the OPF problem in Figure 7.8a and Figure 7.9a, where the optimality gap for the network reduction focused *hybrid*

[25] The consistent exactness under the *hybrid architecture* in Figure 7.6 and Figure 7.8 indicates that pathological price profiles are indeed unlikely. To not depart too much from this chapter's main topic, the discussion of LMPs is omitted here and the interested reader is kindly referred to our work in [2].

architecture is consistently zero. Besides, the results show a similar but more pronounced tendency as for the SDR, as the SOCR is a further relaxation of the SDR. Notably, for the *hybrid architecture* the SOCR is consistently exact and the optimality gap is zero throughout.

Turning back the attention to the capacity gain, it shall be noted that the *hybrid architecture* provides such a thorough flexibilization that the maximum loadability is not determined by congestion but by the available generation capacity. In order to illustrate its further potential, the generation capacity is increased proportionally by 25%. Then, the reference AC grid exhibits a maximum loadability of 117.05% BCL, while the *hybrid architecture* achieves the remarkable maximum loadability of 143.78% BCL. This substantial capacity gain is also offered by the network reduction focused *hybrid architecture*, which attains a maximum loadability of 143.58% BCL. The hybrid AC/DC grid with 55 *hybrid architecture* based conversions achieves a maximum loadability of 126.26% BCL and the one with 77 congestion-based conversions 119.22% BCL. Thus, also in this setting the conversions guided by the *hybrid architecture* offer a more effective flexibilization. The respective OPF results are shown in Figure 7.5b to Figure 7.9b, which demonstrate that the qualitative characteristics identified above still apply after such a generation capacity expansion.

In conclusion, this case study shows that the insights from the small-scale example in Section 7.1 indeed generalize to large-scale systems. The grid flexibilization with the *hybrid architecture* induces a substantial gain in the effective transmission capacity and the flexible power flow avoids restrictive congestion. Besides, the study makes evident that the focusing of the *hybrid architecture* is inevitable for large-scale systems to arrive at an adequate number of conversions. Here, the network reduction based focusing of the *hybrid architecture* successfully reduces the number of conversions without any significant concessions to the grid flexibilization, but it still necessitates an extensive number of conversion measures. By selecting conversion measures based on the *hybrid architecture*, it is possible to arrive at an adequate trade-off between the number of conversions and the attained grid flexibilization. The results show that a small fraction of the measures can already suffice and, in comparison to an analogous selection scheme that neglects the impact on the network topology, they emphasize the benefit of resolving cycles in the AC grid topology.

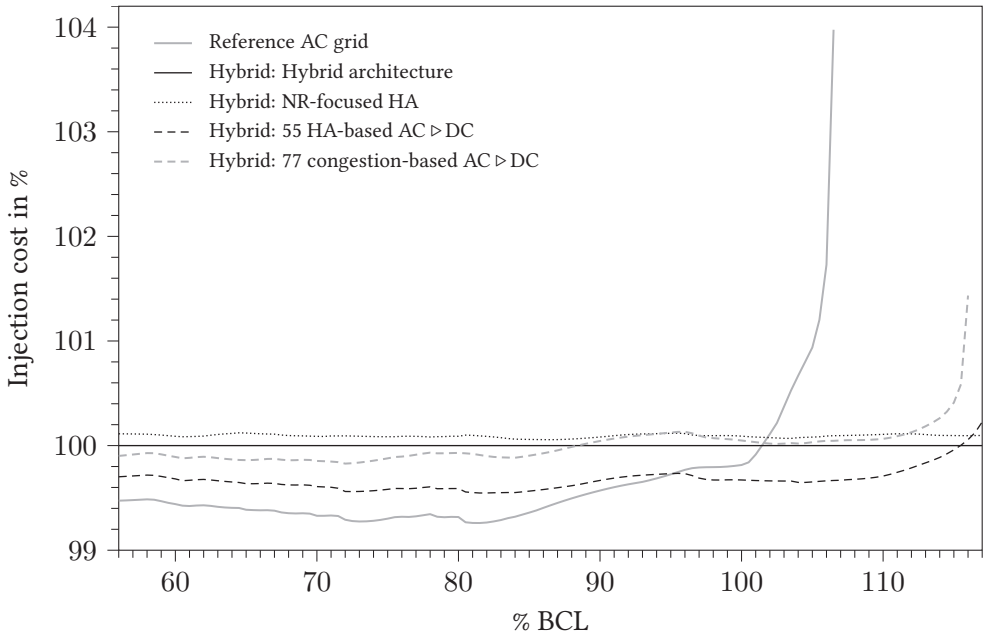

(a) 100% generation capacity.

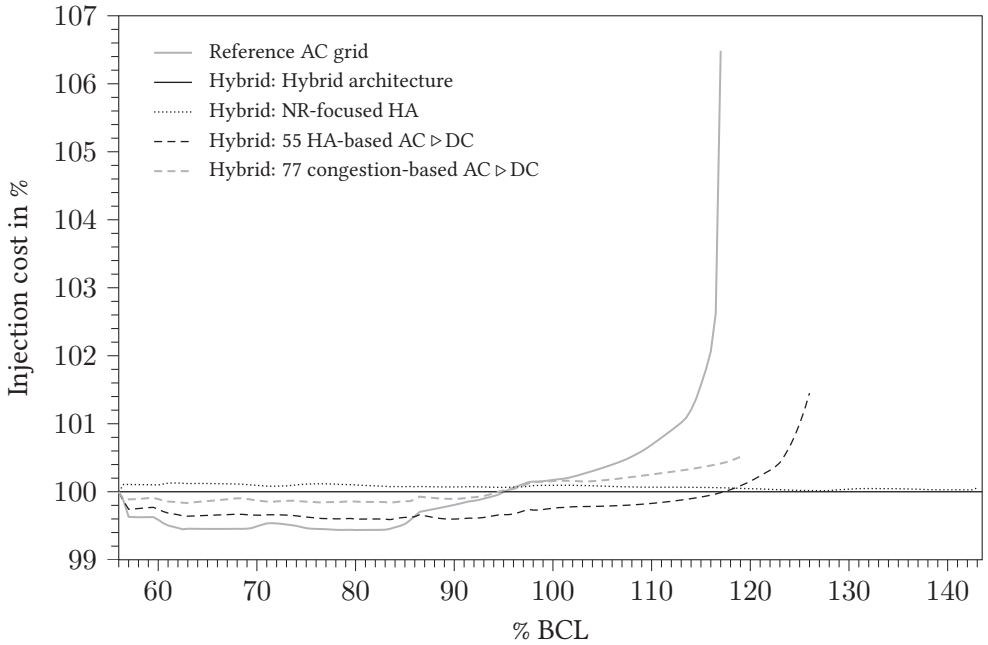

(b) 125% generation capacity.

Figure 7.5: Relative total injection cost with respect to the *hybrid architecture*.

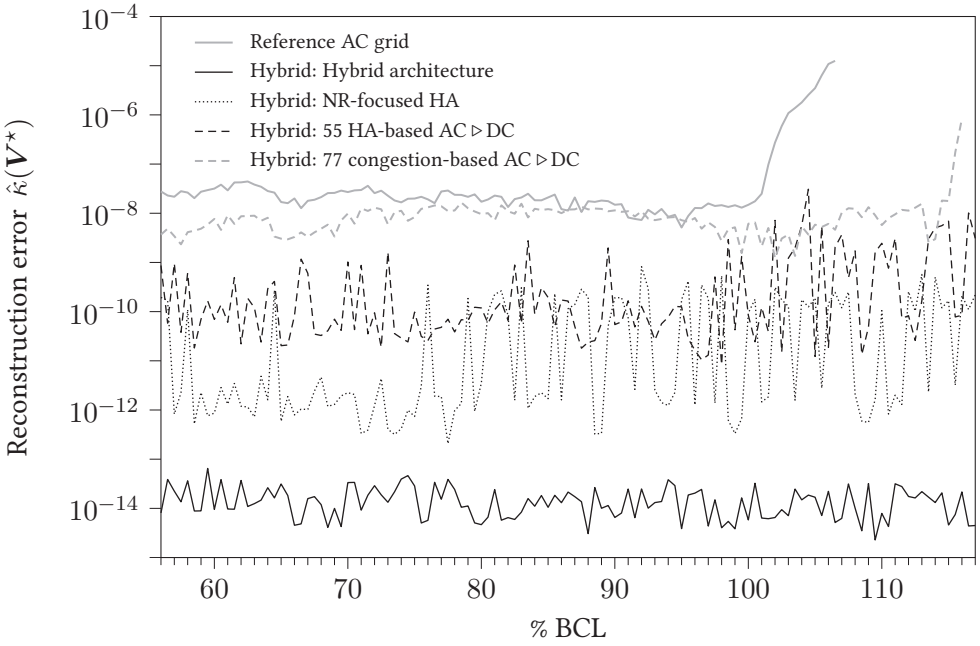

(a) 100% generation capacity.

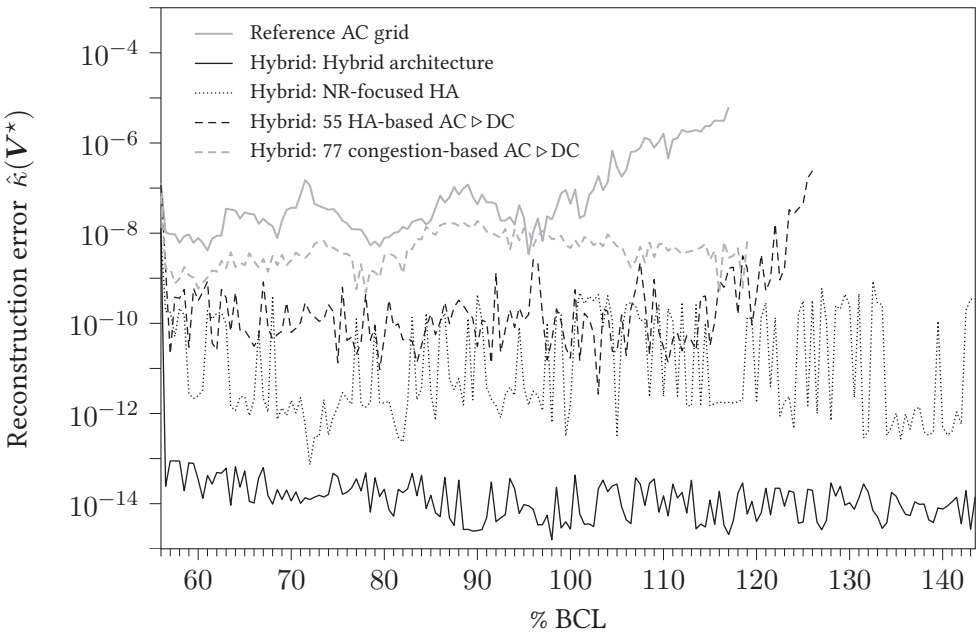

(b) 125% generation capacity.

Figure 7.6: Reconstruction error $\hat{\kappa}(\boldsymbol{V}^\star)$ of the SDR for different load levels.

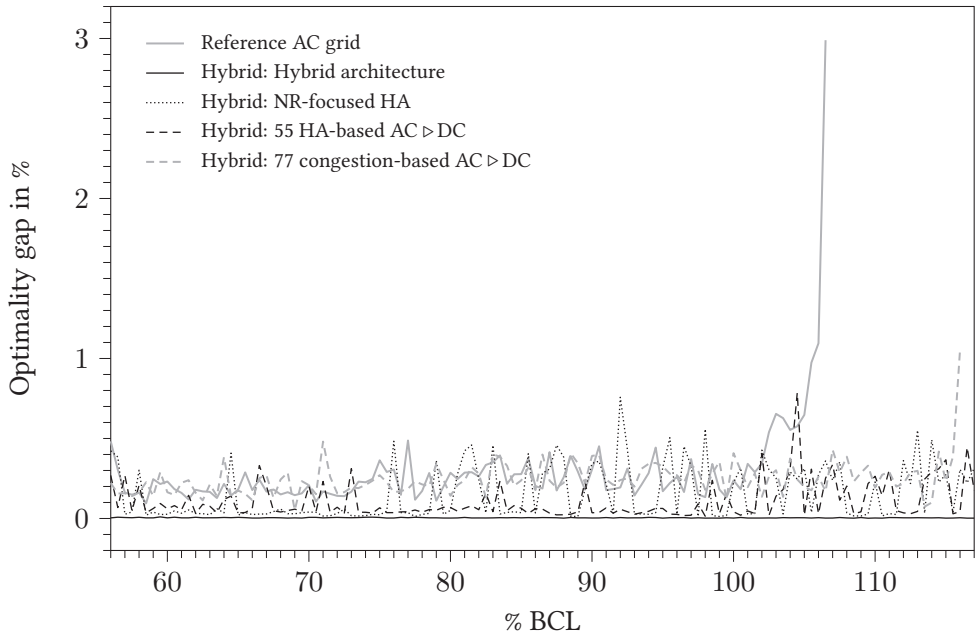

(a) 100% generation capacity.

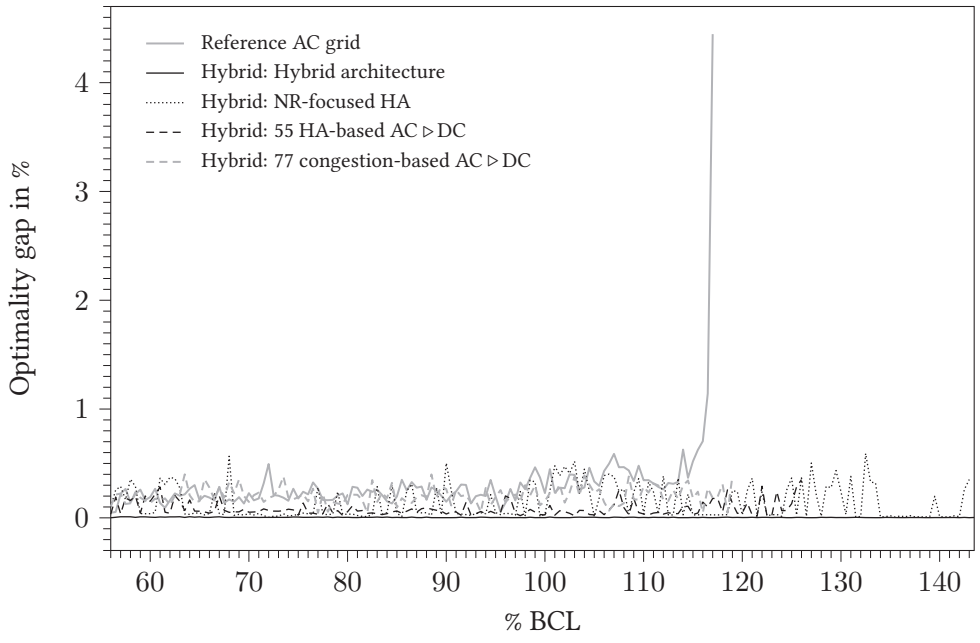

(b) 125% generation capacity.

Figure 7.7: Optimality gap with respect to the SDR for different load levels.

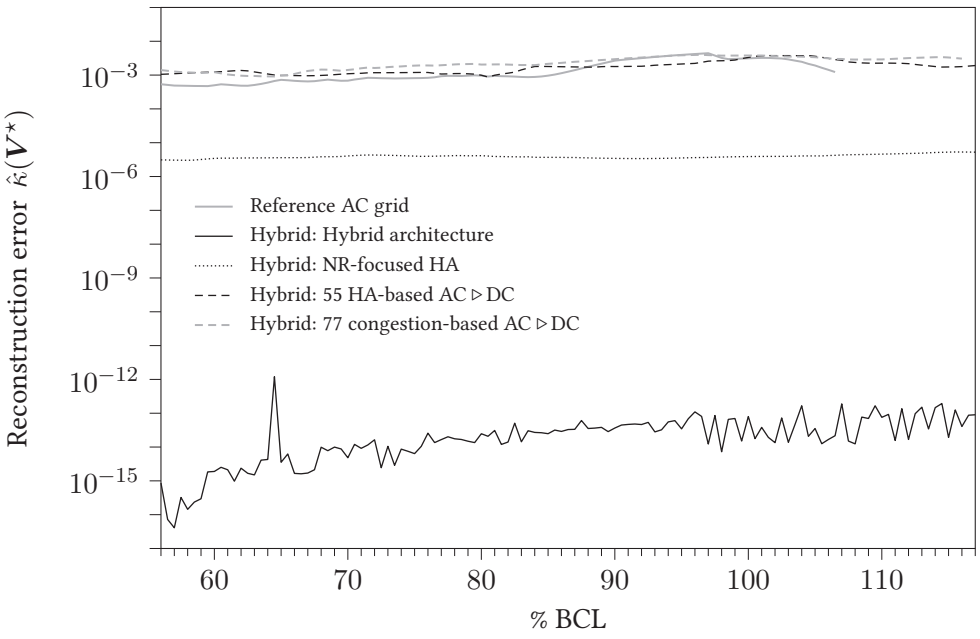

(a) 100% generation capacity.

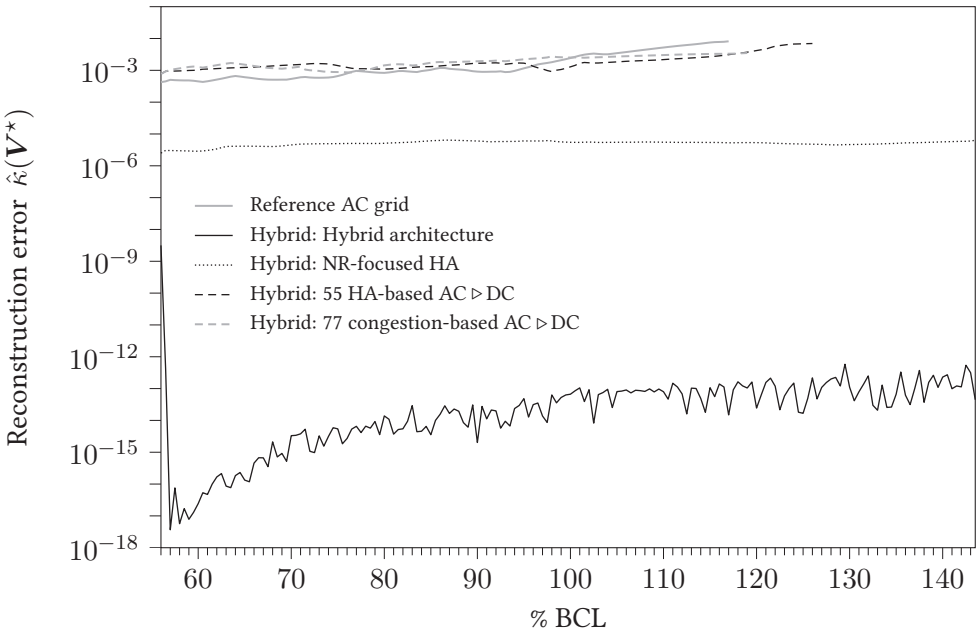

(b) 125% generation capacity.

Figure 7.8: Reconstruction error $\hat{\kappa}(\boldsymbol{V}^\star)$ of the SOCR for different load levels.

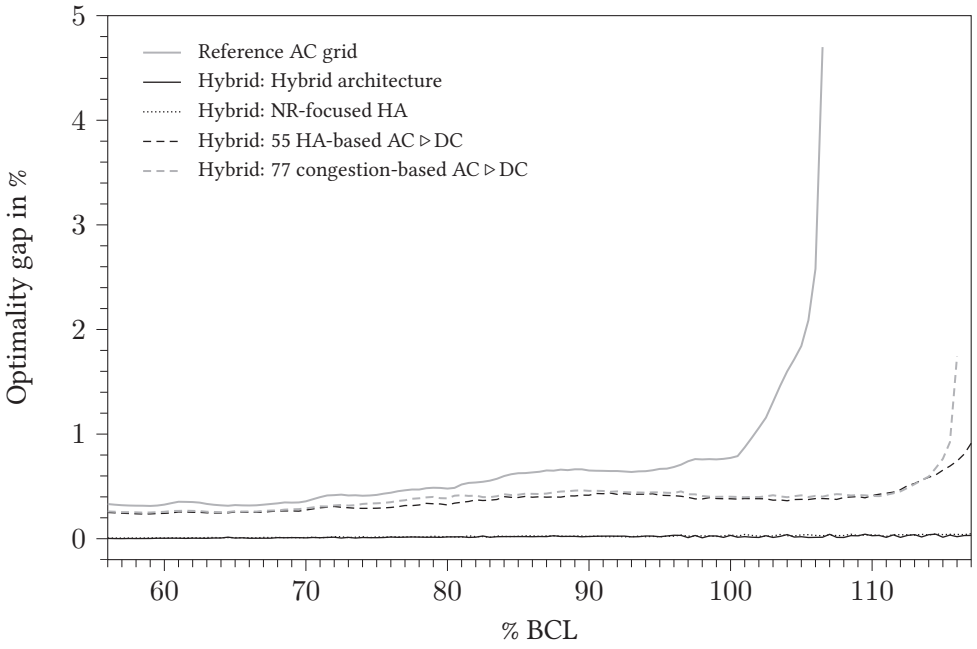

(a) 100% generation capacity.

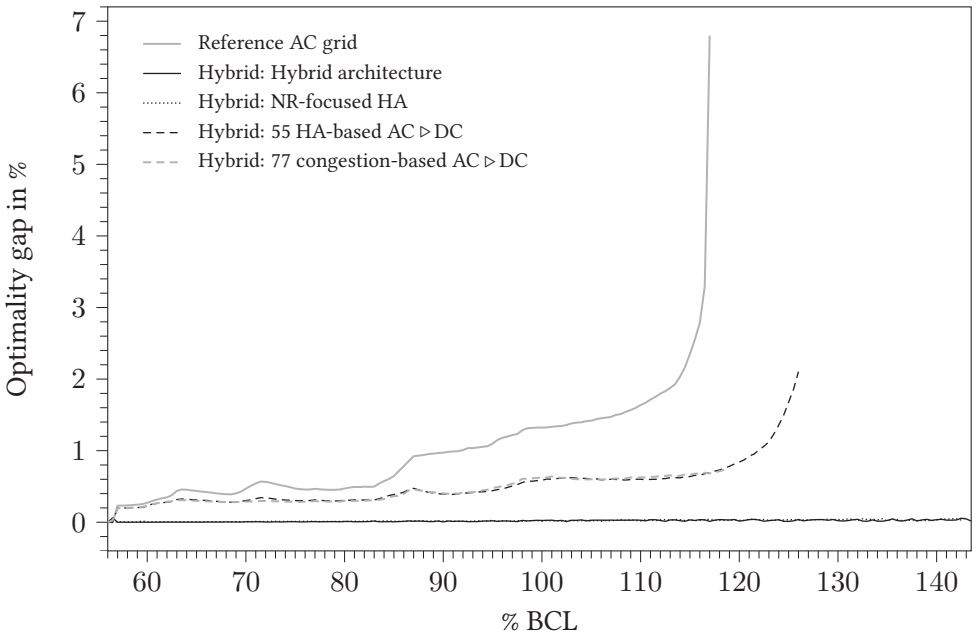

(b) 125% generation capacity.

Figure 7.9: Optimality gap with respect to the SOCR for different load levels.

7.3 The German Transmission Grid

The previous case studies demonstrate the potential of grid flexibilization with the *hybrid architecture* by analyzing its impact on the effective transmission capacity based on the maximum loadability. This case study turns the attention to a specific setting that actually necessitates additional transmission capacity and investigates the potential of the *hybrid architecture* to propose effective topology-preserving capacity expansion measures. To this end, the German transmission grid is considered, which currently faces extensive challenges due to a process of change known as the *energy transition*.

The energy transition is a reorientation of the energy policy toward RES and the reduction of greenhouse gas emissions. In the electricity sector, this reorientation introduces an increasingly distributed and fluctuating energy production due to the growing use of wind, sun, and biomass as energy sources. These changes in the energy mix also entail a geographic shift of power generation, inducing a growing energy surplus in the north and an energy demand in the south of the country [119, 169]. This transformation of the generation structure renders the expansion of the German transmission grid a key issue of the energy transition [70, 119, 169]. Adequate expansion measures are determined via a multi-stage process, which is repeated iteratively since the year 2012 [70]. In this process, the TSOs propose projected future scenarios and corresponding network development plans, which are screened, verified, and confirmed by the *Bundesnetzagentur* (BNetzA) before specific measures are planned in subsequent stages. Throughout, the proposed measures are repeatedly subject to consultation and public debate to ensure validity and acceptance [70, 71].

The network development plan, i.e., the *Netzentwicklungsplan Strom* (NEP) [170], is based on projections for the year 2030 and identifies several new HVDC transmission lines as a necessary countermeasure for the north-south generation imbalance. While these HVDC lines provide a transmission backbone for the energy transition, they also constitute a primary subject of objection. For example, during consultation of the NEP in 2015 more than $34\,000$ statements were received [70]. Their statistical evaluation shows that the major concerns relate to the impact on humans, the capital loss of real estate, and the impact on the landscape [70]. These objections can be attributed primarily to the implementation of new transmission corridors, where the majority is due to the north-south HVDC lines. Even though the expansion planning follows the so-called *NOVA principle* [119, 169], i.e., grid optimization and reinforcement is preferred to additional transmission lines, these HVDC lines are identified as necessary measures.

The following case study investigates if the conversion of AC lines and transformers to DC operation based on the *hybrid architecture* can outline a possible alternative to these new HVDC lines and, therewith, may identify an opportunity to avoid the necessity of new transmission corridors. To this end, an appropriate model of the German transmission grid is required. Unfortunately, the models employed in [169, 170] are published in a limited form only. On that account, the model presented in [171] is adopted here, which was kindly provided by the Professorship for Power Transmission Systems at TUM. Based on publicly available data, it models the German transmission grid (380 and 220 kV) in 2015 as well as the expansion measures of the NEP in [169] as accurately as possible. In the preparation of this model, tie lines to foreign grids were replaced by an artificial load or generator. Furthermore, the model includes exemplary scenarios for two weeks in the projected year 2030 with hourly resolution. Analogous to [169], the RES generation based on wind and *photovoltaics* (PV) is considered with zero marginal cost. This projected model of the German transmission grid in 2030, which is referred to as the "NEP" in the remainder, is provided via `germany2030nep.db` in [9]. Figure 7.11a on page 107 visualizes the NEP, which shows its AC lines (gray) and the new HVDC transmission lines (black). This figure was kindly rendered by Dominic Hewes of the Professorship for Power Transmission Systems at TUM.

7.3.1 Topology-Preserving Capacity Expansion

To explore alternatives to the new HVDC lines in the NEP, these are removed from the model. This reduced model is then considered at the peak load of the projected year 2030, where it experiences pronounced congestion, in order to analyze topology-preserving capacity expansion measures based on the *hybrid architecture*. Considering the conclusions of the previous case study in Section 7.2.1, a ranking-based measure selection is pursued to identify an adequate trade-off between the number of conversions and the attained capacity gain. To account for the pronounced congestion, the suitability for conversion is defined by the branch utilization, which is determined with an OPF. The structural guideline of the *hybrid architecture* for grid flexibilization is then incorporated by defining a weighted graph on the network topology using this suitability measure. For this weighted graph, the MST is identified and all branches outside the MST are considered as candidates for the conversion to DC operation. Therewith, the most prominently congested or utilized branches are identified that, if converted, additionally resolve a cycle in the AC grid topology. These candidates are ranked by their branch utilization and, on this basis,

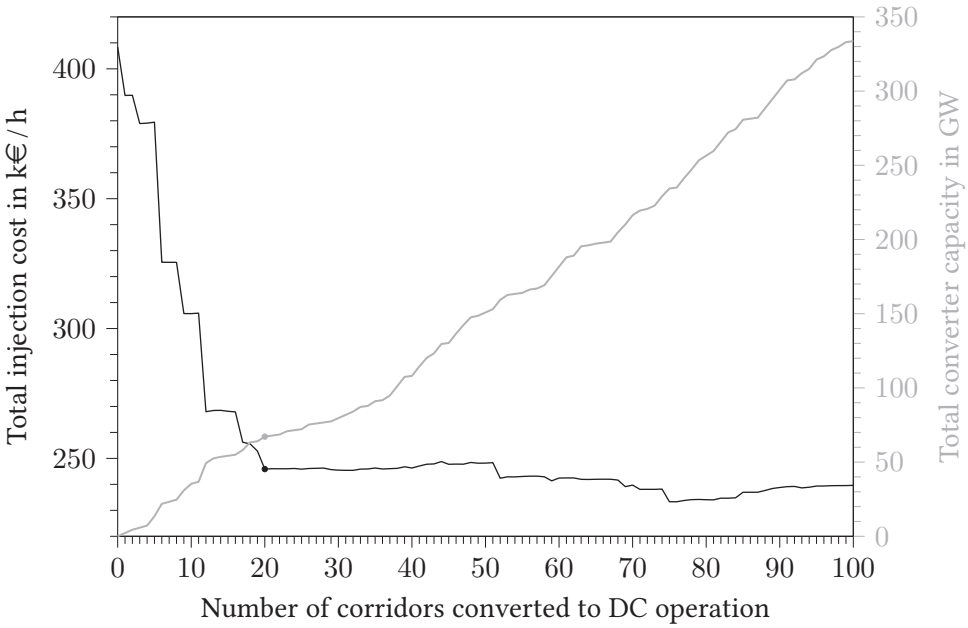

Figure 7.10: Injection cost (black) and converter capacity (gray) w.r.t. conversions.

the conversion of an increasing number of top-ranked candidates is evaluated. Unlike the previous studies, which focus on grid flexibilization only, this study utilizes the conversion to DC operation for an uprating by a factor of two (cf. e.g. [122]) if the utilization of a branch exceeds 95% to relieve congested connections. In case of parallel lines or transformers, their joint conversion to DC operation is considered. The evaluation is illustrated in Figure 7.10, where, for simplicity, the term "corridor" refers to the connection of two different buses of the system that may consist of lines or transformers.

At the peak load, the OPF of the NEP exhibits a total injection cost of 265.8 k€/h. If the new HVDC lines are removed from the NEP, the total injection cost increases to 408.4 k€/h, as the congestion necessitates the increased utilization of conventional generation resources. Figure 7.10 shows that the conversion of 20 "corridors" or, more precisely, 12 AC lines and 8 transformers to DC operation can effectively resolve the congestion in this scenario and reduce the total injection cost down to 245.9 k€/h. In the conversion process, which involves the installation of a total of 67.2 GW of converter capacity, 7 of the 12 AC lines and 5 of the 8 transformers are uprated. This hybrid AC/DC grid with topology-preserving capacity expansion measures based on the *hybrid architecture* is further analyzed below, where it is referred to as the "hybrid

grid". It is is provided via `germany2030ha20.db` in [9] and depicted in Figure 7.11b on page 107, which shows the AC lines (gray), the AC lines that were converted to DC operation (black), as well as the transformers that were replaced by a B2B converter (black dot). This figure was kindly rendered by Dominic Hewes of the Professorship for Power Transmission Systems at TUM.

7.3.2 Evaluation and Discussion

The topology-preserving capacity expansion measures to obtain the hybrid grid are selected on the basis of the *hybrid architecture*, the branch utilization under the peak load, and their impact on the performance under the peak load. Besides the structural guideline provided by the *hybrid architecture*, the decision making thus relies on the peak load scenario, which raises the question whether the implemented conversion measures can offer an adequate capacity gain under other scenarios. To investigate this, two exemplary weeks of the projected year 2030 are considered, which include the extreme cases of the year's maximum and minimum load. The total load and RES capacity in these two weeks is shown in Figure 7.12a and Figure 7.14a (page 108 and 110) with an hourly resolution. For these scenarios, the OPFs are computed for the NEP, the hybrid grid, and the NEP without the new HVDC lines. The latter is included to demonstrate the impact of insufficient transmission capacity between the north and the south of the country.

Figure 7.12b and Figure 7.14b depict the hourly total injection cost for both weeks.[26] It can be observed that the hybrid grid can indeed consistently provide adequate transmission capacity to attain the same performance as the NEP. This is particularly visible in the hours of high RES availability, where Figure 7.12c and Figure 7.14c show that the hybrid grid can efficiently utilize the RES. In contrast, the NEP without the new HVDC lines fails to offer sufficient transmission capacity, which is reflected by a considerable curtailment of the RES-based generation and, consequently, an increase of the total injection cost.

Figure 7.13b and Figure 7.15b depict the average branch utilization for both weeks. It can be observed that in the hours of high RES availability the average branch utilization in the hybrid grid increases compared to the NEP. This illustrates that the grid flexibilization induced by the selective conversion of AC branches to DC operation enables an improved utilization of the existing infrastructure, facilitating the increase in effective transmission capacity. As a consequence to the superior

[26] The models do not consider the European power exchange market and, thus, the RES are curtailed in case that the RES capacity exceeds the total load. As the generation based on RES is considered with zero marginal costs (cf. [169, Sec. 2.2]), the total injection cost is zero if the load is served by RES only.

utilization due to the grid's improved power routing capability, the power may flow along electrically longer transmission paths and, thereby, incur higher transmission losses. The transmission losses are shown in Figure 7.13c and Figure 7.15c, where it can be observed that the branch losses as well as the total losses that include the converter losses are slightly higher for the hybrid grid.

Concluding, this case study shows that a topology-preserving capacity expansion with the selective conversion of AC branches to DC operation based on the *hybrid architecture* may offer a viable alternative to the construction of new transmission corridors. In the considered setting, the uprating during the conversion in conjunction with the induced grid flexibilization can successfully provide an adequate increase in the effective transmission capacity. As a trade-off for the improved utilization of the infrastructure, the transmission losses increase slightly due to both the converter losses and electrically longer transmission paths. However, in the light of the significant advantages arising from the avoidance of extensive new transmission corridors, this drawback may be considered as minor.

Finally, it should be emphasized that the presented results should not be interpreted as a direct proposal of specific capacity expansion measures for the German transmission system, but rather as a tangible example for the potential of a topology-preserving capacity expansion based on the *hybrid architecture*. For the proposal of specific expansion measures, a significantly more elaborate analysis, validation, and verification is necessary, including a technical feasibility study for the conversions, a comprehensive validation in different projected scenarios, and a thorough resilience (e.g., N-1 security) analysis. This is not only far beyond the scope of this work, but also beyond its purpose – that is, to illustrate the potential of a systematic conversion of existing AC branches to DC operation for capacity expansion and, therewith, to motivate its consideration by system planners.

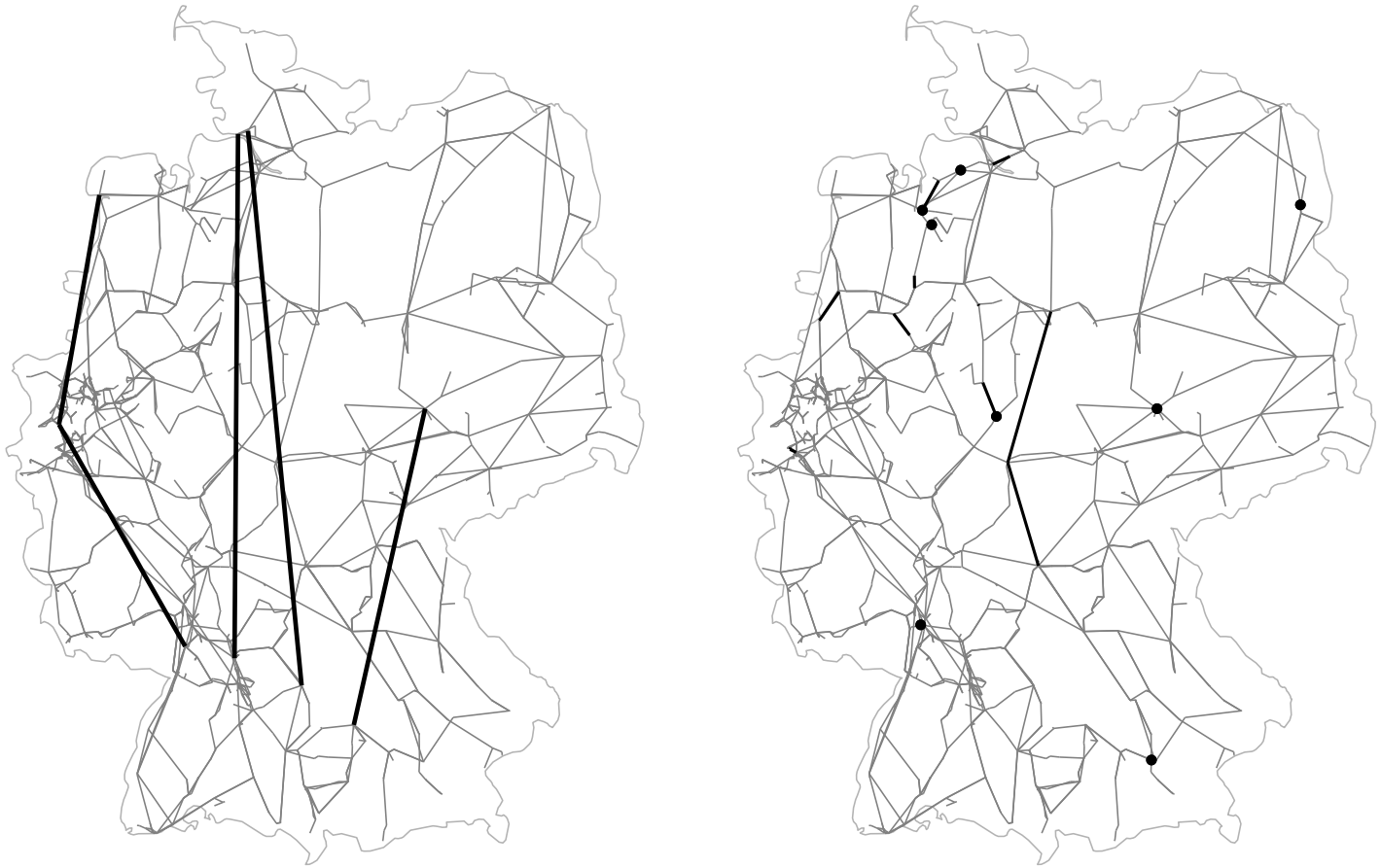

(a) NEP

(b) Topology-preserving capacity expansion

Figure 7.11: Illustration of the NEP with new HVDC lines and the hybrid grid with topology-preserving expansion measures.

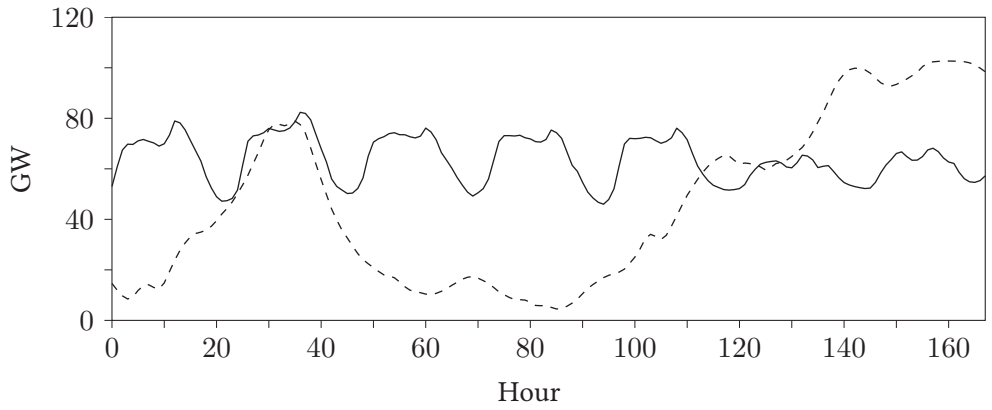

(a) Total load (solid) and RES capacity (dashed).

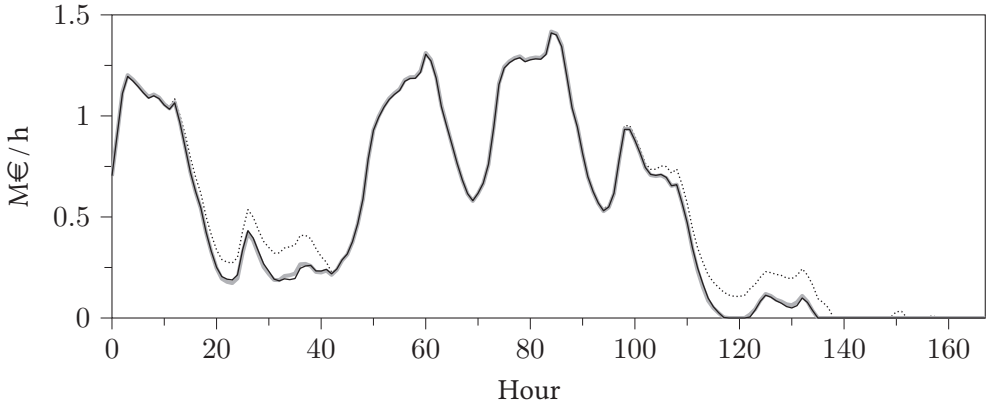

(b) Total injection cost of the NEP (gray), hybrid grid (black), and NEP w/o HVDC (dotted).

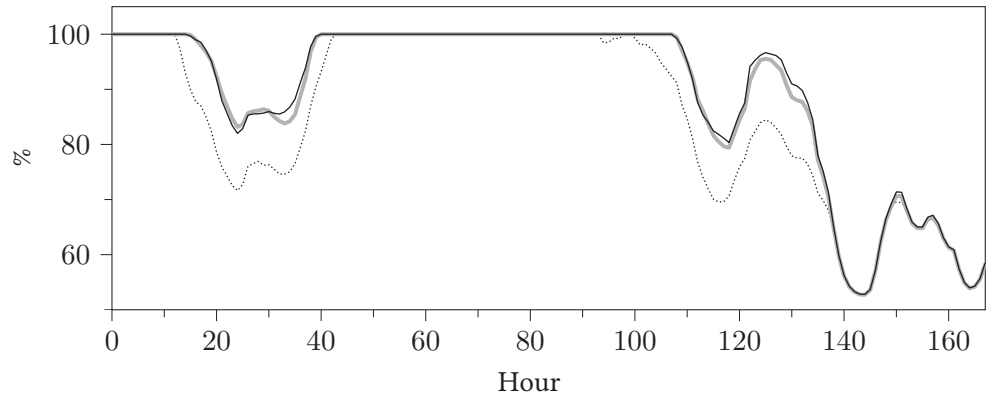

(c) RES utilization of the NEP (gray), hybrid grid (black), and NEP w/o HVDC (dotted).

Figure 7.12: Injection cost and RES utilization in the week with year's maximum load.

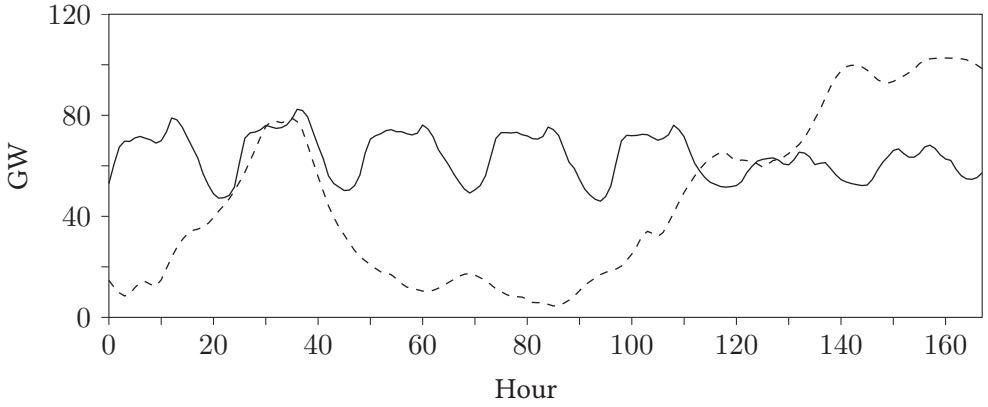

(a) Total load (solid) and RES capacity (dashed).

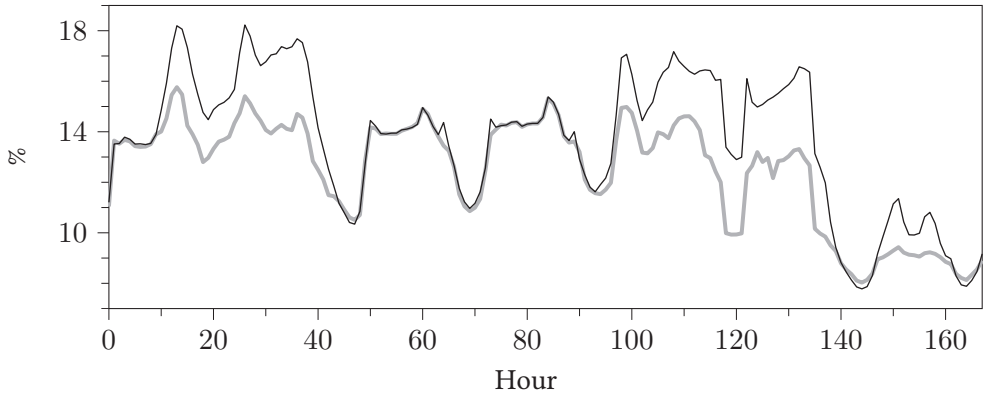

(b) Average branch utilization of the NEP (gray) and hybrid grid (black).

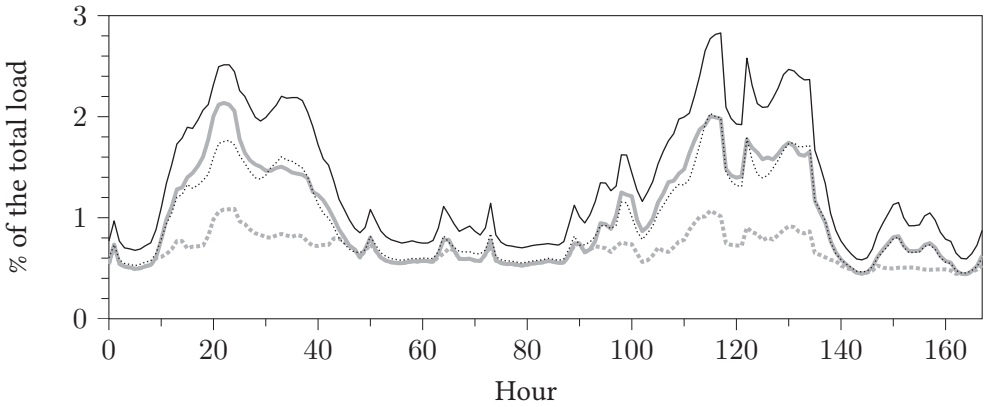

(c) Total losses (solid) and branch losses (dotted) of the NEP (gray) and hybrid grid (black).

Figure 7.13: Branch utilization and losses in the week with year's maximum load.

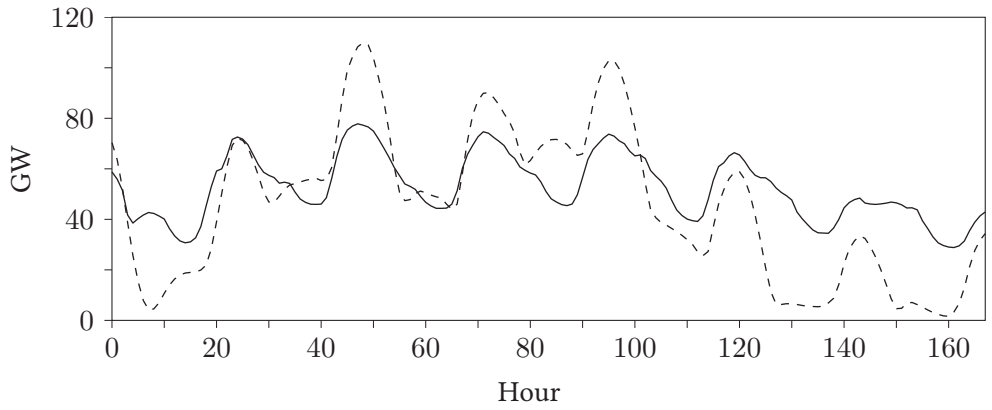

(a) Total load (solid) and RES capacity (dashed).

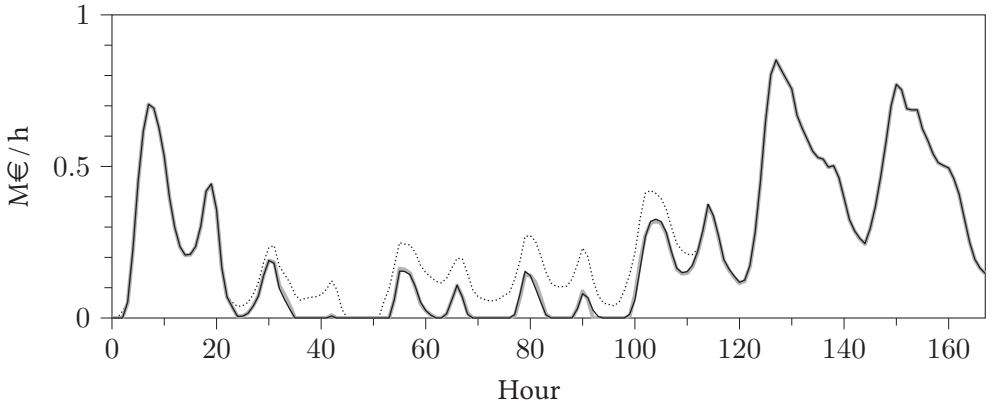

(b) Total injection cost of the NEP (gray), hybrid grid (black), and NEP w/o HVDC (dotted).

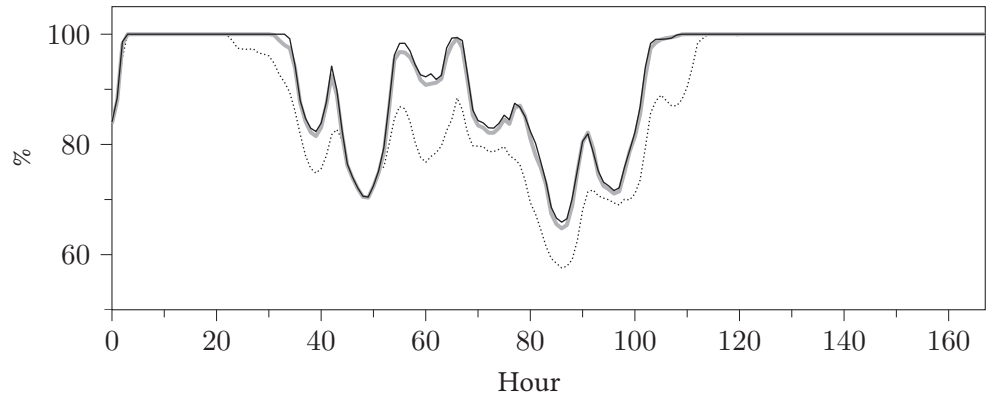

(c) RES utilization of the NEP (gray), hybrid grid (black), and NEP w/o HVDC (dotted).

Figure 7.14: Injection cost and RES utilization in the week with year's minimum load.

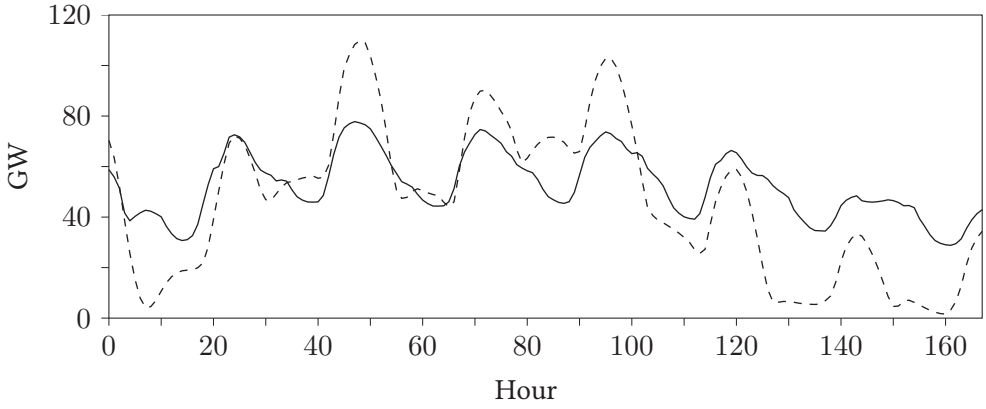

(a) Total load (solid) and RES capacity (dashed).

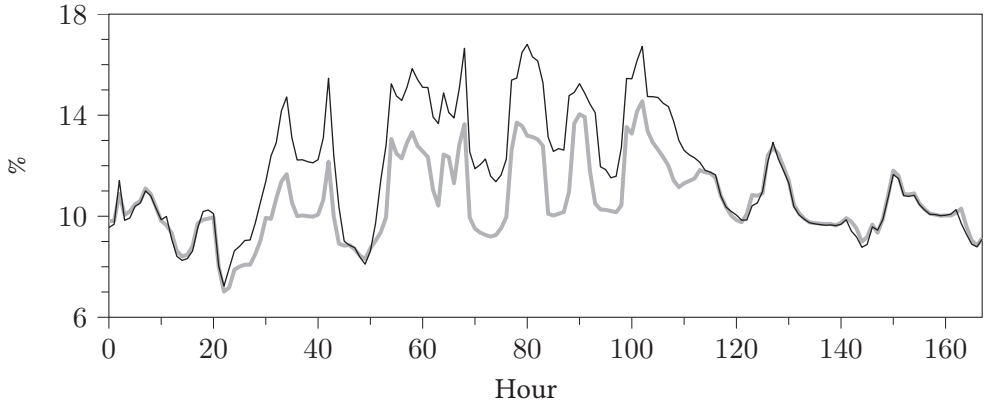

(b) Average branch utilization of the NEP (gray) and hybrid grid (black).

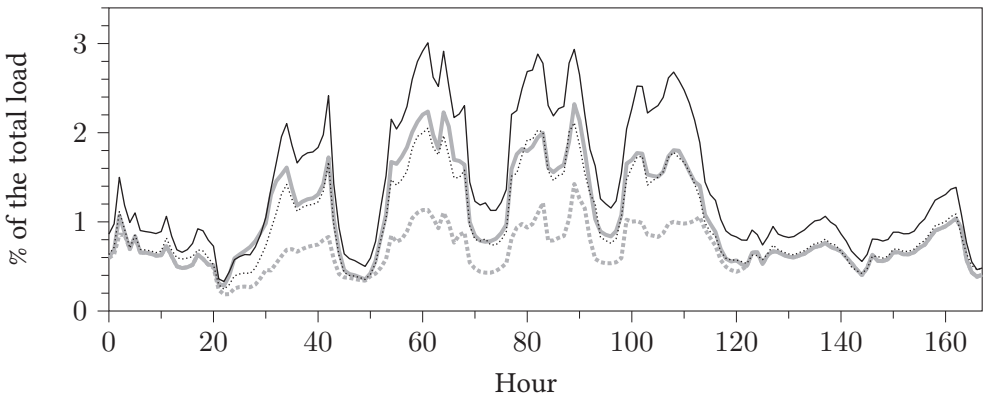

(c) Total losses (solid) and branch losses (dotted) of the NEP (gray) and hybrid grid (black).

Figure 7.15: Branch utilization and losses in the week with year's minimum load.

8 Conclusion

This work presented a mathematical and software framework for the study of the *optimal power flow* (OPF) in *hybrid AC/DC power systems*. Based on a rigorous modeling of the system, the OPF problem was introduced, its challenges were discussed, and a unified formulation was developed to simplify its implementation and mathematical study. On this basis, two convex relaxations were presented as an approach to improve the computational tractability of the OPF problem. Moreover, the *locational marginal prices* (LMPs) were related to the OPF problem and it was shown that the convex relaxations can also enable the efficient computation of optimal nodal prices for electricity markets. In order to render these results easily accessible for research and education, a corresponding software framework was developed that is offered open-source and free of charge. Therewith, a foundation for the exploration and study of hybrid AC/DC power systems was established, with applications ranging from operational and grid expansion planning to techno-economic studies.

Furthermore, the presented framework was utilized to deduce *design implications* for hybrid AC/DC power systems. In particular, it was shown that grid upgrade measures are readily available which increase the transmission capacity and, simultaneously, support the exactness of convex relaxations. The resulting system structure, the so-called *hybrid architecture*, utilizes the conversion of certain existing AC lines to DC operation for a systematic *grid flexibilization* and, alongside, induces a novel *topology-preserving capacity expansion strategy*. In several case studies, ranging from an illustrative small-scale example to an application in the German transmission grid, the potential of this strategy to effectively increase the transmission capacity and improve the utilization of the grid infrastructure was demonstrated.

The results show that the transition of an existing AC power system into a *structured* hybrid AC/DC power system can introduce significant and wide-ranging advantages. Furthermore, it demonstrates that the utilization of (VSC) HVDC technology beyond its traditional applications, i.e., long-distance, underground, and submarine transmission as well as the connection of asynchronous grids, can be

immensely valuable for *grid flexibilization*. In contrast to the traditional applications, the utilization of HVDC technology is then not motivated by a specific transmission task but by its impact on a *system level* to circumvent or mitigate power flow limitations due to grid congestion. Returning to the introductory historical account, this conclusion may bring some late peace to the *war of the currents*: It's the *synergy* of AC and DC technology induces a whole that is greater than the sum of its parts.

8.1 Directions for Future Research

An immediate direction for future research arising from this work is a further exploration of the key feature of the *hybrid architecture*, i.e., the resolution of cycles in the AC grid topology by the conversion of AC branches to DC operation. Such an exploration may consider different aspects, e.g., the application for grid flexibilization to resolve specific issues in existing systems, the study of further focusing techniques for the *hybrid architecture*, or the methodological exploitation of the gradually increasing tightness of the relaxations with the number of conversions.

The case studies show that the presented grid flexibilization strategy can increase the effective transmission capacity of the system even though the individual branch capacities remain unchanged. Consequently, the system can be operated closer to its branch capacity limits and, hence, a *resilient* (e.g., N-1 secure) operational planning gains even more importance. However, due to the increased flexibility in the power flow, the traditional *preventive* security-constrained operational planning is potentially overly and uneconomically conservative. Instead, the grid flexibilization may be utilized in *corrective* resilient operational planning, e.g., via the exploration of *security-constrained OPF problems* that consider HVDC systems for *corrective actions*.

Throughout this work, the hybrid AC/DC power systems were considered in steady state. However, especially in the light of a thorough flexibilization of the grid with HVDC systems, the proper *dynamic control* of the latter is crucial – and raises several questions. For example, how does it affect and shape the system stability? Do they necessitate a coordinated control? Can they be utilized for ancillary services, e.g., dynamic voltage support and oscillation damping? Et cetera …

Certainly, many questions and issues arising in the design and operation of hybrid AC/DC power systems are challenging. Yet, they are accompanied by opportunities: The more (VSC) HVDC systems are integrated, the more the system behavior is defined by control methods. These opportunities *we* can shape and design.

Bibliography

[1] M. Hotz and W. Utschick, "A hybrid transmission grid architecture enabling efficient optimal power flow," *IEEE Trans. Power Syst.*, vol. 31, no. 6, pp. 4504–4516, Nov. 2016.

[2] ——, "The hybrid transmission grid architecture: Benefits in nodal pricing," *IEEE Trans. Power Syst.*, vol. 33, no. 2, pp. 1431–1442, Mar. 2018.

[3] ——, "*hynet:* An optimal power flow framework for hybrid AC/DC power systems," *IEEE Trans. Power Syst.*, vol. 35, no. 2, pp. 1036–1047, Mar. 2020.

[4] L. P. M. I. Sampath, M. Hotz, H. B. Gooi, and W. Utschick, "Network-constrained thermal unit commitment for hybrid AC/DC transmission grids under wind power uncertainty," *Applied Energy*, vol. 258, Jan. 2020.

[5] M. Hotz, I. Boiarchuk, D. Hewes, R. Witzmann, and W. Utschick, "Reducing the need for new lines in Germany's energy transition: The hybrid transmission grid architecture," in *Proc. Int. ETG Congress 2017*, Nov. 2017.

[6] L. P. M. I. Sampath, M. Hotz, H. B. Gooi, and W. Utschick, "Unit commitment with AC power flow constraints for a hybrid transmission grid," in *Proc. 20th Power Syst. Comp. Conf. (PSCC)*, Jun. 2018.

[7] J. Sistermanns, M. Hotz, W. Utschick, D. Hewes, and R. Witzmann, "Feature- and structure-preserving network reduction for large-scale transmission grids," in *Proc. 13th IEEE PowerTech*, Milan, Italy, Jun. 2019.

[8] M. Hotz *et al.*, "*hynet:* An optimal power flow framework for hybrid AC/DC power systems (v1.0.0)," Nov. 2018. [Online]. Available: http://gitlab.com/tum-msv/hynet

[9] M. Hotz (Curator), "*hynet* Grid Database Library (v1.5)," Apr. 2020. [Online]. Available: http://gitlab.com/tum-msv/hynet-databases

[10] D. Jovcic and K. Ahmed, *High Voltage Direct Current Transmission: Converters, Systems and DC Grids*. Chichester, West Sussex, United Kingdom: John Wiley & Sons, Ltd, 2015.

[11] Uno Lamm HVDC Center, "HVDC Light – It's time to connect," ABB AB, Ludvika, Sweden, Tech. Rep. POW0038 (Rev. H), Aug. 2017.

[12] M. P. Bahrman and B. K. Johnson, "The ABCs of HVDC transmission technologies," *IEEE Power and Energy Mag.*, vol. 5, no. 2, pp. 32–44, Mar. 2007.

[13] G. Arcia-Garibaldi, P. Cruz-Romero, and A. Gómez-Expósito, "Future power transmission: Visions, technologies and challenges," *Renewable and Sustainable Energy Reviews*, vol. 94, pp. 285–301, 2018.

[14] G. Buigues, V. Valverde, A. Etxegarai, P. Eguía, and E. Torres, "Present and future multiterminal HVDC systems: Current status and forthcoming developments," in *Proc. Int. Conf. Renewable Energies and Power Quality*, Malaga, Spain, Apr. 2017, pp. 83–88.

[15] OECD/IEA, *Large-Scale Electricity Interconnection: Technology and prospects for cross-regional networks*. Int. Energy Agency, 2016.

[16] J. Carpentier, "Contribution á l'ètude du dispatching èconomique," *Bulletin de la Société Française des Électriciens*, vol. 8, no. 3, pp. 431–447, Aug. 1962.

[17] J. L. Carpentier, "Optimal power flows: Uses, methods and developments," *IFAC Proceedings Volumes*, vol. 18, no. 7, pp. 11–21, 1985.

[18] S. Frank, I. Steponavice, and S. Rebennack, "Optimal power flow: A bibliographic survey I," *Energy Syst.*, vol. 3, no. 3, pp. 221–258, 2012.

[19] ——, "Optimal power flow: A bibliographic survey II," *Energy Syst.*, vol. 3, no. 3, pp. 259–289, 2012.

[20] M. B. Cain, R. P. O'Neill, and A. Castillo, "History of optimal power flow and formulations," *Staff Paper for the Federal Energy Regulatory Commission*, Dec. 2012.

[21] S. H. Low, "Convex relaxation of optimal power flow – Part I: Formulations and equivalence," *IEEE Trans. Control of Netw. Syst.*, vol. 1, no. 1, pp. 15–27, Mar. 2014.

[22] A. J. Wood and B. F. Wollenberg, *Power Generation, Operation, and Control*, 2nd ed. Wiley, 1996.

[23] J. Zhu, *Optimization of Power System Operation*, 2nd ed., ser. IEEE Press Series on Power Engineering. Hoboken, NJ, USA: John Wiley & Sons, Ltd, 2015.

[24] S. Frank and S. Rebennack, "An introduction to optimal power flow: Theory, formulation, and examples," *IIE Transactions*, vol. 48, no. 12, pp. 1172–1197, 2016.

[25] F. Capitanescu, J. L. M. Ramos, P. Panciatici, D. Kirschen, A. M. Marcolini, L. Platbrood, and L. Wehenkel, "State-of-the-art, challenges, and future trends in security constrained optimal power flow," *Electric Power Syst. Research*, vol. 81, no. 8, pp. 1731–1741, 2011.

[26] T. Faulwasser, A. Engelmann, T. Mühlpfordt, and V. Hagenmeyer, "Optimal power flow: An introduction to predictive, distributed and stochastic control challenges," *Automatisierungstechnik*, vol. 66, no. 7, pp. 573–589, Jul. 2018.

[27] C. N. Lu, S. S. Chen, and C. M. Ing, "The incorporation of HVDC equations in optimal power flow methods using sequential quadratic programming techniques," *IEEE Trans. Power Syst.*, vol. 3, no. 3, pp. 1005–1011, Aug. 1988.

[28] R. Wiget and G. Andersson, "Optimal power flow for combined AC and multi-terminal HVDC grids based on VSC converters," in *Proc. IEEE PES General Meeting*, Jul. 2012.

[29] J. Cao, W. Du, H. F. Wang, and S. Q. Bu, "Minimization of transmission loss in meshed AC/DC grids with VSC-MTDC networks," *IEEE Trans. Power Syst.*, vol. 28, no. 3, pp. 3047–3055, Aug. 2013.

[30] W. Feng, A. L. Tuan, L. B. Tjernberg, A. Mannikoff, and A. Bergman, "A new approach for benefit evaluation of multiterminal VSC-HVDC using a proposed mixed AC/DC optimal power flow," *IEEE Trans. Power Delivery*, vol. 29, no. 1, pp. 432–443, Feb. 2014.

[31] Q. Zhao, J. García-González, O. Gomis-Bellmunt, E. Prieto-Araujo, and F. M. Echavarren, "Impact of converter losses on the optimal power flow solution of hybrid networks based on VSC-MTDC," *Electric Power Syst. Research*, vol. 151, pp. 395–403, 2017.

[32] M. Baradar, M. R. Hesamzadeh, and M. Ghandhari, "Second-order cone programming for optimal power flow in VSC-type AC-DC grids," *IEEE Trans. Power Syst.*, vol. 28, no. 4, pp. 4282–4291, Nov. 2013.

[33] S. Bahrami, F. Therrien, V. W. S. Wong, and J. Jatskevich, "Semidefinite relaxation of optimal power flow for AC–DC grids," *IEEE Trans. Power Syst.*, vol. 32, no. 1, pp. 289–304, Jan. 2017.

[34] A. Venzke and S. Chatzivasileiadis, "Convex relaxations of probabilistic AC optimal power flow for interconnected AC and HVDC grids," *IEEE Trans. Power Syst.*, vol. 34, no. 4, pp. 2706–2718, Jul. 2019.

[35] H. Ergun, J. Dave, D. Van Hertem, and F. Geth, "Optimal power flow for AC–DC grids: Formulation, convex relaxation, linear approximation, and implementation," *IEEE Trans. Power Syst.*, vol. 34, no. 4, pp. 2980–2990, Jul. 2019.

[36] N. Meyer-Huebner, M. Suriyah, and T. Leibfried, "Distributed optimal power flow in hybrid AC–DC grids," *IEEE Trans. Power Syst.*, vol. 34, no. 4, pp. 2937–2946, Jul. 2019.

[37] J. Beerten, S. Cole, and R. Belmans, "Generalized steady-state VSC MTDC model for sequential AC/DC power flow algorithms," *IEEE Trans. Power Syst.*, vol. 27, no. 2, pp. 821–829, May 2012.

[38] CIGRE Working Group B4.57, "Guide for the development of models for HVDC converters in a HVDC grid," *CIGRE Brochure 604*, Dec. 2014.

[39] D. Kirschen and G. Strbac, *Fundamentals of Power System Economics.* John Wiley & Sons, Ltd, 2004.

[40] A. Gómez-Expósito, A. J. . Conejo, and C. Cañizares, Eds., *Electric Energy Systems: Analysis and Operation.* Boca Raton, FL, USA: CRC Press, 2008.

[41] B. Stott, J. Jardim, and O. Alsac, "DC power flow revisited," *IEEE Trans. Power Syst.*, vol. 24, no. 3, pp. 1290–1300, Aug. 2009.

[42] S. Boyd and L. Vandenberghe, *Convex Optimization.* Cambridge, UK: Cambridge University Press, 2004.

[43] M. S. Bazaraa, H. D. Sherali, and C. M. Shetty, *Nonlinear Programming: Theory and Algorithms*, 3rd ed. Hoboken, NJ, USA: John Wiley & Sons, Inc., 2006.

[44] R. T. Rockafellar, *Convex Analysis*, ser. Princeton Landmarks in Mathematics. Princeton, NJ, USA: Princeton University Press, 1997.

[45] J.-B. Hiriart-Urruty and C. Lemaréchal, *Convex Analysis and Minimization Algorithms I.* Berlin/Heidelberg, Germany: Springer-Verlag, 1996.

[46] ——, *Convex Analysis and Minimization Algorithms II.* Berlin/Heidelberg, Germany: Springer-Verlag, 1996.

[47] Y. Nesterov, *Lectures on Convex Optimization*, 2nd ed., ser. Springer Optimization and Its Applications. Cham, Switzerland: Springer, 2018, vol. 137.

[48] D. P. Bertsekas, A. Nedić, and A. E. Ozdaglar, *Convex Analysis and Optimization*, ser. Optimization and Computation Series. Belmont, MA, USA: Athena Scientific, 2003.

[49] R. A. Jabr, "Radial distribution load flow using conic programming," *IEEE Trans. Power Syst.*, vol. 21, no. 3, pp. 1458–1459, Aug. 2006.

[50] X. Bai, H. Wei, K. Fujisawa, and Y. Wang, "Semidefinite programming for optimal power flow problems," *Int. J. Electrical Power & Energy Syst.*, vol. 30, no. 6-7, pp. 383–392, 2008.

[51] J. Lavaei and S. H. Low, "Zero duality gap in optimal power flow problem," *IEEE Trans. Power Syst.*, vol. 27, no. 1, pp. 92–107, Feb. 2012.

[52] M. Farivar and S. H. Low, "Branch flow model: Relaxations and convexification – Part I," *IEEE Trans. Power Syst.*, vol. 28, no. 3, pp. 2554–2564, Aug. 2013.

[53] J. A. Taylor, *Convex Optimization of Power Systems.* Cambridge, UK: Cambridge University Press, 2015.

[54] D. K. Molzahn and I. A. Hiskens, "Sparsity-exploiting moment-based relaxations of the optimal power flow problem," *IEEE Trans. Power Syst.*, vol. 30, no. 6, pp. 3168–3180, Nov. 2015.

[55] B. Ghaddar, J. Marecek, and M. Mevissen, "Optimal power flow as a polynomial optimization problem," *IEEE Trans. Power Syst.*, vol. 31, no. 1, pp. 539–546, Jan. 2016.

[56] C. Coffrin, H. L. Hijazi, and P. V. Hentenryck, "The QC relaxation: A theoretical and computational study on optimal power flow," *IEEE Trans. Power Syst.*, vol. 31, no. 4, pp. 3008–3018, Jul. 2016.

[57] B. Kocuk, S. S. Dey, and X. A. Sun, "Strong SOCP relaxations for the optimal power flow problem," *Operations Research*, vol. 64, no. 6, pp. 1177–1196, Nov. 2016.

[58] C. Bingane, M. F. Anjos, and S. Le Digabel, "Tight-and-cheap conic relaxation for the AC optimal power flow problem," *IEEE Trans. Power Syst.*, vol. 33, no. 6, pp. 7181–7188, Nov. 2018.

[59] S. Bahrami and V. W. S. Wong, "Security-constrained unit commitment for AC-DC grids with generation and load uncertainty," *IEEE Trans. Power Syst.*, vol. 33, no. 3, pp. 2717–2732, May 2018.

[60] B. Zhang and D. Tse, "Geometry of injection regions of power networks," *IEEE Trans. Power Syst.*, vol. 28, no. 2, pp. 788–797, May 2013.

[61] S. H. Low, "Convex relaxation of optimal power flow – Part II: Exactness," *IEEE Trans. Control of Netw. Syst.*, vol. 1, no. 2, pp. 177–189, Jun. 2014.

[62] L. Gan, N. Li, U. Topcu, and S. H. Low, "Exact convex relaxation of optimal power flow in radial networks," *IEEE Trans. Automatic Control*, vol. 60, no. 1, pp. 72–87, Jan. 2015.

[63] R. Madani, S. Sojoudi, and J. Lavaei, "Convex relaxation for optimal power flow problem: Mesh networks," *IEEE Trans. Power Syst.*, vol. 30, no. 1, pp. 199–211, Jan. 2015.

[64] M. Nick, R. Cherkaoui, J. L. Boudec, and M. Paolone, "An exact convex formulation of the optimal power flow in radial distribution networks including transverse components," *IEEE Trans. Automatic Control*, vol. 63, no. 3, pp. 682–697, Mar. 2018.

[65] L. Gan and S. H. Low, "Optimal power flow in direct current networks," *IEEE Trans. Power Syst.*, vol. 29, no. 6, pp. 2892–2904, Nov. 2014.

[66] C. W. Tan, D. W. H. Cai, and X. Lou, "Resistive network optimal power flow: Uniqueness and algorithms," *IEEE Trans. Power Syst.*, vol. 30, no. 1, pp. 263–273, Jan. 2015.

[67] European Commission, *The Strategic Energy Technology Plan.* Publications Office of the European Union, 2017.

[68] R. Baldick and R. P. O'Neill, "Estimates of comparative costs for uprating transmission capacity," *IEEE Trans. Power Delivery*, vol. 24, no. 2, pp. 961–969, Apr. 2009.

[69] CIGRE Working Group B2/C1.19, "Increasing capacity of overhead transmission lines – Needs and solutions," *CIGRE Brochure 425*, Aug. 2010.

[70] Bundesnetzagentur für Elektrizität, Gas, Telekommunikation, Post und Eisenbahnen, "Bedarfsermittlung 2024 - Zusammenfassung der Konsultationsergebnisse," Tech. Rep., Sep. 2015.

[71] ——, "Bedarfsermittlung 2017 - 2030: Zusammenfassung der Konsultationsergebnisse," Tech. Rep., Dec. 2017.

[72] Python Core Team, "Python: A dynamic, open source programming language (v3.7.1)," Oct. 2018. [Online]. Available: http://www.python.org

[73] M. Farivar and S. H. Low, "Branch flow model: Relaxations and convexification – Part II," *IEEE Trans. Power Syst.*, vol. 28, no. 3, pp. 2565–2572, Aug. 2013.

[74] S. Bose, D. F. Gayme, K. M. Chandy, and S. H. Low, "Solving quadratically constrained quadratic programs on acyclic graphs with application to optimal power flow," in *Proc. 48th Annual Conf. Information Sciences and Syst.*, Mar. 2014, pp. 1–5.

[75] A. R. Bergen and V. Vittal, *Power Systems Analysis*, 2nd ed. Upper Saddle River, NJ, USA: Prentice Hall, 2000.

[76] P. Kundur, *Power System Stability and Control*, ser. EPRI Power System Engineering Series. McGraw-Hill, 1994.

[77] D. Van Hertem, O. Gomis-Bellmunt, and J. Liang, *HVDC Grids – For Offshore and Supergrid of the Future*, ser. IEEE Press Series on Power Engineering. Wiley, 2016.

[78] M. Baradar and M. Ghandhari, "A multi-option unified power flow approach for hybrid AC/DC grids incorporating multi-terminal VSC-HVDC," *IEEE Trans. Power Syst.*, vol. 28, no. 3, pp. 2376–2383, Aug. 2013.

[79] G. Daelemans, "VSC HVDC in meshed networks," Master's thesis, Katholieke Universiteit Leuven, Leuven, Belgium, 2008.

[80] J. Beerten, S. Cole, and R. Belmans, "A sequential AC/DC power flow algorithm for networks containing multi-terminal VSC HVDC systems," in *IEEE PES General Meeting*, Jul. 2010, pp. 1–7.

[81] G. Daelemans, K. Srivastava, M. Reza, S. Cole, and R. Belmans, "Minimization of steady-state losses in meshed networks using VSC HVDC," in *IEEE PES General Meeting*, Jul. 2009, pp. 1–5.

[82] J. A. Bondy and U. S. R. Murty, *Graph Theory with Applications*. North Holland, 1976.

[83] M. Davies, M. Dommaschk, J. Dorn, J. Lang, D. Retzmann, and D. Soerangr, "HVDC PLUS – Basics and principle of operation," Siemens AG, Erlangen, Germany, Tech. Rep., 2009.

[84] R. D. Zimmerman, C. E. Murillo-Sánchez, and R. J. Thomas, "MATPOWER: Steady-state operations, planning, and analysis tools for power systems research and education," *IEEE Trans. Power Syst.*, vol. 26, no. 1, pp. 12–19, Feb. 2011.

[85] M. R. Garey and D. S. Johnson, *Computers and Intractability: A Guide to the Theory of NP-Completeness*, ser. Series of Books in the Mathematical Sciences. New York, NY, USA: W. H. Freeman & Co., 1979.

[86] P. L. Hammer and A. A. Rubin, "Some remarks on quadratic programming with 0-1 variables," *RAIRO - Oper. Res.*, vol. 4, no. V-3, pp. 67–79, 1970.

[87] A. Forsgren, P. E. Gill, and M. H. Wright, "Interior methods for nonlinear optimization," *SIAM Review*, vol. 44, no. 4, pp. 525–597, 2002.

[88] W. A. Bukhsh, A. Grothey, K. I. M. McKinnon, and P. A. Trodden, "Local solutions of the optimal power flow problem," *IEEE Trans. Power Syst.*, vol. 28, no. 4, pp. 4780–4788, Nov. 2013.

[89] C. Coffrin, R. Bent, K. Sundar, Y. Ng, and M. Lubin, "PowerModels.jl: An open-source framework for exploring power flow formulations," in *Proc. 20th Power Syst. Comp. Conf. (PSCC)*, Jun. 2018.

[90] S. Boyd, N. Parikh, E. Chu, B. Peleato, and J. Eckstein, "Distributed optimization and statistical learning via the alternating direction method of multipliers," *Foundations and Trends in Machine Learning*, vol. 3, no. 1, pp. 1–122, 2011.

[91] D. P. Bertsekas and J. N. Tsitsiklis, *Parallel and Distributed Computation: Numerical Methods*, ser. Optimization and Neural Computation Series. Belmont, MA, USA: Athena Scientific, 1997.

[92] R. A. Horn and C. R. Johnson, *Matrix Analysis*, 2nd ed. New York, NY, USA: Cambridge University Press, 2013.

[93] Z.-Q. Luo, W.-K. Ma, A. M.-C. So, Y. Ye, and S. Zhang, "Semidefinite relaxation of quadratic optimization problems," *IEEE Signal Processing Mag.*, vol. 27, no. 3, pp. 20–34, May 2010.

[94] D. K. Molzahn, B. C. Lesieutre, and C. L. DeMarco, "Investigation of non-zero duality gap solutions to a semidefinite relaxation of the optimal power flow problem," in *Proc. 47th Hawaii Int. Conf. Syst. Sciences*, Jan. 2014, pp. 2325–2334.

[95] D. K. Molzahn, J. T. Holzer, B. C. Lesieutre, and C. L. DeMarco, "Implementation of a large-scale optimal power flow solver based on semidefinite programming," *IEEE Trans. Power Syst.*, vol. 28, no. 4, pp. 3987–3998, Nov. 2013.

[96] B. Kocuk, S. S. Dey, and X. A. Sun, "Inexactness of SDP relaxation and valid inequalities for optimal power flow," *IEEE Trans. Power Syst.*, vol. 31, no. 1, pp. 642–651, Jan. 2016.

[97] M. Fukuda, M. Kojima, K. Murota, and K. Nakata, "Exploiting sparsity in semidefinite programming via matrix completion I: General framework," *SIAM J. Optimization*, vol. 11, no. 3, pp. 647–674, 2001.

[98] E. de Klerk, "Exploiting special structure in semidefinite programming: A survey of theory and applications," *European J. Operational Research*, vol. 201, no. 1, pp. 1–10, 2010.

[99] R. A. Jabr, "Exploiting sparsity in SDP relaxations of the OPF problem," *IEEE Trans. Power Syst.*, vol. 27, no. 2, pp. 1138–1139, May 2012.

[100] M. S. Andersen, A. Hansson, and L. Vandenberghe, "Reduced-complexity semidefinite relaxations of optimal power flow problems," *IEEE Trans. Power Syst.*, vol. 29, no. 4, pp. 1855–1863, Jul. 2014.

[101] A. Eltved, J. Dahl, and M. S. Andersen, "On the robustness and scalability of semidefinite relaxation for optimal power flow problems," *Optimization and Engineering*, vol. 20, Mar. 2019.

[102] S. Kim and M. Kojima, "Exact solutions of some nonconvex quadratic optimization problems via SDP and SOCP relaxations," *Computational Optimization and Applications*, vol. 26, no. 2, pp. 143–154, Nov. 2003.

[103] ——, "Second order cone programming relaxation of nonconvex quadratic optimization problems," *Optimization Methods and Software*, vol. 15, no. 3-4, pp. 201–224, 2001.

[104] S. Kim, M. Kojima, and M. Yamashita, "Second order cone programming relaxation of a positive semidefinite constraint," *Optimization Methods and Software*, vol. 18, no. 5, pp. 535–541, 2003.

[105] F. Alizadeh and D. Goldfarb, "Second-order cone programming," *Mathematical Programming*, vol. 95, no. 1, pp. 3–51, Jan. 2003.

[106] S. Stoft, *Power System Economics: Designing Markets for Electricity*. IEEE Press & Wiley-Interscience, 2002.

[107] D. Gan, D. Feng, and J. Xie, *Electricity Markets and Power System Economics*. Boca Raton, FL, USA: CRC Press, 2013.

[108] A. Jokić, "Price-based optimal control of electrical power systems," Ph.D. dissertation, Technische Universiteit Eindhoven, 2007.

[109] T. J. Overbye, X. Cheng, and Y. Sun, "A comparison of the AC and DC power flow models for LMP calculations," in *Proc. 37th Hawaii Int. Conf. Syst. Sciences*, Jan. 2004, pp. 1–9.

[110] H. Wang, C. E. Murillo-Sanchez, R. D. Zimmerman, and R. J. Thomas, "On computational issues of market-based optimal power flow," *IEEE Trans. Power Syst.*, vol. 22, no. 3, pp. 1185–1193, Aug. 2007.

[111] F. Li and R. Bo, "DCOPF-based LMP simulation: Algorithm, comparison with ACOPF, and sensitivity," *IEEE Trans. Power Syst.*, vol. 22, no. 4, pp. 1475–1485, Nov. 2007.

[112] A. Ben-Tal and A. Nemirovski, *Lectures on Modern Convex Optimization*, ser. MPS/SIAM Series on Optimization. Society for Industrial and Applied Mathematics, 2001.

[113] MOSEK ApS, *The MOSEK Optimizer API for Python manual. Version 9.0.*, 2019. [Online]. Available: http://docs.mosek.com/9.0/pythonapi.pdf

[114] A. Venzke, S. Chatzivasileiadis, and D. K. Molzahn, "Inexact convex relaxations for AC optimal power flow: Towards AC feasibility," *arXiv:1902.04815*, Oct. 2019.

[115] R. Madani, M. Ashraphijuo, and J. Lavaei, "Promises of conic relaxation for contingency-constrained optimal power flow problem," *IEEE Trans. Power Syst.*, vol. 31, no. 2, pp. 1297–1307, Mar. 2016.

[116] Z. Yuan and M. R. Hesamzadeh, "Second-order cone AC optimal power flow: Convex relaxations and feasible solutions," *J. Modern Power Syst. and Clean Energy*, vol. 7, no. 2, pp. 268–280, 2019.

[117] D. Shchetinin, T. T. De Rubira, and G. Hug, "Efficient bound tightening techniques for convex relaxations of AC optimal power flow," *IEEE Trans. Power Syst.*, vol. 34, no. 5, pp. 3848–3857, Sep. 2019.

[118] T. P. Hughes, *Networks of Power: Electrification in Western Society, 1880-1930*. Johns Hopkins University Press, 1993.

[119] 50Hertz Transmission, Amprion, TenneT TSO, and TransnetBW, "Netzentwicklungsplan Strom 2030 (2. Entwurf)," Tech. Rep., Apr. 2019.

[120] ——, "Netzentwicklungsplan Strom 2030 (2. Entwurf) – Hintergrundmaterial: Kostenschätzungen," Tech. Rep., 2019.

[121] CIGRE Working Group B2.41, "Guide to the conversion of existing AC lines to DC operation," *CIGRE Brochure 583*, May 2014.

[122] ABB Grid Systems, "Boosting power with HVDC Light – Fast-track solution increases capacity of existing infrastructure to help meet EU emissions targets," ABB AB, Ludvika, Sweden, Tech. Rep. POW0077, May 2012.

[123] CIGRE Working Group B4.46, "Voltage source converter (VSC) HVDC for power transmission – Economic aspects and comparison with other AC and DC technologies," *CIGRE Brochure 492*, Apr. 2012.

[124] S. Bose, D. F. Gayme, S. H. Low, and K. M. Chandy, "Optimal power flow over tree networks," in *Proc. 49th Annu. Allerton Conf. Communication, Control, and Comp.*, Sep. 2011.

[125] S. Bose, D. F. Gayme, K. M. Chandy, and S. H. Low, "Quadratically constrained quadratic programs on acyclic graphs with application to power flow," *IEEE Trans. Control of Netw. Syst.*, vol. 2, no. 3, pp. 278–287, Sep. 2015.

[126] H. van der Holst, "Graphs whose positive semi-definite matrices have nullity at most two," *Linear Algebra and its Applications*, vol. 375, pp. 1–11, 2003.

[127] C. R. Johnson, A. L. Duarte, C. M. Saiago, B. D. Sutton, and A. J. Witt, "On the relative position of multiple eigenvalues in the spectrum of an Hermitian matrix with a given graph," *Linear Algebra and its Applications*, vol. 363, pp. 147–159, 2003.

[128] Y. C. de Verdière, "Multiplicities of eigenvalues and tree-width of graphs," *J. Combinatorial Theory, Series B*, vol. 74, no. 2, pp. 121–146, 1998.

[129] S. Bose, S. H. Low, and K. M. Chandy, "Equivalence of branch flow and bus injection models," in *Proc. 50th Annu. Allerton Conf. Communication, Control, and Comp.*, Oct. 2012, pp. 1893–1899.

[130] J. B. Ward, "Equivalent circuits for power-flow studies," *AIEE Transactions*, vol. 68, pp. 373–382, Jul. 1949.

[131] F. F. Wu and A. Monticelli, "Critical review of external network modelling for online security analysis," *Int. J. Electrical Power & Energy Syst.*, vol. 5, no. 4, 1983.

[132] H. E. Brown, *Solution of Large Networks by Matrix Methods.* New York: John Wiley & Sons Inc, 1985.

[133] H. Duran and N. Arvanitidis, "Simplification for area security analysis: A new look at equivalencing," *IEEE Trans. Power App. Syst.*, vol. PAS-91, pp. 670–679, Mar. 1972.

[134] A. Monticelli, S. Deckmann, A. Garcia, and B. Stott, "Real-time external equivalents for static security analysis," *IEEE Trans. Power App. Syst.*, vol. PAS-98, no. 2, pp. 498–508, Mar. 1979.

[135] S. Deckmann, A. Pizzolante, A. Monticelli, B. Stott, and O. Alsac, "Studies on power system load flow equivalencing," *IEEE Trans. Power App. Syst.*, vol. PAS-99, no. 6, pp. 2301–2310, Nov. 1980.

[136] P. Dimo, *Nodal Analysis of Power Systems.* Kent, England: Abacus Press, 1975.

[137] M. Gavrilas, O. Ivanov, and G. Gavrilas, "REI equivalent design for electric power systems with genetic algorithms," *WSEAS Trans. Circuits and Syst.*, vol. 7, no. 10, pp. 911–921, Oct. 2008.

[138] F. Milano and K. Srivastava, "Dynamic REI equivalents for short circuit and transient stability analyses," *Electric Power Syst. Research*, vol. 79, no. 6, pp. 878–887, Jan. 2009.

[139] W. F. Tinney and W. L. Powell, "The REI approach to power network equivalents," in *Proc. IEEE PICA Conf.*, Toronto, Canada, May 1977, pp. 314–320.

[140] E. C. Housos, G. Irisarri, R. M. Porter, and A. M. Sasson, "Steady state network equivalents for power system planning applications," *IEEE Trans. Power Apparatus and Syst.*, vol. PAS-99, no. 6, pp. 2113–2120, Nov. 1980.

[141] A. Papaemmanouil and G. Andersson, "On the reduction of large power system models for power market simulations," in *Proc. 17th Power Syst. Comp. Conf. (PSCC)*, Aug. 2011.

[142] R. D. Zimmerman, C. E. Murillo-Sánchez *et al.*, "MATPOWER: A Matlab power system simulation package (v6.0b2)," Nov. 2016. [Online]. Available: http://www.pserc.cornell.edu/matpower/

[143] R. Lincoln, "PYPOWER: A port of MATPOWER to Python (v5.1.2)," Jun. 2017. [Online]. Available: http://github.com/rwl/PYPOWER

[144] F. Milano, "An open source power system analysis toolbox," *IEEE Trans. Power Syst.*, vol. 20, no. 3, pp. 1199–1206, Aug. 2005.

[145] ——, "PSAT: Matlab-based power system analysis toolbox (v2.1.10)," Jun. 2016. [Online]. Available: http://faraday1.ucd.ie/psat.html

[146] C. Coffrin *et al.*, "PowerModels.jl: A Julia/JuMP package for power network optimization (v0.8.5)," Oct. 2018. [Online]. Available: http://github.com/lanl-ansi/PowerModels.jl

[147] L. Thurner, A. Scheidler, F. Schäfer, J. Menke, J. Dollichon, F. Meier, S. Meinecke, and M. Braun, "Pandapower—An open-source Python tool for convenient modeling, analysis, and optimization of electric power systems," *IEEE Trans. Power Syst.*, vol. 33, no. 6, pp. 6510–6521, Nov. 2018.

[148] ——, "pandapower: An easy to use open source tool for power system modeling, analysis and optimization with a high degree of automation (v1.6.0)," Sep. 2018. [Online]. Available: http://www.pandapower.org/

[149] J. Beerten and R. Belmans, "Development of an open source power flow software for high voltage direct current grids and hybrid AC/DC systems: MATACDC," *IET Generation, Transmission & Distribution*, vol. 9, no. 10, pp. 966–974, 2015.

[150] W. McKinney, "Data structures for statistical computing in Python," in *Proc. 9th Python in Science Conf.*, 2010, pp. 51–56.

[151] E. Gamma, R. Helm, R. Johnson, and J. Vlissides, *Design Patterns: Elements of Reusable Object-Oriented Software*, ser. Professional Computing Series. Addison-Wesley, 1994.

[152] H. Li and T. Adalı, "Complex-valued adaptive signal processing using nonlinear functions," *EURASIP J. Advances in Signal Process.*, vol. 2008, Feb. 2008.

[153] G. D. Irisarri, X. Wang, J. Tong, and S. Mokhtari, "Maximum loadability of power systems using interior point nonlinear optimization method," *IEEE Trans. Power Syst.*, vol. 12, no. 1, pp. 162–172, Feb. 1997.

[154] A. Wächter and L. T. Biegler, "On the implementation of an interior-point filter line-search algorithm for large-scale nonlinear programming," *Mathematical Programming*, vol. 106, no. 1, pp. 25–57, Mar. 2006.

[155] P. R. Amestoy, I. S. Duff, J. Koster, and J.-Y. L'Excellent, "A fully asynchronous multifrontal solver using distributed dynamic scheduling," *SIAM J. Matrix Analysis and Applications*, vol. 23, no. 1, pp. 15–41, 2001.

[156] P. R. Amestoy, A. Guermouche, J.-Y. L'Excellent, and S. Pralet, "Hybrid scheduling for the parallel solution of linear systems," *Parallel Computing*, vol. 32, no. 2, pp. 136–156, 2006.

[157] IBM, *IBM ILOG CPLEX Optimization Studio (v12.9)*, 2019. [Online]. Available: http://www.ibm.com/products/ilog-cplex-optimization-studio

[158] F. Li and R. Bo, "Small test systems for power system economic studies," in *Proc. IEEE PES General Meeting*, Jul. 2010.

[159] R. Merris, "Laplacian matrices of graphs: A survey," *Linear Algebra and its Applications*, vol. 197-198, pp. 143–176, 1994.

[160] D. E. Knuth, *The Art of Computer Programming – Combinatorial Algorithms*. Addison-Wesley, 2011, vol. 4A.

[161] M. Hotz, "`generateSpanningTrees(A)` – Generating all spanning trees for a connected undirected simple graph," Nov. 2015. [Online]. Available: https://de.mathworks.com/matlabcentral/fileexchange/53787-generatespanningtrees-a

[162] R. D. Zimmerman, C. E. Murillo-Sánchez *et al.*, "MATPOWER: A Matlab power system simulation package (version 7.0)," Jun. 2019. [Online]. Available: https://matpower.org

[163] T. Oliphant, "NumPy: A guide to NumPy," USA: Trelgol Publishing, 2006, Version 1.17.0, 2019. [Online]. Available: http://www.numpy.org/

[164] MATLAB, *version 9.0.0 (R2016a)*. Natick, Massachusetts: The MathWorks Inc., 2016. [Online]. Available: http://www.mathworks.com/

[165] R. C. Prim, "Shortest connection networks and some generalizations," *Bell Syst. Tech. J.*, vol. 36, no. 6, pp. 1389–1401, Nov. 1957.

[166] J. B. Kruskal, "On the shortest spanning subtree of a graph and the traveling salesman problem," *Proc. Amer. Math. Soc.*, vol. 7, pp. 48–50, Feb. 1956.

[167] R. Sedgewick and K. Wayne, *Algorithms*, 4th ed. Addison-Wesley, 2011.

[168] C. Grigg, P. Wong, P. Albrecht, R. Allan, M. Bhavaraju, R. Billinton, Q. Chen, C. Fong, S. Haddad, S. Kuruganty, W. Li, R. Mukerji, D. Patton, N. Rau, D. Reppen, A. Schneider, M. Shahidehpour, and C. Singh, "The IEEE reliability test system - 1996. A report prepared by the Reliability Test System Task Force of the Application of Probability Methods Subcommittee," *IEEE Trans. Power Syst.*, vol. 14, no. 3, pp. 1010–1020, Aug. 1999.

[169] 50Hertz Transmission, Amprion, TenneT TSO, and TransnetBW, "Netzentwicklungsplan Strom 2030 (1. Entwurf)," Tech. Rep., Jan. 2017.

[170] ——, "Netzentwicklungsplan Strom 2030 (1. Entwurf)," Tech. Rep., Feb. 2019.

[171] D. Hewes, S. Altschaeffl, I. Boiarchuk, and R. Witzmann, "Development of a dynamic model of the European transmission system using publicly available data," in *Proc. IEEE Int. Energy Conf. (ENERGYCON)*, Apr. 2016.